ON THE USE OF INTERFACIAL FRACTURE MECHANICS APPROACHES FOR EVALUATION OF THE END MOVEMENT IN CONCRETE SLABS

A Dissertation

by

MIRMILAD MIRSAYAR

Submitted to the Office of Graduate and Professional Studies of
Texas A&M University
in partial fulfillment of the requirements for the degree of

DOCTOR OF PHILOSOPHY

Chair of Committee,	Dan Zollinger
Committee Members,	Robert Lytton
	Zachary Grasley
	Alan Freed
Head of Department,	Robin Autenrieth

May 2017

Major Subject: Civil Engineering

ABSTRACT

This dissertation aims to study effects of different design factors on the end movements in Continuously Reinforced Concrete (CRC) pavements subjected to environmental loads. End movement in CRC pavements is an important distress leading to deterioration of in-service pavement structures. Different models, including closed form solutions and numerical approaches for prediction of the concrete slab displacements, are introduced and discussed. The effect bond strength between the concrete slab and the subbase layer on concrete slab end movement is investigated using interfacial fracture mechanics concepts. First, the theoretical criteria describing the mechanism of interfacial crack propagation are discussed in a general framework. A modified version of the maximum tangential stress criterion is developed for strong interfaces and it is shown that the proposed model provides more accurate prediction of the experimental data. A new fracture test specimen, which covers all mixed mode conditions, is proposed for evaluation of the bond strength between two dissimilar materials. The new test specimen is then employed for evaluation of the bond strength between the asphalt concrete and the Portland cement concrete.

As the next step, a series of three dimensional finite element simulations are performed to investigate end movements in CRC pavements. The concrete slab/ subbase layer and concrete slab/ reinforcing steel bar interfaces were modelled using a zero thickness cohesive layer which follows traction-separation constitutive law. The results of the finite element simulations are compared with those measured from experiments by

previous researchers. Finally, the effects of CRC dimensions, material properties, bond strength, and environmental loads on the end movements in CRC pavements are explored using three dimensional finite element simulations. The results obtained in the present work can help pavement engineers to better understand the mechanism of end movements in CRC pavements.

DEDICATION

To my beloved wife, Maryam,

To my parents Leila and Mansour, and

To Dr. Isaac Asimov (1920 – 1992).

ACKNOWLEDGEMENTS

First of all, I would like to thank my committee chair, Dr. Zollinger, and my committee members, Dr. Lytton, Dr. Grasley, and Dr. Freed, for their guidance and support throughout the course of this research.

Thanks also go to my friends and colleagues, and the department faculty and staff for making my time at Texas A&M University a great experience.

Finally, thanks to my parents and parents-in-law for their encouragement, my sister, my sister-in-law, and my brother-in-law for continuous concern, and to my wife for her patience and love.

CONTRIBUTORS AND FUNDING SOURCES

Contributors

This work was supported by a dissertation committee consisting of Dr. Zollinger as the committee chair, Dr. Lytton and Dr. Grasley of the Department of Civil Engineering, and Dr. Freed of the Department of Mechanical Engineering.

All work for the dissertation was completed by the student independently.

Funding Sources

This work was made possible in part by funding provided by the Civil Engineering Department and the Transportation Institute of Texas A&M under Grant Number 605221-00001.

The contents of this work are solely the responsibility of the author and do not necessarily represent the official views of the Texas A&M Civil Engineering Department and the Transportation Institute.

TABLE OF CONTENTS

LIST OF FIGURES

LIST OF TABLES

1. INTRODUCTION

1.1. Background

Rigid pavements are widely used in constructing airport fields and major highways, such as those in the interstate highway system. Like flexible pavements, rigid highway pavements are designed as all-weather, long-lasting structures to serve modern day high-speed traffic. Offering high quality riding surfaces for safe vehicular travel, they function as structural layers to distribute vehicular wheel loads in such a manner that the induced stresses transmitted to the subgrade soil are of acceptable magnitudes.

In rigid pavements, the bond behavior between the Portland cement concrete slabs and the subbase layer significantly influences on the displacements in concrete slabs caused by environmental loading as well as the traffic loading. In addition, the bond behavior directly affect on cracking patterns in concrete slabs. The bond strength between the concrete slab and the subbase layer defines the restriction and boundary conditions of the concrete slab, and as a result, plays a significant role in erosion, displacements, and cracking in a pavement structure. Therefore, the study of bond behavior at the interface of the concrete slab and subbase layer is essential to improve our pavement design. An extension in the service life of rigid pavements, which represents a significant portion of the construction industry's efforts, can lead to enormous improvements in the life cycle costs and sustainability of our transportation system. The presented dissertation aims to address the effect of bond behavior at the

interface of concrete lab and subbase, effect of curing conditions, subbase type, and slab dimensions, on end movements and erosion behavior of the slab.

1.2. Objectives

The overarching goals of this research are to evaluate end restraint in concrete pavement system by taking into consideration effects of concrete slab/ subbase resistance, utilizing interfacial fracture mechanics concepts. The bond behavior between concrete slab and subbase can be characterized by the theoretical fracture mechanics concepts. The model used for simulations of the concrete slab/ subbase bond behavior, represents the restriction of a concrete slab at the bottom where it is connected to the subbase layer. Different modeling methods are employed to study end movements (restraints) in concrete slabs including traditional theoretical approaches and finite element simulations. Specific objectives of the current research are as follows:

- **Interfacial fracture criteria**: De-bonding mechanism between the concrete slab and the subbase are addressed in this dissertation using interfacial fracture mechanics approaches. Typically, the interface cracks initiate and propagates at the interface of concrete slab and the subbase due to environmentally induced temperature and moisture gradients effects. Traditional interfacial fracture criteria are discussed and then a new criterion is proposed which provides more accurate predictions for different bonded joints made of different materials. The fracture criteria for weak interfaces are also discussed which can be applied for predictions of the debonding in rigid pavements with weak bond strength.

- **Laboratory testing for evaluation of the bond resistance**: Conducting experiments on laboratory specimens has always been an easier way than in-situ experiments for evaluation of the failure mechanism in structures. Using laboratory specimens, one can simulate different loading conditions, which can take place in a real in-service structure, in a cheaper and faster way. As a part of this research, a new laboratory test specimen is proposed for evaluation of the bond resistance between the concrete slab and the subbase layer. The proposed test specimen can be employed for evaluation of the bond strength at different loading configurations. Utilizing the proposed specimen, the bond strength between Portland cement concrete and asphalt concrete is evaluated at different temperatures, and proper fracture criteria to address de-bonding mechanism are discussed. The aim of this part is to introduce a test method for evaluation of the bond resistance between concrete slab and the subbase layer in a pavement structure.
- **Models for evaluation of the stress, strain, and displacement fields in concrete slabs**: Different models are employed to study stress, strain, and displacement fields in concrete slabs due to the environmental loading. Some traditional methods for evaluation of the displacements in concrete pavements are introduced and discussed. Although such closed form solutions may not be accurate enough, they provide a direct relationship between different design parameters, and as a result, are useful for engineers. Some modifications are then introduced on the traditional analytical models to increase accuracy of the

predictions presented by these models. Furthermore, concrete pavement/ subbase structure is simulated utilizing three dimensional (3D) finite element method. The three dimensional finite element approach is examined by predicting experimental data given in the literature for end movements in concrete slabs.

- **3D finite element modeling of the concrete slab/ subbase structures**: 3D finite element simulations are performed for continuously reinforced concrete (CRC) pavement at different geometries, subbase modulus, bond strength, and environmental loading conditions. The effect of different design parameters are addressed and discussed.

1.3. Structure of the dissertation

This dissertation is composed of seven sections covering three major subjects: development in interfacial fracture mechanics (section 3), laboratory testing of the asphalt concrete/ Portland cement concrete bond strength (section 4), and models for evaluation of the end movements in concrete slabs (sections 5 and 6). The details of each section are as follows:

Section 1: Introduction. This section covers the background, objectives, and methodology of the research.

Section 2: Literature Review. This section presents a literature survey of the main topics studied in this dissertation. Previous research on evaluation of the displacement field in concrete slabs, bond behavior between concrete slab and subbase, and different interfacial fracture criteria are discussed.

Section 3: Interfacial fracture criteria. Different theoretical fracture criteria are discussed for the problem of crack lying at the interface of two dissimilar materials. The bond strength and crack propagation path are discussed using different fracture criteria. A new fracture criterion is developed for debonding of strong interfaces which provides more accurate prediction of the test data available in the literature. Criteria for weak interfaces are also discussed. Finally, some comments are given for crack propagation in a viscoelastic media. The goal of this section is to study interfacial fracture mechanics in a comprehensive framework, in order to be used in next sections for evaluation of the bond strength in a concrete slab/ subbase structure.

Section 4: A new test specimen for evaluation of the interfacial bond strength. In this section, different fracture test specimens for evaluation of the bond behavior between two dissimilar materials are discussed. Then, a new fracture test is suggested which can cover a wider range of the loading configurations, from pure tension to pure shear. The suggested specimen is characterized using finite element simulations. Finally, the bond strength between Portland cement concrete and asphalt concrete is evaluated using the proposed fracture test specimen.

Section 5: Models for the prediction of displacements in CRC pavements. Different model including theoretical ones and 3D finite element one are discussed in this section. Finally, a 3D finite element model is suggested which models cement concrete/ subbase and cement concrete/ reinforcing steel bar bonds using zero thickness cohesive elements. The suggested 3D finite element approach is then examined by the available experimental data in the literature for displacements in concrete slabs.

Section 6: Effect of different factors on the end movements in CRC pavements. A series of 3D finite element simulations on CRC pavement structures under different environmental loading configurations are presented. The effect of geometry, modulus of layers, bond strength and loading profile is studied.

Section 7: Summary, conclusions, and Future Research. This section presents a summary of the major conclusions that can be drawn from this research and discusses future research efforts that can stem from this work.

1.4. Key findings of the research

Important accomplishments of and findings from this research are as follows:

- Different fracture criteria are discussed for evaluation of the bond strength between two dissimilar materials. A modified fracture criterion is suggested which provide more accurate predictions for bond strength as well as the crack propagation direction. Different criteria are compared and discussed for different bonded structures, and some comments are given which can be helpful for designing of the bonded joints.
- Fracture test specimens for evaluation of the bond behavior between two dissimilar bonded materials are discussed. A new specimen is presented and characterized which can be employed for a wide range of the loading configurations. The bond behavior between Portland cement concrete and asphalt concrete is evaluated at different temperatures using the suggested fracture test specimen.

- Different models for evaluation of the displacements in concrete slabs are discussed. Some modifications are given for the traditional theoretical models in order to improve predictions given by these models. The 3D finite element simulation is represented as a more accurate way than traditional methods to predict concrete slab/ subbase stress, strain, and displacement fields.
- 3D finite element simulation is performed for different geometries, subbase modulus, bond strength, and different environmental loading profiles. The effect of each factor on the concrete slab stress and displacement fields is discussed.

2. LITERATURE REVIEW

2.1. Rigid pavements

There are four types of rigid pavements: Jointed plain concrete (JPC) pavement, jointed reinforced concrete (JRC) pavement, continuously reinforced concrete (CRC) pavement, and pre-stressed (PC) concrete pavement. JPC Pavements are plain cement concrete pavements constructed with closely spaced transverse contraction joints. Dowel bars are often used to provide load transfer since aggregate interlock is nearly non-existent for load transfer across the transverse joints (joint spacing usually varies from 4 to 5.5m). CRC pavements are Portland cement concrete pavement with continuous longitudinal steel reinforcement and closely spaced cracks that serve as intermediate transverse expansion or contraction joints. However, the pavement is allowed to crack typically in a random pattern with the notion the cracks will be held tightly closed by the steel reinforcement. In this research we particularly focus on models for prediction of the displacements in CRC pavements.

The first use of CRC pavements was in 1921 by the Bureau of Public Roads on Columbia Pike in Arlington, Virginia. Then, the first significant length of CRC pavements was constructed in the State of Indiana in 1938 (Highway Research Board, 1973 [1]). After that, a good performance of such projects (like the one in Illinois, California, and New Jersey around 1949) led to an increased interest in this design (AASHTO design guide, 1986 [2]). The use of CRC pavements was increased in the 1960s, 1970s, and 1980s during construction of the Interstate Highway System in the

U.S. The use of CRC pavements in the U.S. was increased for more than 15,000 kilometers of equivalent two-lane pavement were in use or under contract at the end of 1971(Highway Research Board, 1973 [1]) and this amount is still increasing. Texas and Illinois, with dissimilar weather and environmental conditions, lead the nation in CRCP usage. Texas constructed its first section in Ft. Worth in 1951. From the 1960s on, Texas has constructed more CRC pavements than any other state, possibly more than all other states combined. Approximately 80 percent of current concrete paving projects let in Texas are CRC pavements. Illinois constructed its first CRC pavement in 1947 on U.S. 40 west of Vandalia. Based on the performance of this experimental project, Illinois began extensive construction of CRC pavements. Approximately two-thirds of the Illinois Interstate system was constructed with CRC pavements [3].

2.2. Slab movements

All Portland cement concrete slabs undergo shrinkage as the concrete ages. This volume change in concrete is very important to the engineer in the design of a concrete slab. This volume change is accommodated by expansion joints and is restricted by the slab's restraints. A concrete slab is restrained by slab/ subbase bond, concrete/ reinforcing steel bar bond, slab's dead weight, etc. In order to design a concrete pavement, stress, strain, and displacement fields are required to be obtained.

In addition to the horizontal shrinkage of the concrete slab, the edges of the slab lift upwards due to the temperature and moisture gradient throughout the slab. In a pavement structure, with respect to temperature, when the slab surface is cooler than the

slab bottom, the surface tends to contract and curling the slab edges (or corners) upward as a result of negative temperature gradient through the slab thickness. On the other hand, the moisture gradient through the thickness induces an additional deformation in the concrete slab, called warping. Such factors are particularly prevalent during the curing stages of a concrete pavement affecting the potential for lift-off (the separation of slab from the subbase layer). Lift-off is the first step towards erosion damage which is a distress type that threatens the sustainability of a concrete pavement. In a concrete slab, the lift-off is controlled by the net climatically induced contraction strain field, which takes into account both temperature and the moisture effects, the bond behavior between concrete slab and subbase, and the weight of the concrete slab. Such interaction causes a stress field throughout the slab which results in separation of the slab from the subbase.

In this research, we particularly study end movements in CRC pavement which is widely used in construction of pavement structures and was developed as an alternative to jointed concrete pavement to eliminate the need for contraction joints. In fact, the study of CRC pavements provides a more general solution since the end movement in a plain concrete slab is a particular case of this problem. In CRC pavement, the longitudinal reinforcement is continuous and each individual length of the reinforcing bar is tied each of its adjoining bars in the reinforcement net. The steel keeps the cracks tightly closed maintaining the integrity of the aggregate interlock across the cracks. Over the years, the mechanism of the slab deformation due to such environmental effects has been investigated by many researchers. Palmer [4] studied stress, strain and displacement field in CRCP. He calculated relative displacements between concrete slab and subgrade, and

between concrete slab and reinforcing steel bar. However, he did not consider effect of lift-off on the slab end movement and did not take into account the effect of interface crack propagation.

McCullough and his colleagues [5, 6] developed CRCP-11 to design concrete pavement under different climatic conditions. The software was a sophisticated tool for pavement design considering predicted minimum concrete temperatures for the medium and long terms which allows a reasonable economical designs. Zhang [7] studied the effects of base characteristics on curling stresses of CRCP under different types of base materials. He studied the effects of six typical bases on curling stresses of CRCP subjected to temperature variations using a 2D finite-element method. However, he used a simple friction model for concrete slab/ subbase and concrete/ reinforcing steel bar interfaces which does not take into account any cohesion at the interfaces.

In addition to the horizontal displacements of the concrete slab, the vertical movements (lift-off) is also considered as one of the important parameters in design of concrete pavements, and as a result, needs to be evaluated. The lift-off in concrete slabs has been investigated by many researchers so far, by taking into consideration effects of curling and warping, together and separately [8 – 17]. A pioneering work has been done by Westergaard [8] on the thermal stress field analysis in rigid slabs due to their curling. He presented a linear elastic solution for the slab curling assuming a linear temperature gradient through the slab thickness and an elastic Winkler foundation for the subgrade. Tang et al. [9] suggested an analytical approach to evaluate stress and displacement distribution in a semi-infinite slab and in an infinitely-long slab of a finite width. They

also considered the effect of gap that may occur under the concrete slab resulting from curling and proposed an approximate formula for the maximum stress in a finite slab. However, the net effects of curling and warping causes the lift-off in concrete slab pavements. In this regard, Bari and Zollinger [10] proposed a new framework to model the effects of the concrete slab/subgrade interface for design purposes considering short- and long-term performance. They studied the effect of interfacial adhesion as well as the sliding friction on the interfacial resistance and the slab lift-off. However, in practice, cracks propagate at the interface of the concrete slab and subbase and none of the above models can present a sophisticated method to describe interface crack propagation mechanism.

2.3. Factors affecting displacements in concrete slabs

There are many factors influencing displacements in concrete pavements. Among them are temperature, moisture, material properties of the slab and subbase, bond behavior between slab and subbase, and percentage and position of the steel reinforcement. A literature survey is provided in the following addressing some of the recent works to evaluate displacements in concrete slabs.

2.3.1. Temperature change in a concrete slab

Thermally induced stresses are one of the primary sources of the stresses in concrete slabs. In CRC pavements, the thermal stress depends on (1) the thermal properties in early aged concrete which can be often characterized by the heat of

hydration; (2) the environmental effects in aged concrete (ambient air temperature and solar radiations); (3) geometry of the structure (zero-stress point). The thermal stress field in a concrete slab is influenced by the structural boundary conditions of the slab. If a concrete slab is unrestrained, it expands and contracts during heating and the subsequent cooling process without stress development. However, concrete slabs are always restrained to some degree, either externally by adjoining structures or internally by a variation in temperature vertically in the slab itself. Therefore, due to such imposed restraint conditions, temperature change results in compressive and/or tensile stresses in the concrete. Thus, a primary question would be, whether the induced thermal stresses lead to cracking or not [18].

Due to the hydration of fresh concrete, energy releases in the form of heat. The primary heat generation cycle actually starts often the dormant period while the calcium ions concentration builds up. During this period, the concrete is in a plastic state and is relatively inactive reaction-wise. A couple of hours after the end of the dormant period, the peak of the primary cycle is reached. At this point, the major portion of the hydration products crystallize from the solution of the mixture. This is when the time of initial and/or final set of the concrete occurs. As hydration products grow, they form a barrier to the movement of the calcium ion when the availability of calcium diminishes, the reaction drops down and hydration may eventually stop [3, 20]. The rate of hydration is very sensitive to initial temperature, especially during the primary cycle [3, 20]. Therefore, the temperature cycle during construction is an important factor affecting the rate of hydration.

The coefficient of thermal expansion (COTE) is also a key parameter affecting on the thermal stress distribution in both hardening and hardened concrete slabs. Like all composite materials, the COTE of concrete is influenced by a large number of factors that can be generally related to its major components: cement paste and aggregate. The thermal characteristics of concrete obviously affect the crack pattern in concrete slabs since thermally induced dimensional changes in the Portland cement concrete influence the formation of transverse cracks. The type of coarse aggregate also directly influences on COTE of concrete, because coarse aggregates form a large part of concrete by volume [21].

The COTE of concrete is approximately equal to the volumetrically weighted average of the coefficients of its ingredients [3]. It is needed to calculate the thermal strains and stresses of concrete slabs. The COTE of concrete has been measured by many researchers so far [22 – 25] and varies within 2.78 – $8.33\times10^{-6}/^{o}F$, depending on aggregates, constituents and the moisture state of concrete [23]. It also has been reported in the literature that the COTE of concrete is slightly greater during heating than cooling and its value at early-ages is higher than that of mature concrete [23 – 29]. In this study, however, the coefficient is assumed to be constant over time since the early-age behavior is not studied.

2.3.2. Concrete shrinkage

Since concrete is largely composed of water, the water transport and change in amount of water significantly influence in volume change of concrete. In other words,

water-related shrinkage is a volumetric change caused by loss and movement of the water (i.e., change in the internal pore pressure caused by drying or self-desiccation). Drying of concrete is affected by the environmental conditions in which the relative humidity of the concrete attempts to equilibrate with the humidity of the surrounding environment. As the internal humidity strives to equilibrate with a lower environmental humidity, water is evacuated from the capillary pores which results in the development of tensile stresses. This tensile stress is attributed to the compressing the rigid skeleton of concrete which provides a partial explanation for the effect we commonly refer to as drying shrinkage. Shrinkage in concrete can be classified into the following types:

Drying shrinkage is by far the most common cause of shrinkage. The drying shrinkage of concrete is analogous to the mechanism of drying of timber specimen. Under drying conditions, the gel water is lost progressively over a long time, as long as the concrete is kept in drying conditions. One of the most substantial factors influencing free shrinkage is the water to cement ratio (w/c). The w/c required for complete hydration is typically assumed to be approximately 0.42 depending on the amount of gel porosity that is assumed [30]. The amount of water has a direct influence on the size and magnitude of the porosity (i.e., higher w/c pastes have higher porosity). Therefore, theoretically, specimens with a lower w/c have a lower amount of pore water and consequently exhibit lower drying shrinkage (practically, there is an optimum value for w/c). Currently, the Texas Department of Transportation (TxDOT) limits the water-to-cement ratio to a maximum 0.45 for paving concrete [3].

Aggregate gradation does not directly influence shrinkage [31], however, it may be concluded that the use of higher aggregate volume exhibits lower free shrinkage since the aggregate is generally dimensionally stable. Aggregates with higher stiffness exhibit lower free shrinkage based on the same reasoning. The use of high porosity lightweight aggregate (LWA) has also been suggested as one method to minimize autogenous shrinkage [32, 33]. For this purpose, the LWA is saturated to various degrees before using and the aggregate acts as a water reservoir to supply water that counteracts the self-desiccation of the paste.

Autogenous shrinkage occurs in a conservative system, like sealed concrete (i.e., no moisture loss) without temperature change. This type of shrinkage is caused by cement hydration and seen as the external, macroscopic volume change of cementitious materials after initial set, without any "exchange" with the environment. This exchange is either of substances (moisture), a temperature variation or an external load or restraint.

Plastic shrinkage is a term used for freshly poured concrete and manifests itself soon after the concrete is placed in the forms while the concrete is still in the plastic state. This type of shrinkage occurs when the rate of loss of water from the surface exceeds the rate at which the bleeding water is available. Environmental considerations including wind speed, solar effects, low relative humidity, and high temperature significantly influence the potential of plastic shrinkage cracking [29].

2.3.3. Material properties

The material properties of the concrete slab, subbase layer, and reinforcing steel significantly influences displacements in pavement structures. For concrete slab, the material properties of the concrete ingredients (cement past and aggregates) represents the effective modulus of the concrete. The stiffness and strength of each component influences crack pattern in a concrete slab and therefore are essential to be studied. The stiffness of each layer in a concrete pavement structure directly relates to the displacements in the structure. The effect of stiffness of layers on the displacement field in concrete slabs has been investigated by the researchers in the past [34 – 36]. In the previous research, the concrete slab and base layer are modelled as linear elastic plates connected by springs (Winkler foundation) and the displacements in the pavement is evaluated by plate theories (like Mindlin plate theory). However, the concept of using springs as interface elements brings many problems since such spring models do not represent de-bonding mechanism between layers in a sophisticated manner. The displacements in a concrete slab are developed in either elastic deformations or de-bonding (slip deformations). However, a sophisticated model representing both de-bonding and elastic deflections has not been developed yet.

2.3.4. Bond behavior between concrete slab and subbase

The presented dissertation aims to provide researchers with some insight as to the effect of bond behavior at the interface of concrete lab and subbase, curing conditions, and the relative stiffness on the end movement of the slab, and to answer some of the

primary questions on the mechanism of end movement in concrete slab/ subbase structures. Therefore, a literature survey is necessary to briefly review of the previous works in this field. The bond behavior between the Portland cement concrete slabs and the subbase layer significantly influences on horizontal displacements in concrete slabs caused by environmental loading as well as the traffic loading. In addition, the bond behavior directly affects on both cracking patterns in concrete slabs. Therefore, the study of bond behavior at the interface of the concrete slab and subbase layer is essential to improve our pavement design. In other words, an extension in the service life of rigid pavements, which represents a significant portion of the construction industry's efforts, can lead to enormous improvements in the life cycle costs and sustainability of the transportation system.

The bond strength of the Portland cement concrete/subbase has rarely been investigated. A limited number of published works can be found in the literature for the shear strength and tensile strength of the Portland-cement concrete/asphalt concrete bonded joints, with and without interface cracks [37 – 47]. Chabot et al. [42] conducted a set of experiments to investigate mixed mode interfacial fracture in asphalt concrete/ Portland cement concrete bonded joints. They used four point bend specimens for their fracture tests and obtained strain energy release rate under different loading and boundary conditions. Tschegg et al. [43] dealt with the testing and assessment of the bond behavior and the crack resistance of asphalt-concrete interfaces tested at different temperatures. They conducted their tests at different pretreatments of the interface: without any treatment, using cement grout, using a combination of cement grout and

synthetic dispersion, or using only synthetic dispersion. Pouteau et al. [45] studied the fatigue life of a concrete layer bonded to an asphalt subbase. They presented an in situ experiment aiming to evaluate the growth of a defect at the interface of a CRC pavement bonded to an asphalt subbase under traffic loads. They also suggested a new laboratory test to study the initiation and the propagation of the crack at the interface. However, all previous works failed to obtain fracture toughness under different mixed mode conditions because of the limitations on the specimen geometry. The finite element simulation of the crack propagation at the interface of concrete slab and subbase has also rarely been investigated by the researchers [46, 47]. For instance, Mirsayar et al. [46] conducted a series of finite element simulations to investigate effect of subbase modulus and environmental loadings on the interface crack propagation between plain Portland cement concrete slabs and the subbase. However, they used a two dimensional model and did not considered the bond strength effects. Kim et al. [48] conducted a series of finite element simulations to study bond behavior between the concrete slab and the base. They also performed a sensitivity analysis to investigate the effects of overlay and CRC pavement parameters, such as elastic modulus, thickness, coefficient of thermal expansion and percent reinforcement, on the interfacial shear and normal stresses. They have incorporated their mechanistic model into the HIPERBOND software developed for the FHWA. Totsky [49] developed a model in which a multilayered system resting on subgrade was modelled as series of springs and plates where curling was analyzed iteratively. In this model, the springs that were in tension are removed as the pavement section curls allowing for the system to be reanalyzed to determine the equilibrium

condition. The removal of the interfacial springs during the solution process represented the layer separation. However, the presented model was not able to obtain curling and warping effects. Also, the bond between reinforcing steel bar and the concrete was simulated as a simple shear model which does not consider effect of cohesion.

2.4. Fracture criteria for bonded structures

End movements of a concrete slab consists of both contraction shrinkage and slab lift – off action. Such movements is accompanied with de-bonding of the slab from subgrade when the net induced climatically strain field in the concrete slab exceeds a critical value. In traditional models, de-bonding of the concrete slab from subbase is considered as a simple friction model which does not consider effect of cohesion between the concrete and the subbase. However, a sophisticated model should be able to take into account both tensile and shear stress components at the interfaces. The interfacial fracture mechanics can be utilized to simulate de-bonding at the interface under combined shear/ tensile stresses at the interface. The process of crack initiation and propagation at the interface of two dissimilar materials has widely been studied in the past [50 – 59]. Depending on the bond strength, the mechanism of interfacial crack propagation can be classified into two types: strong interfaces, and weak interfaces. In strong interfaces, the crack kinks into the weaker material, and for weak bonds, the interface crack propagates through the interface. The fracture criteria for strong and weak interfaces are different from each other. For strong interfaces, fracture criteria deals with material properties of both bonded materials. However, for weak interfaces,

the strength of the bond itself is more important than mechanical properties of the each material. There are many published works in the literature by the previous researchers on the study of crack propagation at strong interfaces. He and Hutchinson [50], presented an energy based framework for crack propagation at the interface of two dissimilar elastic solids. Hurd et al. [51] studied the mechanism of fracture at the strong interface of silicon and glass. They measured the mode I fracture toughness and kinking angles using a compact tension test specimen. Martinet al. [52] carried out an asymptotic analysis to model the mechanism of deflection of a crack at an interface in a brittle bi-material system. Using the energy release rate concept, they found that in the case of a stationary crack impinging perpendicularly on the interface and submitted to progressive loading, the energy criterion depends on the elastic mismatch of the bi-material constituents and the ratio of the crack extensions in the deflected and the penetrated directions. Evans et al. [53] studied fracture energy of a bi-material system and found that the fracture energy is not unique and usually exhibits values substantially larger than the thermodynamic work of adhesion. Mirsayar [55] recently proposed a new stress-based fracture criterion for crack kinking out of the interface which can be applied for bonded structures with strong interfaces. He found that not only the singular stress terms, but also the first non-singular stress term of the asymptotic series expansion influences on the fracture behavior of interface bonds.

One can also find a lot of published works in the literature for analysis of bond behavior of weak interfaces [56 – 62]. Fernlund and Spelt [56] proposed a new jig for mixed mode fracture testing of adhesively bonded joints and conducted a set of fracture

tests on different bonded structures to obtain their fracture toughness. Campilho et al. [57] studied the ability of extended finite element method to predict the fracture behavior of thin layers of adhesive between stiff and compliant adherends. Choupani and his coworkers [60 – 62] investigated the mixed mode crack propagation in adhesively bonded joints, made of various combination of the materials, experimentally.

The type of the specimen has always been an important factor for conducting research on the fracture properties of different materials. There are some important factors which are needed to be considered for choosing a fracture test specimen. A fracture test specimen should be: (1) manufactured easily, (2) should be able to be loaded easily, and (3) cover all loading configurations from pure mode I (opening mode) to pure mode II (sliding mode). However, many of the fracture tests proposed by the previous researchers are not able to cover all mixed mode conditions. One can find several fracture test specimens in the literature such as compact tension (CT), three point bend (3PB), four point bend (4PB), Brazilian disk (BD), semicircular bend (SCB), and double cantilever beam (DCB). Some of them, like BD, can cover form pure mode I to pure mode II conditions. However, for a bi-material system, we can rarely find a specimen in the literature satisfying all three conditions mentioned above for a proper fracture test specimen. One of the aims of the current research is to develop a new specimen covering different mixed mode conditions from pure mode I to pure mode II for an interface crack.

2.5. Summary of the review

According to the field observations, a concrete slab on certain types of bases are bonded together and as a result, cracks initiate and propagate through the interface during the slab shrinkage. In the central portions of a slab, the interface is likely fully bonded either due to chemical adhesion or high frictional restraint or both. These conditions often exist in push-off or lab friction tests which have been common methods to measure the coefficient of friction but are frequently plagued by shear failure planes forming in the matrix of the subbase layer complicating the determination of the friction values (see Figure 2-1a). The adhesive aspects of interfacial resistance have largely been thought to be a factor during construction where it has on occasion been the source of cracking problems. If the mechanical and/or adhesive resistance is too high initially, random cracking may be initiated at the bottom rather than the top of the slab during the early life of a jointed pavement – which is often a problem associated with the control of cracking during sawcutting operations since the notches are placed at the surface of the pavement. High bond resistance can also be a problem in CRC pavement construction (see Figure 2-1b) but in a sense opposite of what happens in jointed pavement construction where cracking development is inhibited too much.

Depending on the material properties of the subbase layer, the interface crack may kink into one of the materials (strong interface) or propagate through the interface (weak interface). Both cases could happen depending on the degree of bond between subbase and concrete slab. As will be described later, the possibility of crack propagation through the interface increases at lower temperatures for a given concrete

slab/ subbase structure. Also, the fracture criteria for evaluation of the interfacial crack propagation are different for weak and strong interfaces.

(a) (b)

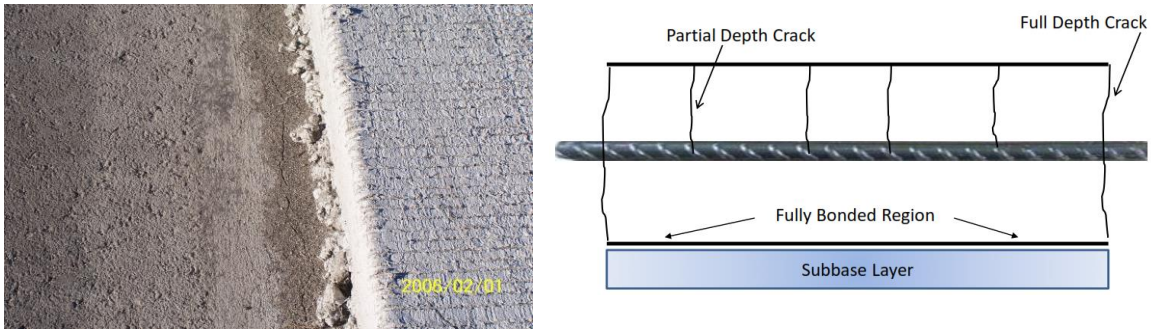

Figure 2-1. (a) Example of shear failure below the slab/subase interface (b) Partial-depth cracking in a longitudinal segment of CRC pavement.

The previous methods for bond behavior assumes that slab and subgrade are sliding with respect to each other and do not take into account the effect of interface crack in their bond model. However, the cracks developed at the interface of subbase layer and concrete slab cause to the stress concentration which influences on the delamination behavior, and can be addressed by the interfacial fracture mechanics.

As discussed in the literature review, a proper criterion has not been developed so far to investigate bond behavior between concrete slab and subbase. One of the goals of the current dissertation is to find a suitable fracture criterion to address the fracture behavior of the interface bond between concrete slab and the base layer.

In this dissertation, the aim is to address end movements in slabs (placed on the subgrade) utilizing interfacial fracture mechanics concepts. The slab displacements and

stresses due to the net environmental loading as well as the bond behavior between concrete slab and subbase layer is evaluated using finite element simulations. Some comments and modifications are also given and discussed for the previous simplified closed form solutions. This dissertation particularly investigates the bond slip between the concrete slab and subbase layer. The effect of slab lift-off is taken into account which has not been considered in previous works. The effects of materials property, geometry, reinforcing steel bar, and curing conditions on the bond slip between slab and subbase will be studied in this approach. The results of this research would be useful for design optimization of the slab/ subbase structures at different climatic conditions.

3. INTERFACIAL FRACTURE CRITERIA[*]

3.1. Introduction

Bi-material joints such as composite/ metal, ceramic/ metal, and ceramic/ ceramic materials are extensively used in many industrial applications. Some well-known examples are: the silicon carbide/ titanium (Sic/ Ti) fasteners in aircrafts [63], silicon/ glass joints in micro-electro-mechanical systems (MEMS) [64], fiber/ matrix joints in composite structures [65 – 67], pavement structures [45 – 47], and rock/ concrete interfaces in dams [68]. In structures containing bi-material joints, the existence of cracks at the interface is inevitable because of the high local stress rise resulting from material discontinuity and/ or geometrical conditions. These interface cracks can be created during both the bonding process and service life of the structures. The presence of cracks in structures containing such bi-material joints significantly influences load bearing capacity and may finally result in detachment. Therefore, the fracture behavior of bi-material cracks is an important issue. Under external mechanical and/ or thermal loading condition, interface cracks may grow through the interface or kink into one of the materials. When an interface bond is strong, for instance, silicon/ glass anodic bonds in MEMS, the crack may kink into one of the materials instead of growing through the interface. In fact, as the bi-material cracks are often subjected to mixed mode (opening and sliding) loading conditions, the crack growth is most likely to propagate into one of

[*] Part of the results reported in this section are reprinted with permission from "On fracture of kinked interface cracks–The role of T-stress" by MM Mirsayar, 2014. Materials & Design, 61, 117-123, Copyright 2014 by Elsevier and "The role of T-stress on kinking angle of interface cracks" by MM Mirsayar and P. Park, 2015. Materials & Design, 80, 12-19, Copyright 2015 by Elsevier.

the materials. The prediction of the crack propagation direction is essential to understand the fracture behavior of the bi-material joints subjected to the mixed loading conditions. For strong interfaces, different fracture criteria are proposed so far based on energy release rate concept, and tangential stress concept as discussed in the followings.

Several fracture criteria have been suggested for evaluating fracture behavior of notches and cracks in homogeneous bodies as well as interface cracks existing between two dissimilar materials [69 – 78]. A recent and comprehensive review on brittle fracture criteria can be found in Breto and Lazzarin [71]. In agreement with the pioneering work done by Williams [69] for the interface crack, Dempsey and Sinclair [70] studied the stress singularities in the plane elasticity of the composite wedge. Strain energy release rate, is one of the popular choices as a fracture parameter to characterize the fracture of bi-material cracks [79 – 81]. However, the strain energy release rate is not able to show the participation of each fracture mode (opening, mode I and sliding, mode II) as well as the T-stress clearly. Yuuki and Xu [82] have suggested a fracture criterion for bi-material cracks based on maximum tangential stress (MTS) concept. According to their proposed criterion, a mixed mode crack at a bi-material interface propagates in the direction, at where the tangential stress reaches its maximum value. They have indicated that MTS criterion, which had been used previously for simple crack (cracks in homogeneous media) [83], is capable of successfully predicting the fracture behavior of bi-material cracks. The advantages of their criterion to the previous ones was its simplicity and the ability of considering the role of each fracture mode separately. Nevertheless, their criterion was limited to special combination of materials (specific

ranges of bi-material constant, ε). In addition, they only used the singular solution (the terms associated with stress intensity factors), and did not consider the effect of the T-stress (first non-singular stress term) and higher order terms.

Recent studies on notches and cracks in homogeneous bodies or bi-material interfaces have shown that the first non-singular stress term of elastic stress field can play an important role in stress distribution and fracture behavior at the vicinity of such sharp corners [84 – 92]. For example, Smith et al. [89] revisited the MTS criterion for homogeneous cracks, and studied the effect of the first non-singular stress term of the elastic stress field (T-stress) on the fracture initiation angle and fracture load. They have shown that the T-stress has an important role in the fracture initiation angle as well as the fracture load, and neglecting this term may cause significant error in using of the MTS criterion. For bi-material cracks, Dreier and Schmauder [90] presented an analytical equation for calculation of the T-stress due to the thermal residual stresses. Li and Xu [91] also studied the variation of T-stress before and after kinking of a bi-material crack between two elastic solids. Nevertheless, a stress-based fracture criterion considering the effect of T-stress for a bi-material crack tip has not been suggested until Mirsayar [93]. As a part of the current section, the criterion suggested by Mirsayar [93] will be presented.

In all criteria mentioned above, the interface is assumed to be strong enough so that the cracks kink into one of the materials instead of propagating through the interface. For a weak interface, where the bond strength is weaker than ultimate strength of each bonded materials, an interface crack propagates through the interface instead of

kinking into one of the materials. There are very limited mechanistic based fracture criteria in the literature addressing the interfacial de-bonding of weak interfaces. One of the most popular criteria for weak interfaces is the critical stress intensity factor. For mixed mode conditions, this criterion can be written in form of a power law equation. This criterion has widely been used by many researchers so far to investigate bond strength of many engineering materials [60 – 62]. This section of the dissertation deals with different fracture criteria for both strong and weak interfaces. Also, a new stress based fracture criterion is presented for evaluation of the experimental data for strong interfaces.

3.2. Fracture criteria for strong interfaces

3.2.1. General remarks

A typical bi-material interface crack between two homogeneous and isotropic elastic solids with three possible fracture paths is illustrated in Figure 3-1. The elastic stress field in the vicinity of the bi-material crack tip can be represented as [94]:

$$\sigma_{rr}^{(m)} = \frac{K_I}{\sqrt{2\pi r}} f_{rr\_1}^{(m)}(\ln\left[\frac{r}{L}\right], \varepsilon, \theta) + \frac{K_{II}}{\sqrt{2\pi r}} f_{rr\_2}^{(m)}(\ln\left[\frac{r}{L}\right], \varepsilon, \theta) + 4\frac{T}{R^{(m)}}\cos^2(\theta) + H.O.T$$

$$\sigma_{\theta\theta}^{(m)} = \frac{K_I}{\sqrt{2\pi r}} f_{\theta\theta\_1}^{(m)}(\ln\left[\frac{r}{L}\right], \varepsilon, \theta) + \frac{K_{II}}{\sqrt{2\pi r}} f_{\theta\theta\_2}^{(m)}(\ln\left[\frac{r}{L}\right], \varepsilon, \theta) + 4\frac{T}{R^{(m)}}\sin^2(\theta) + H.O.T \quad (3.1)$$

$$\tau_{r\theta}^{(m)} = \frac{K_I}{\sqrt{2\pi r}} f_{r\theta\_1}^{(m)}(\ln\left[\frac{r}{L}\right], \varepsilon, \theta) + \frac{K_{II}}{\sqrt{2\pi r}} f_{r\theta\_2}^{(m)}(\ln\left[\frac{r}{L}\right], \varepsilon, \theta) - 4\frac{T}{R^{(m)}}\sin(\theta)\cos(\theta) + H.O.T$$

where, m=1, 2 denotes material number, r and θ are the variables of the polar coordinate with the origin at the crack tip. $\sigma_{rr}^{(m)}, \sigma_{\theta\theta}^{(m)}$, and $\tau_{r\theta}^{(m)}$ are the radial, tangential, and shear stresses of the material m, respectively. The parameter L is a characteristic length [95, 96], and $R^{(m)}$ is the material parameter defined as follows:

$$R^{(1)} = \sqrt{2\pi}\left(1+\frac{1+\kappa_1}{1+\kappa_2}\frac{G_2}{G_1}\right)$$
$$R^{(2)} = \sqrt{2\pi}\left(1+\frac{1+\kappa_2}{1+\kappa_1}\frac{G_1}{G_2}\right) \tag{3.2}$$

where, G_m is the shear modulus, the parameter κ_m equals $3-4\nu_m$ for plane strain condition and $(3-\nu_m)/(1+\nu_m)$ for plane stress condition, and ν_m is Poison's ratio. The bi-material constant, ε, is defined as:

$$\varepsilon = \frac{1}{2\pi}\ln\left(\frac{G_2\kappa_1+G_1}{G_1\kappa_2+G_2}\right) \tag{3.3}$$

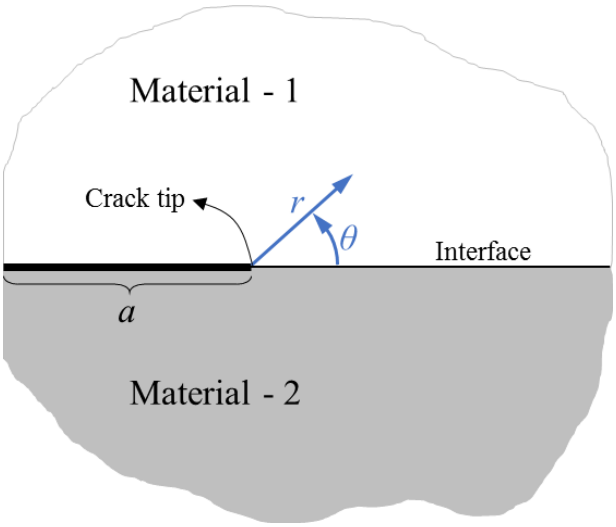

Figure 3-1. Configuration of a bi-material interface crack between two homogeneous and isotropic elastic solids.

The parameters f_{rr}, $f_{\theta\theta}$ and $f_{r\theta}$ in Eq. (3.1) are known functions of $\ln[r/L]$, θ and ε (see appendix A for more details). The coefficients K_I and K_{II} are stress intensity factors associated with the mode I (opening and mode II (sliding), respectively, and T is the T-stress. The first and the second terms represent the singular stress field (when $r \to 0 \Rightarrow (1/\sqrt{r}) \to \infty$) and, the T – stress is the first nonsingular stress term.

The general form of the mixed mode brittle fracture criteria is presented in Eq. (3.4), since the elastic stress, strain and displacement field around crack tip can generally be controlled by K_I, K_{II}, the higher order terms (H.O.T), and material properties.

$$\begin{cases} \theta_0 = g(K_I, K_{II}, H.O.T, r, \varepsilon) \\ h(K_I, K_{II}, H.O.T, r, \varepsilon) = C \end{cases} \tag{3.4}$$

where, θ_0 and C are direction of the crack propagation and a critical value of the material constant (critical stress/ strain/ initiation energy), respectively and h and g are functions to be determined. It will be shown later in this dissertation that the term corresponding to the T parameter plays the most important role in the brittle fracture behavior of the materials, and the higher order terms can be neglected in most cases. It should be noted that pure modes and mixed mode conditions are special cases of Eq. (3.1) and also, the T parameter is not considered in traditional criteria. In the following, the minimum strain energy density (SED) criterion, the maximum energy release rate (G) criterion, the maximum tangential stress (MTS) criterion, and the maximum tangential strain (MTSN) criterion are briefly explained. Then, the MTS criterion is described in more detail, and finally, a modified version of MTS is presented which can provide more accurate predictions of the fracture test data.

3.2.2. Minimum strain energy density (SED) criterion

The SED criterion was first proposed by Sih [83] for a crack problem in a homogeneous media and claims that the crack propagates in direction where the strain energy density, *S*, reaches its minimum value. The strain energy density around the crack tip can be given as;

$$\frac{S}{r} = W = \frac{1}{2}\sigma_{ij}\varepsilon_{ij} \tag{3.5}$$

where, σ_{ij} and ε_{ij} $(i,j = r,\theta)$ are the stress and strain components, respectively. The criterion can be presented as shown in Eq. (3.6) and (3.7).

$$\left.\frac{\partial S}{\partial \theta}\right|_{\theta=\theta_0} = 0 \ , \qquad \left.\frac{\partial^2 S}{\partial \theta^2}\right|_{\theta=\theta_0} > 0 \tag{3.6}$$

$$S_{\min} = S\big|_{\theta=\theta_0} = S_C \tag{3.7}$$

where S_C is the critical value of the strain energy density factor. For an interface crack, however, the crack kinks into the weaker material (material *m*) for strong interfaces. The strain energy density can then be expressed in terms of the stress components as;

$$S = \frac{1}{2G}\left\{\frac{\kappa^{(m)}+1}{8}(\sigma_{rr}^{(m)} + \sigma_{\theta\theta}^{(m)})^2 - \sigma_{rr}^{(m)}\sigma_{\theta\theta}^{(m)} + (\tau_{r\theta}^{(m)})^2\right\} \tag{3.8}$$

Where, $\kappa^{(m)}$ equals to $3 - 4\nu^{(m)}$ and $(3 - \nu^{(m)})/ (1 + \nu^{(m)})$, for plane strain and plane stress, respectively. The traditional SED criterion only considers singular stress terms which are corresponding to K_I and K_{II}.

3.2.3. Maximum energy release rate (G) criterion

The energy release rate can be expressed in form of the Eq. (3.9) if one assumes that crack propagates a unit length along its extension.

$$G = \frac{1}{E^*}[(K_I)^2 + (K_{II})^2] \tag{3.9}$$

where $E^* = E$ for plane stress conditions, and $E^* = E/(1-\nu^2)$ for plane strain conditions. However, the crack does not propagate along its extension line under mixed mode condition. The modified version of this criterion was then suggested by Hussain et al. [97] by omitting this limitation. The modified criterion states that fracture occurs at the crack tip in direction where the energy release rate reaches its maximum. The proposed criterion by Hussain et al. [97], is based on the released energy when a crack propagates a kinked unit length, under mixed mode conditions. The criterion can be presented as;

$$\theta_0 = \theta\big|_{G_\theta = G_{\theta,\max}}, \qquad G_{\theta,\max} \geq G_C \tag{3.10}$$

However, the calculation of the G_θ parameter is not an easy task. The G_θ parameter can be expressed as Eq. (3.11) if the crack propagates in direction of θ from crack tip in a unit length of Δa.

$$G_\theta = \lim_{\Delta a \to 0} \frac{1}{2\Delta a} \int_0^{\Delta a} \frac{1}{2} \left\{ \sigma_{\theta\theta}(a)\delta_\theta(a+\Delta a) + \sigma_{r\theta}(a)\delta_r(a+\Delta a) \right\} d\eta \tag{3.11}$$

where, $\delta_k \quad (k = r, \theta)$ is the opening displacement of the kinked crack face in *k* direction. It can be shown that the close form mathematical expression for G_θ is nearly impossible and may lead to lose its physical meaning when $\Delta a \to 0$. Because the G_θ parameter can only be calculated using a huge numerical analysis, many of researches prefer to use expression given in Eq. (3.11) when $\Delta a \to 0$. Although the concept is presented for homogeneous media, it can be extended for a bi-material crack problem if we use stress field given in Eq. (3.1). The concept of G criterion can also successfully describe delamination problem if the interface crack does not kink into the materials (weak interfaces).

3.2.4. Maximum tangential stress (MTS) criterion

According to the MTS criterion, an interface crack propagates in the direction where the tangential stress $\sigma_{\theta\theta}^{(m)}$ reaches its critical value $\sigma_C^{(m)}$ at a critical distance of $r_c^{(m)}$ from crack tip [82, 83]. The critical distance, $r_c^{(m)}$, defines the size of crack process zone in brittle materials, and is known to be a material property independent from loading and boundary conditions. The critical distance, $r_c^{(m)}$, is defined as follows [95, 96]:

$$r_c^{(m)} = \frac{1}{2\pi}\left(\frac{K_{IC}^{(m)}}{\sigma_C^{(m)}}\right)^2 \tag{3.12}$$

where, $\sigma_C^{(m)}$ and $K_{IC}^{(m)}$ are the tensile strength and mode I fracture toughness of material *m*, respectively. It is worth mentioning that in some models, the physical length scale is

related to the microstructure of the materials (such as grain size or inclusion spacing). However, these micromechanistic models are not considered in the form of presented in Eq. (3.12) and the length scale used for this equation utilizes continuum mechanics models [96].

According to the MTS criterion, the direction of crack propagation, $\theta_0^{(m)}$, at where $\sigma_{\theta\theta}^{(m)}$ becomes maximum, can be determined from the following conditions:

$$\begin{cases} \left(\dfrac{\partial \sigma_{\theta\theta}^{(m)}}{\partial \theta} \right)_{r_c^{(m)}, \theta_0^{(m)}} = 0 \\ \left(\dfrac{\partial^2 \sigma_{\theta\theta}^{(m)}}{\partial \theta^2} \right)_{r_c^{(m)}, \theta_0^{(m)}} < 0 \end{cases} \tag{3.13}$$

By applying these conditions to the extended form of tangential stress, $\sigma_{\theta\theta}^{(m)}$, described in Eq. (3.1), the kinking angle, $\theta_0^{(m)}$, can be obtained as shown in Eq. (3.14):

$$\begin{aligned} &\frac{\partial \sigma_{\theta\theta}^{(m)}}{\partial \theta} = 0 \rightarrow \frac{K_I}{\sqrt{2\pi r_c^{(m)}}} \frac{\partial f_{\theta\theta\_1}^{(m)}}{\partial \theta} + \frac{K_{II}}{\sqrt{2\pi r_c^{(m)}}} \frac{\partial f_{\theta\theta\_2}^{(m)}}{\partial \theta} = 0 \quad \rightarrow \quad \theta_0^{(m)} \\ &\left(\frac{\partial^2 \sigma_{\theta\theta}^{(m)}}{\partial \theta^2} \right)_{r_c^{(m)}, \theta_0^{(m)}} < 0 \end{aligned} \tag{3.14}$$

Using Eq. (3.1) and substituting only singular stress terms into Eq. (3.14), one can find the relationship between stress intensity factors at onset of fracture initiation with the critical tangential stress as:

$$\sqrt{2\pi r_c^{(m)}}\, \sigma_c^{(m)} = K_I f_{\theta\theta\_1}^{(m)} + K_{II} f_{\theta\theta\_2}^{(m)} \tag{3.15}$$

The parameters $f_{\theta\theta\_1}^{(m)}$ and $f_{\theta\theta\_2}^{(m)}$ should be defined at $\theta = \theta_0^{(m)}$ (see appendix A). The left hand side of the Eq. (3.15) equals to mode I fracture toughness, $K_{IC}^{(m)}$, of each material based on linear elastic fracture mechanics concept (see Eq. (3.12)). Therefore, the Eq. (3.15) could be rewritten as Eq. (3.16) to represent the MTS criterion for bi-material cracks.

$$K_{IC}^{(m)} = K_I f_{\theta\theta\_1}^{(m)} + K_{II} f_{\theta\theta\_2}^{(m)} \tag{3.16}$$

3.2.5. Maximum tangential strain (MTSN) criterion

The MTSN criterion, states that crack propagates in the direction, θ_0, where the tangential strain, $\varepsilon_{\theta\theta}$, reaches its maximum value, ε_T, at a critical distance, r_c, from the crack tip. The criterion was first proposed by Chang [98] for homogeneous media, but it could simply be represented for an interface crack as:

$$\begin{cases} \left.\dfrac{\partial \varepsilon_{\theta\theta}^{(m)}}{\partial \theta}\right|_{r=r_c^{(m)};\theta=\theta_0^{(m)}} = 0 \\ \left.\dfrac{\partial^2 \varepsilon_{\theta\theta}^{(m)}}{\partial \theta^2}\right|_{r=r_c^{(m)};\theta=\theta_0^{(m)}} < 0 \end{cases} \tag{3.17}$$

$$\varepsilon_{\theta\theta}^{(m)}(r_c^{(m)}, \theta_0^{(m)}) = \varepsilon_T^{(m)} = \sigma_T^{(m)} / E^{(m)} \tag{3.18}$$

Where, σ_T is the tensile fracture strength and $E^{(m)}$ is Young's modulus of the material *m*. The critical distance $r_c^{(m)}$ has the same expression as given in Eq. (3.12). The linear elastic relationship between the tangential strain and stress components is:

$$\varepsilon_{\theta\theta}^{(m)} = \frac{1}{E^{(m)}}(\sigma_{\theta\theta}^{(m)} - \nu^{(m)}\sigma_{rr}^{(m)}) \tag{3.19}$$

where $\nu^{(m)}$ is the Poisson's ratio of the material *m*. It is clear from Eq. (3.19) that the predictions based on MTSN criterion coincide with those based on MTS criterion when $\nu = 0$, mathematically.

3.3. Modified MTS (MMTS) criterion

A modified version of the MTS, named the MMTS [55], criterion is outlined here by considering the effect of T-stress in the bi-material crack stress field. First, the MTS criterion is reformulated and the role of T-stress on fracture initiation angle and fracture toughness is studied mathematically. Then, the MTS and MMTS are compared with each other in prediction of the fracture test data.

3.3.1. Formulations

By considering the effect of T-stress as well as the singular stress field given in Eq. (3.1), the conventional MTS criterion can be reformulated. The crack propagation angle in material *m* can be obtained from the following process by taking into account the effect of T-stress term:

$$\frac{\partial\sigma_{\theta\theta}^{(m)}}{\partial\theta} = 0 \rightarrow \frac{K_I}{\sqrt{2\pi r_c^{(m)}}}\frac{\partial f_{\theta\theta\_1}^{(m)}}{\partial\theta} + \frac{K_{II}}{\sqrt{2\pi r_c^{(m)}}}\frac{\partial f_{\theta\theta\_2}^{(m)}}{\partial\theta} + \frac{4T}{R^{(m)}}\sin(2\theta) = 0 \quad \rightarrow \quad \theta_0^{(m)} \tag{3.20}$$

$$\left(\frac{\partial^2\sigma_{\theta\theta}^{(m)}}{\partial\theta^2}\right)_{r_c^{(m)},\theta_0^{(m)}} < 0$$

In order to normalize the effects of T-stress and each fracture mode (K_I and K_{II}), the Eq. (3.20) can be rewritten as:

$$\frac{K_I}{K_{eff}}\frac{\partial f_{\theta\theta\_1}^{(m)}}{\partial\theta}+\frac{K_{II}}{K_{eff}}\frac{\partial f_{\theta\theta,\_2}^{(m)}}{\partial\theta}+\frac{4B\alpha^{(m)}}{R^{(m)}}\sin(2\theta)=0 \tag{3.21}$$

where, K_{eff} ,the effective stress intensity factor, and the parameters $\alpha^{(m)}$ and B are defined as:

$$K_{eff}=\sqrt{K_I^2+K_{II}^2} \tag{3.22}$$

$$B=\frac{T\sqrt{\pi a}}{K_{eff}} \tag{3.23}$$

$$\alpha^{(m)}=\sqrt{\frac{2r_c^{(m)}}{a}} \tag{3.24}$$

The parameter a is the crack length for edge cracks and semi-crack length for center cracks. Therefore, one can obtain the kinking angle by substituting the known parameters K_I, K_{II} and T-stress into the Eq. (3.21). The crack parameters K_I, K_{II} and T can be obtained by using different numerical methods [54, 85].

By taking into account the effect of T-stress, the Eq. (3.15) can also be changed to the following equation to obtain mixed mode fracture toughness;

$$\sqrt{2\pi r_c^{(m)}}\sigma_c^{(m)} = K_I f_{\theta\theta\_1}^{(m)} + K_{II} f_{\theta\theta\_2}^{(m)} = K_{IC}^{(m)} - 4\frac{T\sqrt{2\pi r^{(m)}}}{R^{(m)}}\sin^2(\theta_0^{(m)}) \tag{3.25}$$

The parameters $f_{\theta\theta\_1}^{(m)}$ and $f_{\theta\theta\_2}^{(m)}$ should be defined at $\theta = \theta_0^{(m)}$ calculated from Eq. (3.1) (see appendix A). The Eq. (3.26) could also be rewritten in terms of non-dimensional parameters as:

$$\sqrt{2\pi r_c^{(m)}}\sigma_c^{(m)} = K_I f_{\theta\theta\_1}^{(m)} + K_{II} f_{\theta\theta\_2}^{(m)} = K_{IC}^{(m)} - \frac{4}{R^{(m)}} B\alpha^{(m)} K_{eff}\sin^2(\theta_0^{(m)}) \tag{3.26}$$

Equations (3.21) and (3.26) represent MMTS criterion for prediction of the kinking angle and mixed mode interfacial fracture toughness, respectively.

3.3.2. The role of T-stress

Figure 3-2 shows the variation of the crack kinking angle with M^e, the mode mixity, and $B\alpha^{(1)}$ which represents T-stress effects. The mode mixity, M^e, represents the participation of each fracture mode, and is given as:

$$M^e = \frac{2}{\pi}\tan^{-1}\left(\frac{K_I}{K_{II}}\right) \tag{3.27}$$

Therefore, M^e = 1 for pure opening mode (mode I) and M^e = 0 for pure sliding mode (mode II). In order to show the effect of T-stress in Figure 3-2, it is typically assumed that crack propagates into material-1. The same trend would be obtained if material 2 were selected instead of material 1. The dimensionless parameter $B\alpha^{(m)}$ reflects the distribution of the T-stress in tangential stress field around the bi-material

crack tip. The range of $B\alpha^{(1)}$ is arbitrarily selected to be -0.6 < $B\alpha^{(1)}$ < 0.345. The material parameter $R^{(1)}$ and bi-material constant ε are selected to be 3 and -0.05, respectively. Since $\varepsilon = -0.05 < 0$, the material-1 is stiffer than material-2. The ranges of $B\alpha^{(1)}$, $R^{(1)}$, and ε are determined to be reasonable by referring the previously published experimental data [82, 89, 99, and 100].

The solid line in Figure 3-2 is the case of $B\alpha^{(1)} = 0$, i.e., there is no T-stress. This means that the solid line is identical to the kinking angle predicted by the traditional MTS criterion, while the dotted lines are the predictions considering the non-zero T-stress. The significant differences between the solid and dotted lines in Figure 3-2 demonstrate that neglecting the T-stress will result in significant errors in predicting the kinking angle. Furthermore, the kinking angle increases for positive values of T-stress (correspondingly the positive $B\alpha^{(1)}$), and conversely decreases for negative values of T-stress. It is also notable that the effect of T-stress on kinking angle decreases as the mode of loading approaches to pure opening mode (mode I, $M^e \rightarrow 1$), while the T-stress has considerable influences in pure sliding mode (mode II, $M^e \rightarrow 1$).

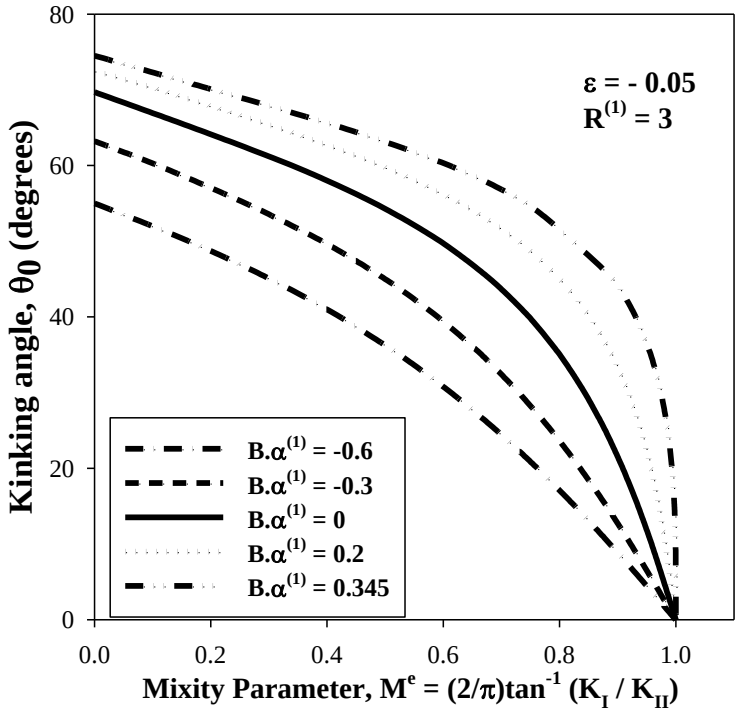

Figure 3-2. Effect of T-stress on kinking angle in material-1.

The effect of T-stress on mixed mode fracture toughness of a bi-material crack is also illustrated in Figure 3-3. Again, it is arbitrary assumed that crack propagates into material-1. The dimensionless parameter $B\alpha^{(1)}$ is also selected arbitrary within the range of $-0.4<B\alpha^{(1)}<0.12$ to cover an applicable range of experimental data. The material parameter $R^{(1)}$ and bi-material constant ε are selected as 5 and 0.05 respectively. For each value of $B\alpha^{(1)}$, fracture occurs in the area restricted between the coordinate axes and the corresponding curve.

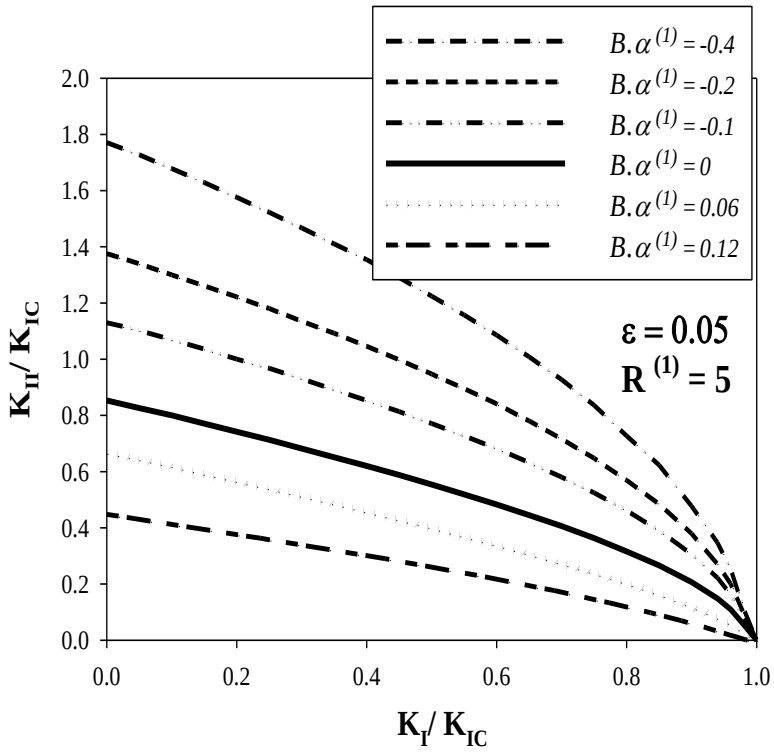

Figure 3-3. Effect of T-stress on mixed mode fracture toughness (it is assumed that the crack propagates into the material-1).

It can be seen that the fracture loci significantly vary with the magnitude and sign of T-stress (parameter $B\alpha^{(1)}$).Furthermore, it is seen that the predicted fracture toughness decreases for positive values of T-stress and conversely increase for negative values of T-stress. It is also notable to be mentioned when K_{II} approaches zero (pure mode I condition) the T-stress has no influence and when K_I approaches to zero there are always considerable errors for MTS predictions.

3.3.3. Calculation of the stress field parameters

In order to apply the MMTS criterion, the crack tip stress field parameters such as the stress intensity factors (K_I and K_{II}) and T-stress are needed to be calculated. For some geometries, at which the closed form solutions are not available, a finite element analysis is a useful tool to determine those parameters. In the presented study, the finite element over-deterministic (FEOD) method is used to find the stress intensity factors and T-stress for the three previous experiments that were simulated herein to validate the MMTS criterion. In this approach, the series solutions of displacement fields around the bi-material crack tip is fitted to a large number of nodal displacements obtained from the nodes surrounding the crack tip. Consequently, an over-determined set of linear equations is obtained, and the unknown coefficients in Eq. (3.1) are determined from the set of linear equations by employing the least square method. This method has also been successfully used to calculate the stress intensity factors and the coefficients of the higher order non-singular terms of the stress fields in both single- and bi-material sharp notch problems [54, 84]. The major advantages of the over-deterministic method are its simplicity, high accuracy, and the ability to calculate the fracture parameters and stress field including singular and non-singular terms simultaneously. More details about this approach can be found in Ayatollahi et al. [54]. An example of typical finite element meshes used for simulation of bi-material edge cracked specimen used by Bowen and Knauss [99] and its expanded view of the crack tip elements are shown in Figure 3-4.

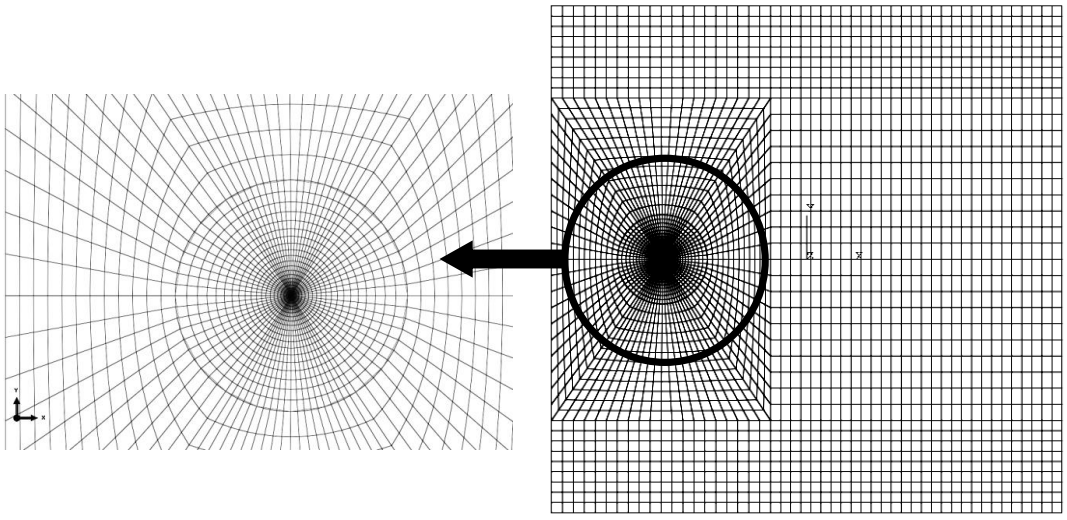

Figure 3-4. A typical finite element mesh used for simulation of bi-material edge cracked test specimen used by Bowen and Knauss [99].

In the following, the MTS and MMTS criteria are compared with each other in prediction of the fracture test data for different bonded structures. As a part of procedure, the stress intensity factors as well as the T-stress were calculated using FEM. For each specimen, a very fine mesh was used in the region near the crack tip, like shown in Fig 3-4 for edge cracked specimen, to reflect the high stress/strain gradient near the crack tip.

3.3.4. Validation of the MMTS criterion, and discussion

In order to validate the kinking angle and mixed mode fracture toughness predictions by MMTS criterion, three previously published set of data on bi-material

interface cracks are reexamined. The kinking angles and mixed mode fracture toughness are calculated using the MMTS criterion, and compared to the predictions by traditional criteria and experimental data.

3.3.4.1. Prediction of the kinking angles

- ***Case 1:*** Xie et al. [100]:

Xie et al. [100] studied the fracture behavior of a bi-material joint made of a carbon fiber reinforced composite and steel sheet and glued by epoxy using DCB specimens. The bi-material crack was embedded at the steel/ epoxy interface as illustrated in Figure 3-5.

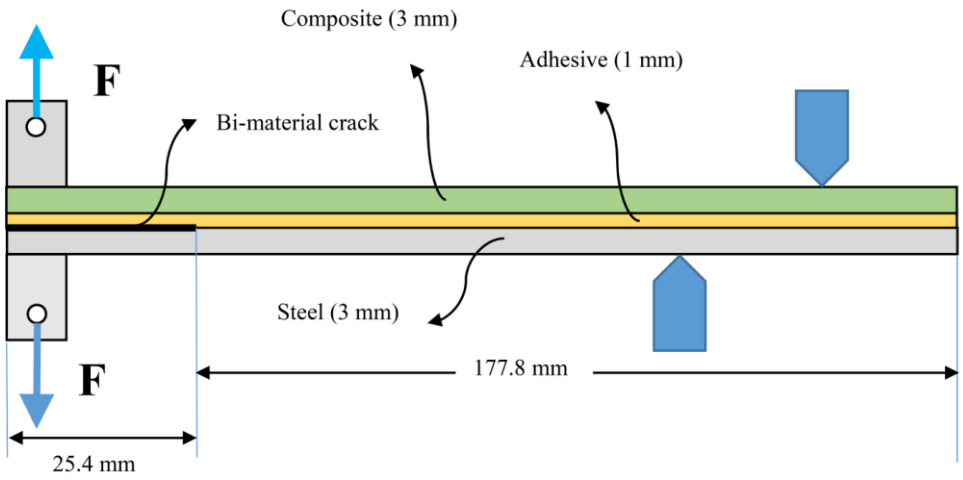

Figure 3-5. DCB specimen containing a bi-material crack at the epoxy/ steel interface tested by Xie et al. [100].

The elastic properties of each material are given in Table 3-1. They conducted a set of experiments on the DCB specimens under different loading conditions to study the fracture load and kinking angles of the interfacial crack. They observed that the interface cracks sometimes kink into the epoxy part with different kinking angles under different loading conditions. The dimensionless material parameters ε and $R^{(1)}$ are calculated to be 0.072 and 136.63, respectively, according to the material properties given in Table 3-1.

Table 3-1. The elastic properties of the materials in the DCB specimen [100].

Material	Young's modulus, E (MPa)	Poisson's ratio, ν
Composite	52,740	0.23
Adhesive (epoxy)	3,694.9	0.35
Steel	207,000	0.29

Figure 3-6 shows the variations of normalized tangential stress in epoxy part of the DCB specimen ($F_1 = F_2$) versus the angle θ at a circular path along the critical distance r_c = 0.05 mm from the crack tip. It is seen that a considerable discrepancy exists between the stress distributions reconstructed by MTS criterion and directly from FE results. On the other hand, the stress distribution obtained from MMTS criterion shows a very good coincidence with the FE analysis. As seen from Fig. 3-6, because of the positive values of T-stress, the MTS criterion provides lower values of tangential stress than the MMTS criterion. For this case, the kinking angles (corresponding to maximum tangential stress) obtained by FE analysis, MMTS, and MTS are 65.8^o, 65.1^o and 39.9^o, respectively.

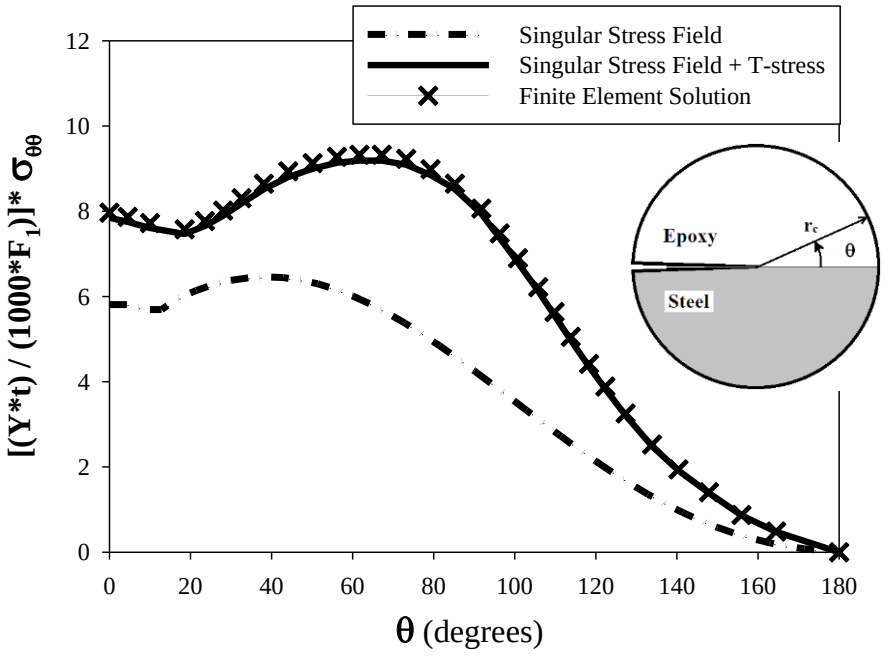

Figure 3-6. Variation of normalized tangential stress versus θ in epoxy part of the DCB specimen at a circular path of radius $r = r_c = 0.05$ mm from the crack tip.

Figure 3-7 shows the variations of the normalized tangential stress in epoxy part of the DCB specimen (F = F1 = F2) along the radial direction at the angle $\theta = \theta_0 = 65.8^o$, which corresponds to the angle of maximum tangential stress at the radial distance of 0.05 mm from crack tip. The normalized tangential stress is calculated by three different methods: a) closed form solution using only the singular stress terms of Eq. (3.1) – dash-dot line in Figure 3-7, b) closed form solution using the singular terms and the T-stress term of Eq. (3.1) – solid line, and c) finite element solution – cross symbol. With highly refined mesh around the crack tip (Figure 3-4), the finite element simulation is considered to be a solution including the effect of singular terms as well as higher order terms (including T-stress term). The gap between the solid and dash-dot lines in Figure

3-7 clearly shows that the T-stress significantly influences on the stress field near the critical distance of the bi-material crack tip. On the other hand, the solid line and cross symbol in Figure 3-7 are almost identical to each other in this range. This implies that the higher nonsingular stress terms have no effect on the stress distribution for radial distances less than 0.1 mm from crack tip. Indeed, the effect of the higher order terms would become more important when estimating far field stress. However, brittle cracks propagation is governed by the tangential stress at the critical distance from the crack tip (r = 0.05mm for epoxy), and hence, the effects of higher order terms can be neglected. It can be concluded that considering the first T-stress term and singular terms are sufficient for prediction of brittle crack propagation. It is also seen from Figure 3-7 that the T-stress smoothly varies around the critical distance, which shows that the T-stress calculation in this range is stable.

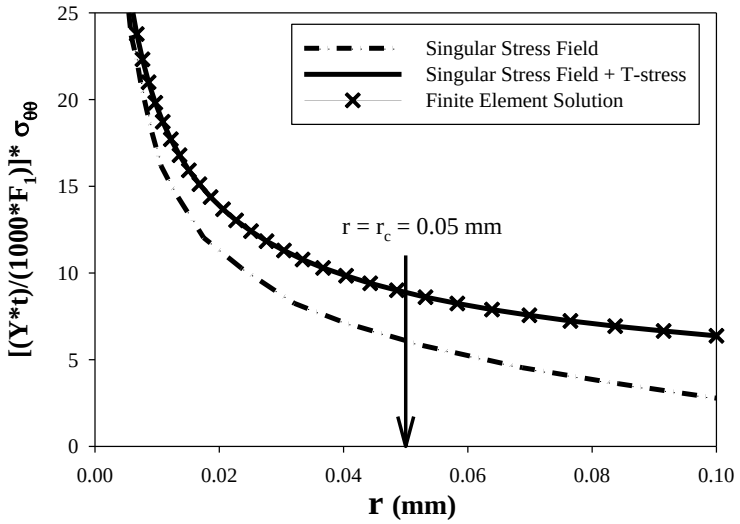

Figure 3-7. Variation of normalized tangential stress versus radial distance in epoxy part of the DCB specimen along $\theta = \theta_0 = 65.8^o$.

Table 3-2 shows the mode mixity parameter, M^e and the normalized T-stress parameter, $B\alpha^{(1)}$ for two samples of the DCB specimens obtained by the FE simulation and the experimental values given in Xie et al. [100]. The critical distance r_c for epoxy is assumed to be 0.05 mm according to the material properties given in Kawaguchi and Pearson [101]. For the given loading conditions, the bi-material cracks kink into the epoxy part (material-1).

Table 3-2. Values of M^e and $B\alpha^{(1)}$ from FE simulation compared to the experimental data [100].

F_2/F_1	M^e (FE simulation)	M^e (test results)	$B\alpha^{(1)}$
-1	0.564	0.572	0.327
0	0.312	0.332	0.341

The values of the kinking angles reported by Xie et al. [100] versus different M^e are illustrated in Figure 3-8. They used the maximum strain energy release rate criterion for prediction of the kinking angles. The kinking angles obtained by MTS and MMTS criteria are compared to the experimental and predicted data by Xie et al. [100] in Fig. 7. The values of T-stress are positive for all test cases, and as a result, the traditional MTS criterion predicted the kinking angles lower than the MMTS criterion. Figure 3-8 clearly shows that the MMTS criterion estimates the kinking angles more accurately than the traditional MTS and the maximum strain energy release rate criteria. Figure 3-8 also shows that the maximum energy release rate criterion does not provide a reasonable estimation of the kinking angles when compared to the MTS and MMTS criteria.

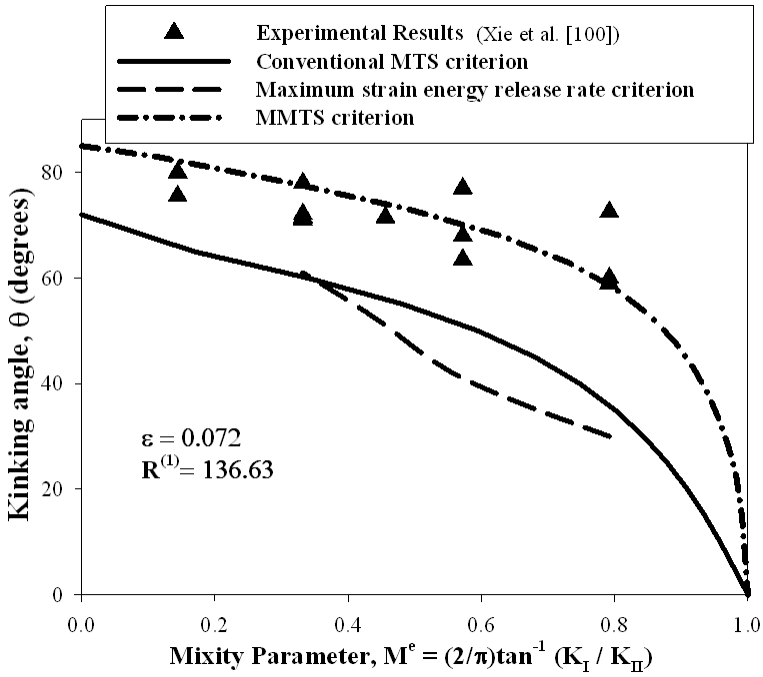

Figure 3-8. Variation of the kinking angle, θ_0, with mode mixity, M^e, for the DCB test specimen. The experimental data [100] are compared to the different fracture criteria.

- ***Case 2:*** Bowen and Knauss [99]

Bowen and Knauss [99] studied the fracture behavior of bi-material cracks existing at the interface of Solithane 55-45 and Solithane 45-55 experimentally. Solithane is a castable polyurethane elastomer used as an adhesive agent. The rigidity of Solithane can be controlled by changing the ratio of polymer and curative. In the bi-material block tested by Bowen and Knauss, Solithane 55-45 is a relatively hard material when compared to Solithane 45-55. The elastic material property of Solithane 55-45 and Solithane 45-55 are given in Table 3-3. They have conducted their tests using edge cracked specimens illustrated in Figure 3-9, at both 20 ^{o}C and 60 ^{o}C. Their experimental

results indicated that bi-material cracks may propagate through interface or may kink into one of the materials as the mode mixity varies [99].

Figure 3-10 compares the kinking angles obtained from the room temperature tests by Bowen and Knauss [99] with the kinking angle versus mode mixity curves calculated by the traditional MTS and suggested MMTS criteria. The material parameters ε and $R^{(1)}$ are calculated -0.039 and 3.38, respectively, and the critical distance for Solithane 55-45 is assumed to be r_c = 0.1 mm.

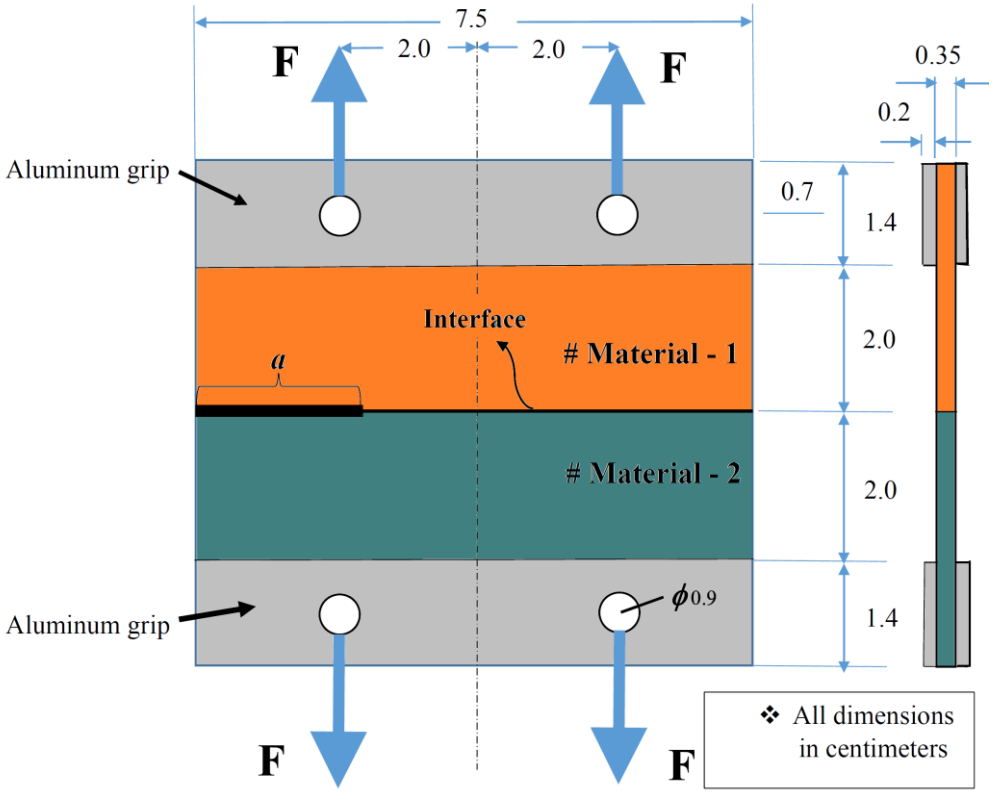

Figure 3-9. The bi-material edge cracked test specimen used by Bowen and Knauss [99].

Table 3-3. The elastic properties of the materials in the bi-material edge cracked test specimens [99].

Material	Young's modulus, E (MPa)	Poisson's ratio, ν
Material 1: Solithane 55-45	3.44	0.499
Material 2: Solithane 45-55	1.20	0.499

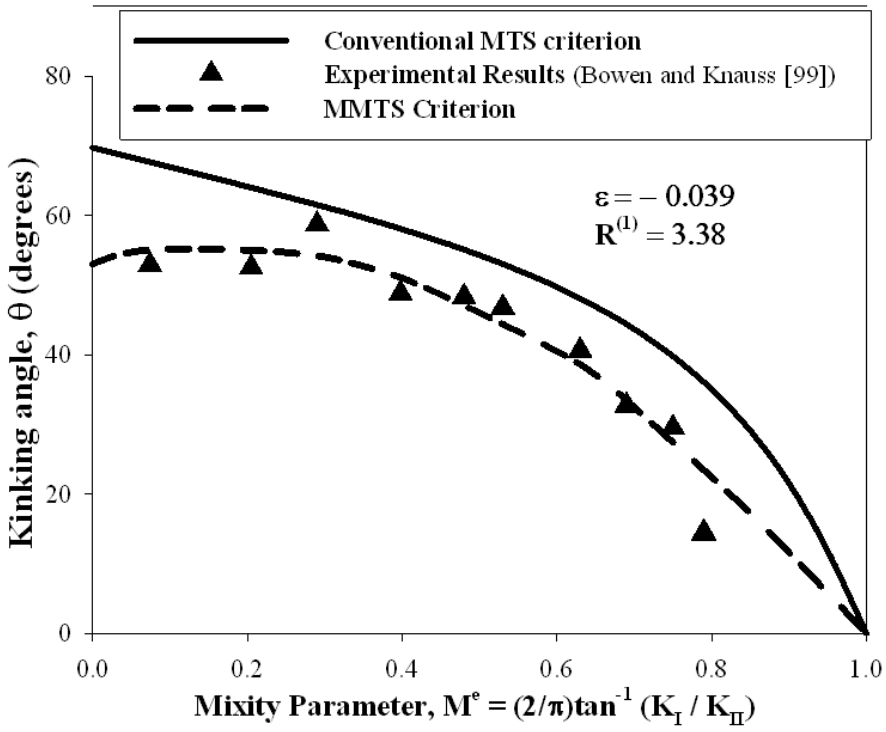

Figure 3-10. The variation of the kinking angle, θ_0, with mode mixity parameter M^e: the simulations by the MTS and MMTS criteria are compared to the test results by Bowen and Knauss [99].

The tests of Bowen and Knauss [99] were simulated using FE analysis in plane stress condition, and the T-stress and stress intensity factors were calculated. Table 3-4 shows two sample data of the mode mixity parameter, M^e and the normalized T-stress

parameter, $B\alpha^{(1)}$ of the DCB specimens obtained by the FE simulation and the experimental values given in Bowen and Knauss [99].

Table 3-4. Values of M^e and $B\alpha^{(1)}$ from FE simulation compared to the experimental data [99].

Specimen	M^e (FE simulation)	M^e (test results)	$B\alpha^{(1)}$
W11/8	0.672	0.694	- 0.311
W11/11	0.216	0.206	- 0.327

Figure 3-10 clearly shows that the MMTS criterion predicts the kinking angle with higher accuracy than the traditional MTS criterion. While the kinking angle measured experimentally by Xie et al. [100] are consistently higher than the prediction by the MTS criterion, the test data obtained from Bowen and Knauss [99] are always lower than the prediction by the MTS criterion. The suggested MMTS criterion provides a good explanation on this trend. As compared in Figure 3-2, the kinking angle increases when the T-stress is positive (tension), and decreases when the T-stress in negative (compression). As the T-stress in Figure 10-3 has a negative value, the experimentally measured kinking angles are lower than the prediction by the MTS criterion, but show good agreement with the prediction by the MMTS criterion.

- ***Case 3:*** Yuuki and Xu [82]

Yuuki and Xu [82] have carried out a set of mixed mode fracture tests using a circular disk specimen containing a crack at the aluminum-epoxy bi-material interface as shown in Figure 3-11. The disk specimen was subjected to different loading angles, ϕ, to

generate various mixed mode loadings ranging from mode I to mode II. The elastic properties of the aluminum and epoxy are given in Table 5.

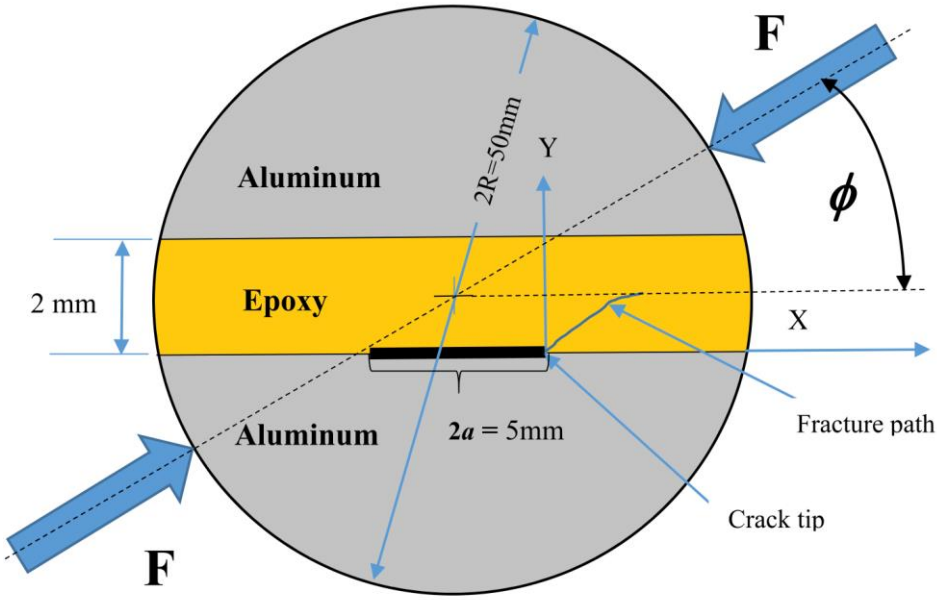

Figure 3-11. The circular disk specimen with a bi-material crack at aluminum/ epoxy interface used by Yuuki and Xu [82]. (The disk thickness, h = 5mm).

Table 3-5. The elastic properties of the materials in circular disk specimen [82].

Material	Young's modulus, E (MPa)	Poisson's ratio, ν
Aluminum	72,520	0.37
Epoxy	2,900	0.38

The variation of the kinking angle with M^e (loading angle, ϕ =13°, 15°, and 17°) measured by Yuuki and Xu [82] are illustrated in Figure 3-12. The material parameters ε

and $R^{(1)}$ are calculated to be 0.057 and 64.64, respectively, and the critical distance, r_c = 0.05 mm is assumed for epoxy part (material-1) [101].

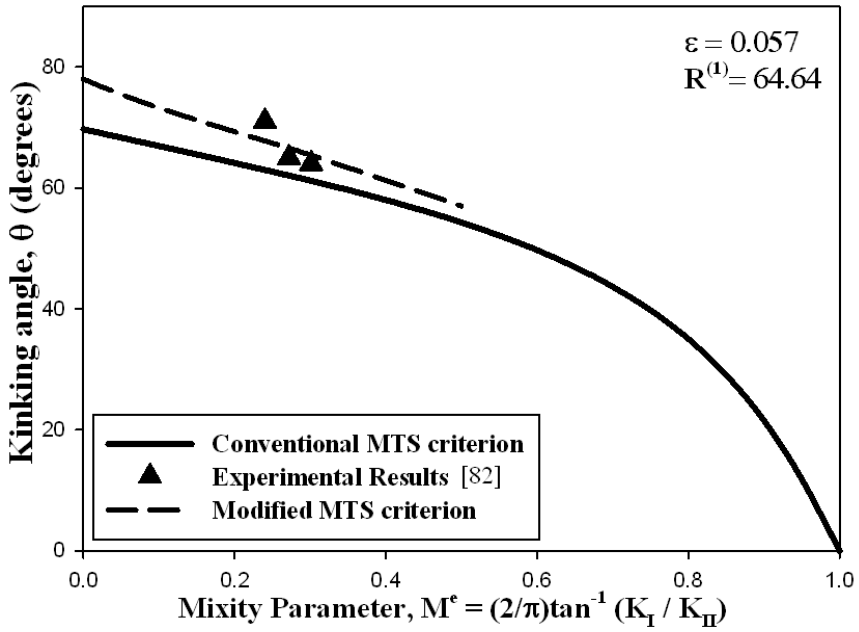

Figure 3-12. Variation of the kinking angle, θ_0, with mode mixity, M^e, for the circular disk specimens. The experimental data [82] are compared to the predictions by the MTS and MMTS criteria.

Two sample values of mode mixity parameter and $B\alpha^{(1)}$ obtained from the FE simulation and the test data [82] are given in Table 3-6.

Table 3-6. Values of M^e and $B\alpha^{(1)}$ from FE simulation compared to the experimental data [82].

ϕ (degrees)	M^e (FE simulation)	M^e (test results)	$B\alpha^{(1)}$
13	0.334	0.328	0.0482
17	0.264	0.272	0.0515

The numerical simulation indicates that the T-stress values are positive for $0.1 < M^e < 0.5$ as shown in Figure 3-12. Therefore, the traditional MTS criterion provides lower predictions than MMTS criterion for kinking angles. Again, the MMTS criterion predicts the experimental results better than the traditional MTS criterion.

As shown in Figures 3-8, 3-10, and 3-12, the applications of the MMTS criterion to three previously published set of data show that the kinking angle of the bi-material interface crack is significantly influenced by the T-stress, and by considering the role of the T-stress, the MMTS criterion is capable of more accurate estimation of the kinking angle than the traditional MTS criterion.

3.3.4.2. Prediction of the fracture toughness

In addition to the kinking angles, Yuuki and Xu [82] have obtained the interfacial mixed mode fracture toughness of Al/ epoxy bonded joints using the same specimen shown in Figure 3-11**.** The predicted fracture loci using both MTS and MMTS criteria are illustrated in Figure 3-13 in comparison with the experimental data. As the crack kinks into the epoxy part, the material property of epoxy (material 1) is used to plot the MMTS curve (K_{IC} = 0.78 MPa.m^0.5 and r_c = 0.05mm) [82]. The MMTS prediction is plotted in different loading conditions. The numerical simulation indicate that the T-stress is positive in all mixed mode conditions, as shown in Table 3-6, for $\phi = 13^o$, 15^o and 17^o. As a result, the estimated mixed mode fracture toughness data by MTS criterion are greater than those of estimated by MMTS criterion. It also could be seen that the

MMTS criterion provides more accurate prediction for experimental results than conventional MTS criterion.

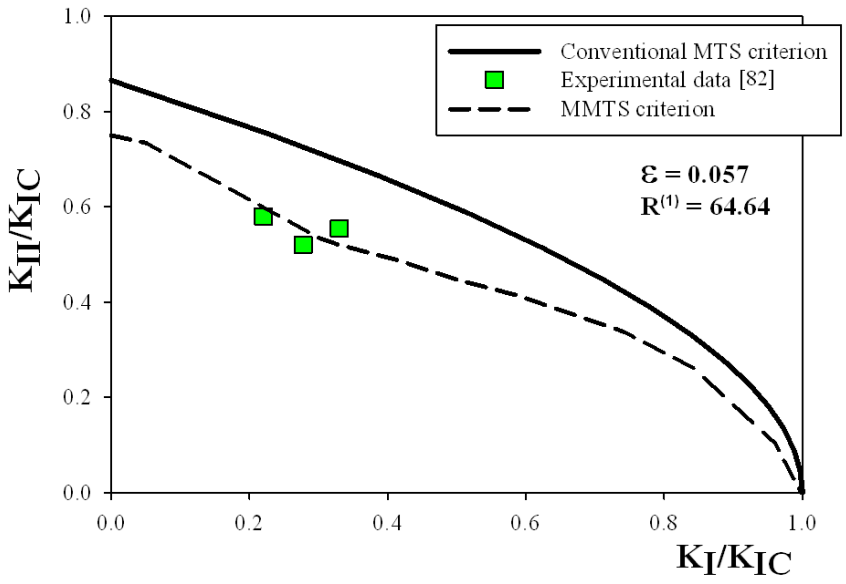

Figure 3-13. Experimental data for mixed mode fracture toughness in comparison with the MTS and MMTS predictions.

3.4. Fracture criteria for weak interfaces

As discussed above, for an interface crack problem, we have two types of fracture criteria which are developed for: “weak” interfaces and “strong” interfaces. Fracture criteria for strong interfaces were discussed above. The interfacial fracture criteria for weak interfaces will be discussed below.

The interfacial fracture criteria for weak interfaces is still in need of development. However, the traditional concepts which are used for crack propagation in a homogeneous media can be applied to weak interfaces. For weak interfaces, mixed

mode fracture energy results can be presented in several ways, including as plots of total fracture energy, as a function of mode mixity, and as fracture envelopes in which either stress intensity factors (K) or strain energy release rates (G) for mode I and mode II loading are plotted on the abscissa and ordinate axes, respectively. Functional forms have been used to express the fracture energy criteria such as [102, 103]:

$$\left[\frac{(G_I)_C}{G_{IC}}\right]^p + \left[\frac{(G_{II})_C}{G_{IIC}}\right]^q = 1 \tag{3.28}$$

where $(G_I)_C$ and $(G_{II})_C$ are the mode I and mode II components of the strain energy release rate at fracture, G_{IC} and G_{IIC} are the critical fracture energies for pure modes, and p and q are exponents. Since $K_I = \sqrt{E^*.G_I}$ and $K_{II} = \sqrt{E^*.G_{II}}$, where $E^* = E$ for plane stress conditions and $E^* = E/(1-\nu^2)$ for plane strain conditions, the related expression for the stress intensity factors can be written as:

$$\left[\frac{(K_I)_C}{K_{IC}}\right]^{2p} + \left[\frac{(K_{II})_C}{K_{IIC}}\right]^{2q} = 1 \tag{3.29}$$

The exponents may be chosen to form the best fit of experimental data or may be prescribed based on some assumed relationship. For example, if the critical fracture energy is assumed to depend only on the total fracture energy ($G_T = G_I + G_{II}$) and not the mode mixity, $p = q = 1$, and $G_{IC} = G_{IIC}$. This results in squaring the stress intensity terms in Eq. (3.29), which being proportional to stress, provides a fracture criterion that is similar to the von Mises yield criterion. If p and q are both greater than, or equal to unity, the resulting criterion implies that the mixed mode fracture energies will be larger than the minimum of G_{IC} and G_{IIC}. In that case, the use of the minimum pure mode

fracture energy (Min (G_{IC}, G_{IIC})) would be conservative for design purposes [60]. On the other hand, if p is less than unity, mixed mode fracture energies could be smaller than G_{IC}, which is often the smallest pure mode fracture energy.

Alternate forms for fracture envelope criterion have also been proposed [104, 105], including [106]:

$$\left(\frac{G_I}{G_{IC}}-1\right)\left(\frac{G_{II}}{G_{IIC}}-1\right)-I_i\left(\frac{G_I}{G_{IC}}\right)\left(\frac{G_{II}}{G_{IIC}}\right)=0 \tag{3.30}$$

This relationship involves a single interaction factor, I_i, which is zero if there is no interaction ($G_I / G_{IC} = 1$ or $G_{II} / G_{IIC} = 1$, corresponding to $p \to \infty$ and $q \to \infty$) and unity if there is a simple addition ($G_I / G_{IC} + G_{II} / G_{IIC} = 1$, corresponding to $p = q = 1$) such that the total energy release rate controls the fracture. However, in many cases the interaction reduces the fracture energy, correspond with $I_i < 1$.

In real bonds, criterion such as given above may be used to model fracture envelopes, but because they are phenomenological in nature, they typically cannot accurately represent results when changes in locus or type of fracture process occur. Mechanistically, shear stresses tend to drive cracks away from a path that is parallel to the bond planes, potentially steering cracks into regions of the material system where the energy dissipation associated with crack advance can change significantly. In some cases, the direction of the shear stress state in relation to the growing crack can steer the crack towards interfaces that are ‘weaker’, allowing the crack to propagate with less energy dissipation. In other cases, however, the crack can actually be steered to regions where greater energy dissipation occurs because of an improved interface or other

reasons. To understand the role that shear stress plays in determining the mode of failure, note that in homogeneous isotropic materials, cracks tend to propagate perpendicular to the direction of maximum tensile stress. In an adhesive joint subjected to a shear state, cracks within the adhesive layer have a tendency to grow toward one interface. Shear-dominated loading often results in interfacial failures or failures with less adhesive left on an interface [107, 108], although more complex hackle pattern failures have also been reported [109]. Also, some adhesive fracture envelopes are relatively smooth, permitting reasonable fits with phenomenological criteria, such as cited above.

3.5. Modifications for viscoelastic media

The elastic stress field around an interface crack can be expressed as Eq. (3.31), where the coefficients of the stress field are time-dependent:

$$\sigma_{rr}^{(m)}(t)=\frac{K_I(t)}{\sqrt{2\pi r}}\,f_{rr\_1}^{(m)}(\ln\left[\frac{r}{L}\right],\varepsilon,\theta)+\frac{K_{II}(t)}{\sqrt{2\pi r}}\,f_{rr\_2}^{(m)}(\ln\left[\frac{r}{L}\right],\varepsilon,\theta)+4\frac{T(t)}{R^{(m)}}\cos^2(\theta)+H.O.T(t)$$

$$\sigma_{\theta\theta}^{(m)}(t)=\frac{K_I(t)}{\sqrt{2\pi r}}\,f_{\theta\theta\_1}^{(m)}(\ln\left[\frac{r}{L}\right],\varepsilon,\theta)+\frac{K_{II}(t)}{\sqrt{2\pi r}}\,f_{\theta\theta\_2}^{(m)}(\ln\left[\frac{r}{L}\right],\varepsilon,\theta)+4\frac{T(t)}{R^{(m)}}\sin^2(\theta)+H.O.T(t) \tag{3.31}$$

$$\tau_{r\theta}^{(m)}(t)=\frac{K_I(t)}{\sqrt{2\pi r}}\,f_{r\theta\_1}^{(m)}(\ln\left[\frac{r}{L}\right],\varepsilon,\theta)+\frac{K_{II}(t)}{\sqrt{2\pi r}}\,f_{r\theta\_2}^{(m)}(\ln\left[\frac{r}{L}\right],\varepsilon,\theta)-4\frac{T(t)}{R^{(m)}}\sin(\theta)\cos(\theta)+H.O.T(t)$$

In a linear viscoelastic material, the stress and strain components satisfy the following constitutive equation:

$$\varepsilon_{ij}(t)=\int_{-\infty}^{t}J_1(t-\tau)\frac{\partial\sigma_{ij}(\tau)}{\partial\tau}d\tau+\frac{1}{3}\delta_{ij}\int_{-\infty}^{t}[J_2(t-\tau)-J_1(t-\tau)]\frac{\partial\sigma_{kk}(\tau)}{\partial\tau}d\tau, \tag{3.32}$$

Where $J_1(t)$ and $J_2(t)$ denote the creep compliance of shear and dilation, respectively. In terms of Laplace transforms with respect to time, the above equation can be expressed as:

$$\bar{\varepsilon}_{ij}(s) = s\bar{J}_1(s)\bar{\sigma}_{ij}(s) + \frac{1}{3}\delta_{ij}s[\bar{J}_2(s) - \bar{J}_1(s)]\bar{\sigma}_{kk}(s). \tag{3.33}$$

The Laplace transforms of the equilibrium equation of stress and compatibility equation are expressed as

$$\frac{\partial \bar{\sigma}_{xx}(s)}{\partial x} + \frac{\partial \bar{\sigma}_{xy}(s)}{\partial y} = 0, \tag{3.34}$$
$$\frac{\partial \bar{\sigma}_{xy}(s)}{\partial x} + \frac{\partial \bar{\sigma}_{yy}(s)}{\partial y} = 0,$$

$$2\frac{\partial \bar{\varepsilon}_{xy}(s)}{\partial x \partial y} = \frac{\partial^2 \bar{\varepsilon}_{yy}(s)}{\partial x^2} + \frac{\partial^2 \bar{\varepsilon}_{xx}(s)}{\partial y^2} \tag{3.35}$$

The viscoelastic coefficients can be expressed in Laplace transforms by the following relations:

$$\bar{J}_1(s) = [1 + s\bar{\nu}(s)]\bar{D}_c(s), \tag{3.36}$$
$$\bar{J}_2(s) - \bar{J}_1(s) = -3s\bar{\nu}(s)\bar{D}_c(s)$$

Where $\bar{D}_c$ and $\bar{\nu}$ are the Laplace transforms of the uniaxial creep compliance $D_c(t)$ and Poisson's ratio $\nu(t)$. Equations 3.33 – 3.36 provide the compatibility of stress as follows:

$$s\bar{D}_c(s)\left(\frac{\partial^2}{\partial x^2} + \frac{\partial^2}{\partial y^2}\right)\left(\bar{\sigma}_{xx}(s) + \bar{\sigma}_{yy}(s)\right) = 0. \tag{3.37}$$

Therefore, the inverse Laplace transform of Eq. (3.37) is expressed as;

$$\int_{-\infty}^{t} D_c(t-\tau)\frac{\partial}{\partial\tau}\left(\frac{\partial^2}{\partial x^2}+\frac{\partial^2}{\partial y^2}\right)\left(\sigma_{xx}(\tau)+\sigma_{yy}(\tau)\right)d\tau = 0 \tag{3.38}$$

We can prescribe the stresses through the separated form

$$\sigma_{ij}(x,y,t) = \sigma_{ij}^{0}(x,y)F(t), \tag{3.39}$$

and introduce the stress function as well as elastic analysis,

$$\frac{\partial^2\phi}{\partial x^2} = \sigma_{yy}^{0}, \qquad \frac{\partial^2\phi}{\partial y^2} = \sigma_{xx}^{0}, \qquad -\frac{\partial^2\phi}{\partial x\partial y} = \sigma_{xy}^{0} \tag{3.40}$$

By substituting Eq. (3.39) and (3.40) into Eq. (3.38), we can deduce that the stress function ϕ must satisfy the following equation

$$\frac{\partial F(t)}{\partial t}\left(\frac{\partial^2}{\partial x^2}+\frac{\partial^2}{\partial y^2}\right)^2\phi = 0. \tag{3.41}$$

Eq. (3.41) states that the spatial distribution of stress field in viscoelastic materials determined by the stress function is the exactly the same as that in elastic materials.

3.6. Summary and conclusions

Different fracture criteria for strong and weak interfaces were studied in this section. For strong interfaces, different energy-based, stress-based, and strain based criteria were reviewed and discussed. The MMTS criterion was developed as a modified version of the conventional MTS criterion considering the role of T-stress. The effect of T-stress on mixed mode fracture toughness of bi-material cracks was studied analytically. The significant effect of T-stress was shown on the estimation of the

kinking angle and mixed mode fracture toughness. Then, the MMTS criterion was validated using the test results reported in the literature for different bonded materials and specimens. It was shown that the MMTS criterion provides more accurate prediction of experimental data than conventional MTS criterion for estimation of the mixed mode fracture toughness and kinking angles of bi-material cracks. It also should be noted the number of experimental dada reported in the literature for mixed mode fracture toughness of strong interfaces were limited. Although, no recommendation is currently given in standards for the faced problem, the results of this paper could be useful in standardization of the bi-material fracture tests. Criteria for interfacial crack propagation through weak bonds were also discussed. Finally, some required modifications were given for extension of the discussed ideas to a linear viscoelastic media.

4. A NEW TEST SPECIMEN FOR EVALUATION OF THE INTERFACIAL BOND STRENGTH

4.1. Introduction

Bi-material joints can be seen as a part of many industrial and engineering structures with application in civil engineering, electronic devices, automobiles and aircrafts [63, 64, 67, 68, 110, and 111]. At the interface of bi-material components, cracks may form during the service life of the structures. The interface cracks are often under mixed mode loading, because of the asymmetry in material properties at the interface, and they may propagate through the interface, or may kink into one of the materials in strong interfaces [64, 68 and 111].

Several theoretical and experimental methods have been suggested by researchers for exploring mixed mode brittle fracture. Since experimental fracture studies on real components are often expensive and difficult, researchers prefer to conduct their experiments using laboratory specimens. However, appropriate fracture criteria allow correlation of the experimental results obtained from laboratory specimens to fracturing in-field structures under their complex service loading conditions. Fracture criteria are needed to understand mechanism of crack initiation and propagation in structural materials under complex loads. In order to validate a fracture criterion, researchers have to conduct a series of experiments on appropriate test materials by using suitable test specimens. For mixed mode fracture experiments, a suitable test configuration should have simple geometry and loading conditions, an inexpensive

preparation procedure, convenient set up and the capability of addressing various combinations of mode I and mode II fracture. Some of the test configurations proposed in the literature for investigating mixed mode I/II fracture are briefly described here.

Erdogan and Sih [83], Williams and Ewing [112] and Theocaris [113] used a rectangular plate containing an inclined center crack subjected to a uniform far tension field in their mixed mode fracture studies. Others employed asymmetrically loaded three or four-point bend specimens to investigate mixed mode brittle fracture [114– 121]. Disc type specimens including the centrally cracked Brazilian disk (BD) specimen and the semi-circular bend (SCB) specimen have been frequently employed for determining the mixed mode fracture resistance of various engineering materials such as rocks and polymers [122–130]. The compact tension-shear specimen [131–133] is another configuration used for mixed mode fracture experiments. Ewing et al. [134] made use of the inclined edge-crack plates subjected to far field tension and bending to study mixed mode fracture in polymeric materials. More recently Ayatollahi and Aliha [135] proposed a diagonally loaded square plate containing an inclined center crack for investigating mixed mode fracture behavior. In the above-mentioned studies, brittle fracture experiments have been conducted either on PMMA or other brittle or quasi-brittle materials like ceramics and rocks. However, some of these specimens have certain shortcomings. For example, some of the mixed mode test configurations are able to provide only limited mode mixities or require complicated loading fixtures.

For a bi-material specimen, the above mentioned problems becomes more important since the mode mixity is influenced by not only the geometry of the specimen,

but also the material properties of each bonded materials. That means there is a need to choose a suitable fracture test specimen by considering both specimen geometry and the material property. Some of the test configurations proposed in literature for investigating mixed mode I/II fracture of bonded structures are briefly described below. Charalambides et al. [136] suggested a new four point bend specimen for measuring the fracture resistance of bi-material interfaces. Utilizing finite element analysis, they characterized their suggested specimen and calculated stress intensity factors at different specimen geometries and elastic properties. They demonstrated the utility of their specimen by conducting experiments on Aluminum/PMMA bonded joints. However, their suggested specimen were not able to cover all combinations from pure mode I to pure mode II. Evans et al. [137] studied the interface crack propagation in different bonded joints using different bi-material fracture test specimens such as: the Sandwich test specimen, the Peel test specimen, the De-cohesion test specimen, and the Composite cylinder test specimen. They demonstrated that the choice of test specimen governs the tendency of cracks to either remain at interfaces or deviate from. However, none of the mentioned specimens were able to cover all mixed mode conditions.

The specimens of circular or semi-circular shape (SCB) are very suitable for fracture testing on rock or asphalt materials because they can be easily cut from cylindrical cores from a pavement structures or cylindrical molds which are traditionally prepared from such materials. However, the SCB specimen has not been used so far for bi-material testing to evaluate bond strength. Also, it is unclear whether the SCB specimen is able to address all mixed mode conditions from pure mode I to pure mode II

for a given material type. However, as elaborated in the next section, a bi-material SCB test specimen is proposed for fracture test of asphalt concrete/ Portland cement concrete bonded joints which can be seen in pavement structure. In the subsequent sections, the suggested specimen is described where its capabilities and advantages are investigated by means of finite element analysis and through some fracture testing conducted using asphalt concrete/ Portland cement concrete bonded specimens.

4.2. New test configuration

The classical semi-circular bend (SCB) specimen has been used by several researchers in the past for investigating mixed mode fracture in brittle materials, e.g. [126–130]. The SCB specimen that contains an angled crack is subjected to three-point bending. Figure 4-1 shows the geometry and loading conditions for the improved SCB test specimen, called the Bi-material SCB (BSCB) specimen, for study of the mixed mode propagation of a crack at the interface of two dissimilar materials. In this test configuration, a semi-circular specimen of radius R that contains an edge interface crack of length a with inclination angle of δ, is loaded asymmetrically by a three-point bend fixture. As illustrated in Figure 4-1, the crack exists at the interface of asphalt concrete and the Portland cement concrete. While the specimen is easily manufactured, it does not need complicated loading fixtures for use in conventional testing machines. The state of mode mixity in the BSCB specimen can be easily altered by changing the locations of two bottom supports (S1 and S2) and the crack inclination angle (δ).The mode I and mode II contributions can be controlled simply by choosing appropriate values for S1,

S2, and δ. Hence different mode mixities can be obtained in the proposed specimen. The specimen has been frequently used in the past but only for the simple case of homogeneous material (single material) in order to obtain pure mode I fracture toughness for several engineering materials including, rocks, concrete, asphalt, polymers, etc. [128–130, 138–140].

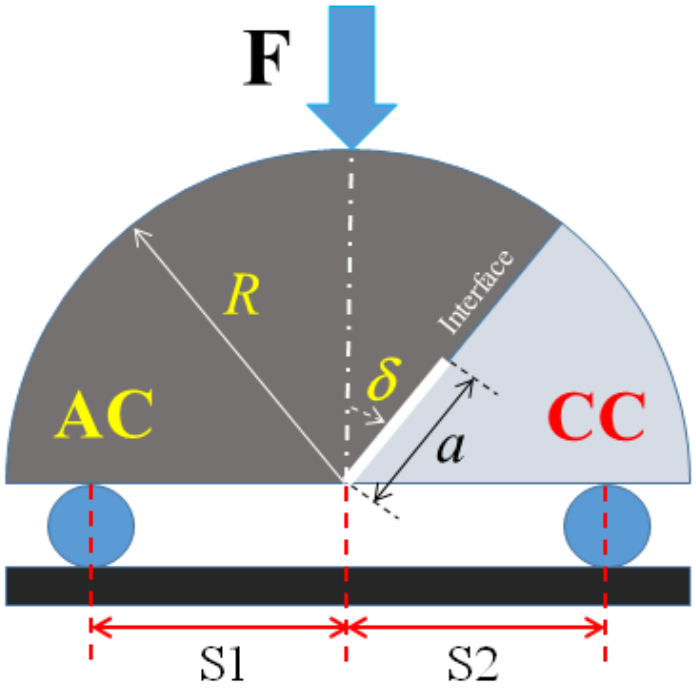

Figure 4-1. Scheme of the CSCB specimen made of asphalt concrete and Portland cement concrete.

In order to study mixed mode interfacial fracture in brittle materials using this configuration, it is necessary to define the state of mode mixity by calculating the mode I and mode II stress intensity factors (K_I and K_{II}) for different loading positions and crack

lengths. The finite element method was employed in this research to determine K_I and K_{II} in the BSCB specimen. More calculation details will be given in the next section.

4.3. Numerical analysis

Stress intensity factors are required to be characterized for any fracture test specimen in order to evaluate stress field around the crack. The stress intensity factors K_I and K_{II} for the BSCB specimen are functions of the crack length (a), crack inclination angle (δ), the locations of loading supports defined by S1 and S2, and elastic properties of both bonded materials. For a given elastic material property, the stress intensity factors can be expressed as the following normalized form:

$$K_I = \frac{F}{2Rt}(\sqrt{\pi a})Y_I(\delta, \frac{a}{R}, \frac{S1}{R}, \frac{S2}{R}) \tag{4.1}$$

$$K_{II} = \frac{F}{2Rt}(\sqrt{\pi a})Y_{II}(\delta, \frac{a}{R}, \frac{S1}{R}, \frac{S2}{R}) \tag{4.2}$$

where t is the specimen thickness and Y_I and Y_{II} are the geometry factors corresponding to mode I and mode II, respectively. For calculating Y_I and Y_{II}, different finite element models of the BSCB specimen were analyzed using the finite element code ABAQUS. Figure 4-2 shows a typical mesh pattern generated for simulating the ASCB specimen. In the models, the following geometry and loading conditions were considered: R = 76.2mm, t=25 mm, a=38.1mm, F = 1000N and different values for crack inclination angles (δ), S1, and S2. Since the original goal of the current research is to evaluate bond strength between asphalt concrete and Portland cement concrete, in this research, these two materials have been used for finite element simulations. Same procedure can be

done for any combination of the materials. The elastic properties used for the finite element modeling of the asphalt concrete and Portland cement concrete are: E_{asph}=4.9 *GPa*, ν=0.35, E_{conc}=40.7*GPa*, ν=0.2. The specimen preparation and material properties is described in the forthcoming sections of this section.

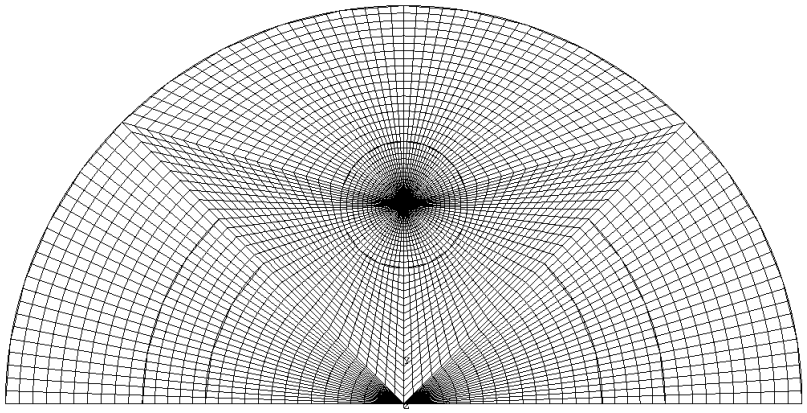

Figure 4-2. A typical finite element mesh pattern used for simulating BSCB specimen with δ=0.

The singular elements were considered in the first ring of elements surrounding the crack tip for producing the square root singularity of stress/strain field. A J-integral based method built in ABAQUS was used for obtaining the stress intensity factors directly from software. Table 4-1 lists the values of Y_I and Y_{II} associated with pure mode I, pure mode II and three mixed mode conditions. It is seen that the proposed specimen is able to cover different mixed mode conditions from pure mode I (M^e=1) to pure mode II (M^e=0). Fig.5 shows the von Mises stress contour plot for two different mode mixities: pure mode I (K_{II} = 0) and pure mode II (K_I = 0). In pure mode I, the stress contour is symmetric relative to the crack plane. However, because of the material mismatch, the

stress contour is discontinuous at the interface. For pure mode II, the contour plot is asymmetric with respect to the crack plane showing the significant effect of shear stress. The proposed specimen is utilized in the next section to evaluate mixed mode bond strength of asphalt concrete/ Portland cement concrete (AC/ PCC) bonded joints at different temperatures.

Table 4-1. Finite element simulation results of BSCB at different mixed mode conditions.

a (mm)	*δ (deg)*	*S1 (mm)*	*S2 (mm)*	Y_I	Y_{II}	M^e
38.1	0	50	38	0.323	0.000	1.00 (pure I)
38.1	0	30	20	0.154	0.062	0.758
38.1	0	60	15	0.149	0.120	0.569
38.1	45	50	50	0.105	0.154	0.382
38.1	58	50	50	0	0.1	0 (pure II)

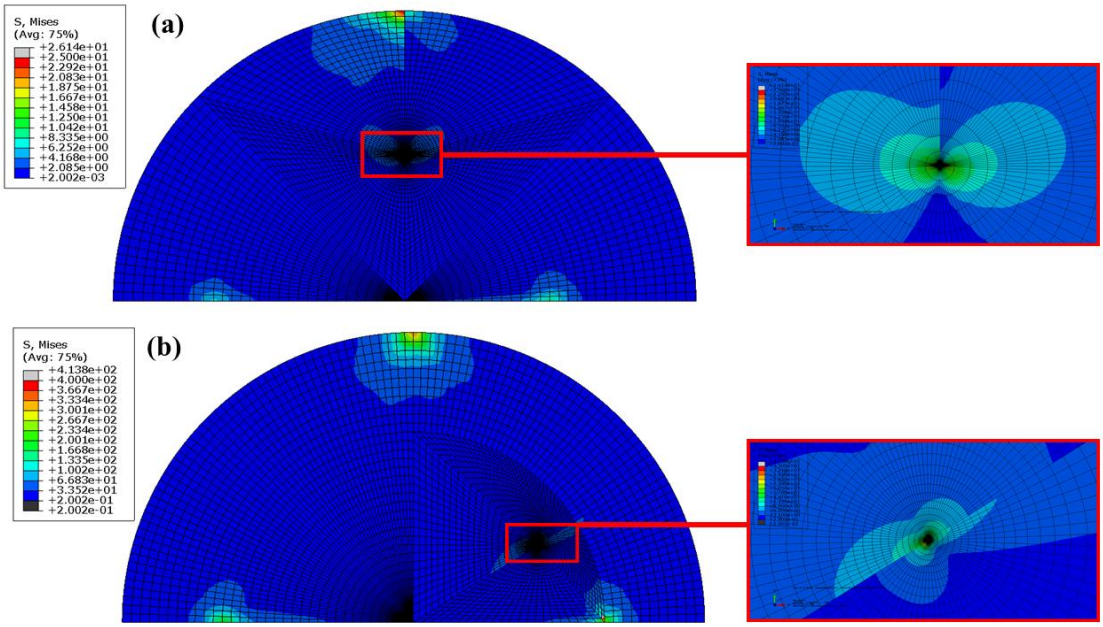

Figure 4-3. Plots of von Mises stress contours in front of the interface crack tip at (a) pure mode I, (b) pure mode II conditions.

4.4. Evaluation of bond strength of AC/ PCC interface

In order to investigate the practical applicability of the BSCB specimen, a series of mixed mode fracture tests were conducted on AC/ PCC bonded joints. A total number of 50 BSCB specimens were manufactured at different thicknesses ranging from 30mm to 35mm. In the following, the material properties of the AC and PCC, specimen preparation process, and fracture test results are describes and finally, the test data were evaluated using a power-law fracture criterion discussed in the previous section of this dissertation (section 3) for weak interfaces.

4.4.1. Material properties of AC and PCC

The materials used to manufacture BSCB specimens made of AC and PCC are given as follows. For AC, PG 64–22 asphalt binder were used and the asphalt binder content was 4.4% of the total weight. Course aggregates and sands were used to be mixed with asphalt binder. The collected materials were dried in an oven, sampled and used for sieve analysis to obtain the percentage of aggregates according to the standard size ranges. The aggregate gradation chart for this mix is given in Table 4-2.

For PCC, the following combination of raw materials were used as listed in Table 4-3. Coarse and fine aggregate and cement were all mixed prior to adding water. Once the cement-aggregate mixture was uniform, a combination of water and admixture was then added. When the batch had a uniform consistency the specimens were cast.

4.4.2. Specimen preparation

Figure 4-4 depicts the procedure for manufacturing the BSCB specimens. As shown, the asphalt concrete portions were made first, and then split before being placed in cylindrical molds such that concrete was placed into the remaining volume to create the composite cylinders. The standard cylindrical mold - 6*in* diameter (152.4*mm*× 304.8*mm*) was used to make the composite cylinders. The 6*in*×6*in* asphalt concrete cylindrical samples were made using a gyratory compactor (see [141] for details on the compaction process).

Table 4-2. Aggregate gradation for making AC part of BSCB specimens.

Sieve size (mm)	Standard sieve size	Percent passing
19	¾ in	100
12.5	½ in	95
9.5	3/8 in	82
4.75	No.4	55
2.36	No.8	34
1.18	No.16	22
0.6	No.30	16
0.3	No.50	12
0.15	No.100	6
0.75	No.200	5
0		0

Table 4-3. Mix design for PCC part of BSCB specimens.

Materials	Weight (lbs) per cubic yard of concrete
Cement Type I/II	423
Fly Ash Class F	141
Coarse Agg. #57 Crushed LS	1850
Fine Agg. Concrete Sand	1184
Water	242.6

Table 4-3. continue	
Materials	Weight per cubic yard of concrete
Water Reducer Type A/D	23 oz
Air Entraining Agent	1.7 oz

The cylindrical samples were cured for one day and cured for 7 days at moisture room and one year at room temperature (25^{o}C). The composite cylinders were then cut into several pieces (perpendicular to the cylinder's axis). Each piece was cut diagonally at the angle of 90^{o}-δ from the AC/PCC interface (δ is the crack inclination angle, shown in Figure 4-1) to make the final composite specimen. The crack length ratio a/R=0.5 was selected to make the test samples. For creating the cracks, first a cutting machine is used to generate a notch through the interface with the initial depth of slightly less than 38.1*mm*. Then, a sharp pre-crack was introduced by a thin cutter to make the final length of each crack. The interface cracks are generated at different inclination angles (δ) to be used for different mixed mode fracture tests as listed in Table 4-1. A total number of 50 BSCB specimens were made for five mixed mode conditions at two temperatures. That means at least five BSCB specimens were prepared for each mode mixity. A typical BSCB specimen made of AC and PCC is shown in Figure 4-5.

4.4.3. Fracture tests

Each BSCB specimen was located inside a three-point bend loading fixture with desired values of S1 and S2, and loaded at the constant rate of 0.4 *mm/min* up to its final fracture. Fracture tests were conducted at two temperatures: 20^{o}C (room temperature) and -20^{o}C. The load–displacement data were recorded during the tests. All the test

samples fractured from the interface crack tip and with negligible non-linear deformation before de-bonding.

Figure 4-6 shows the loading set up for one of the BSCB specimens and a sample fractured specimen. Using the fracture load obtained from each specimen, the critical stress intensity factors of the tested BSCB specimens were calculated from Eq. (4.1) and (4.2). Details of each test including, the fracture loads and the corresponding stress intensity factors are listed in Tables 4-4 and 4.5 for T= -20^{o}C, and T= 20^{o}C, respectively. In Tables 4-4 and 4-5, the specimen codes are PMI: pure mode I, PMII: pure mode II, MM-I: mixed mode type I (S1=30*mm*, S2=20*mm*), MM-II: mixed mode type II (S1=60*mm*, S2=15*mm*), MM-III: mixed mode type III (S1=S2=50*mm*).

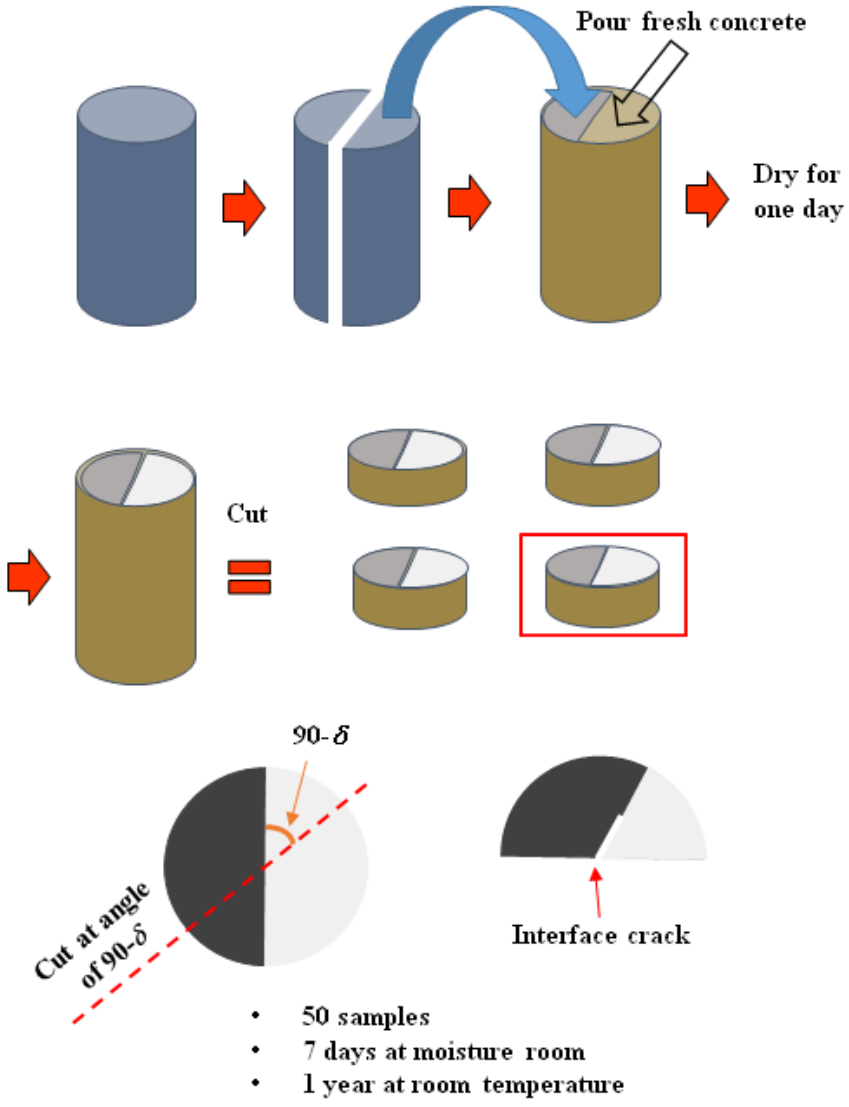

Figure 4-4. Preparation of BSCB specimens made of AC and PCC.

Figure 4-5. A typical BSCB made of AC and PCC with δ=0.

Figure 4-6. Three point bend loading set up for a typical BSCB specimen.

Table 4-4. Summary of the results obtained from mixed mode I/II fracture tests conducted on BSCB specimens made of AC/ PCC, at T = -20°C.

Specimen code	$F_{cr}(N)$	$K_I(MPa\sqrt{m})$	$K_{II}(MPa\sqrt{m})$
PMI-1	3207	0.094062	0
PMI-2	3461	0.101512	0
PMI-3	3420	0.100309	0
PMI-4	2823	0.082799	0
PMI-5	2684	0.078722	0
MM-I-1	5850	0.081807	0.032935
MM-I-2	5740	0.080268	0.032316
MM-I-3	5310	0.074255	0.029895

Table 4-4. continue

Specimen code	$F_{cr}(N)$	$K_I(MPa\sqrt{m})$	$K_{II}(MPa\sqrt{m})$
MM-I-4	5990	0.083764	0.033723
MM-I-5	6120	0.085582	0.034455
MM-II-1	4354	0.05891	0.047444
MM-II-2	4020	0.054391	0.043805
MM-II-3	4200	0.056826	0.045766
MM-II-4	4654	0.062969	0.050713
MM-II-5	3940	0.053308	0.042933
MM-III-1	3120	0.029748	0.04363
MM-III-2	3250	0.030987	0.045448
MM-III-3	3600	0.034324	0.050343
MM-III-4	3740	0.035659	0.0523
MM-III-5	3810	0.036327	0.053279
PMII-1	5741	0	0.052131
PMII-2	5570	0	0.050579
PMII-3	5231	0	0.0475
PMII-4	6020	0	0.054665
PMII-5	5610	0	0.050942

Table 4-5. Summary of the results obtained from mixed mode I/II fracture tests conducted on BSCB specimens made of AC/ PCC, at T = +20°C.

Specimen code	$F_{cr}(N)$	$K_I(MPa\sqrt{m})$	$K_{II}(MPa\sqrt{m})$
PMI-1	1120	0.03285	0
PMI-2	1040	0.030503	0
PMI-3	990	0.029037	0
PMI-4	889	0.026075	0
PMI-5	1201	0.035226	0
MM-I-1	1980	0.027688	0.011147
MM-I-2	1820	0.025451	0.010246
MM-I-3	1760	0.024612	0.009909
MM-I-4	1870	0.02615	0.010528
MM-I-5	1680	0.023493	0.009458
MM-II-1	1420	0.019213	0.015473
MM-II-2	1370	0.018536	0.014928
MM-II-3	1590	0.021513	0.017326
MM-II-4	1310	0.017724	0.014275
MM-II-5	1210	0.016371	0.013185
MM-III-1	1010	0.00963	0.014124
MM-III-2	1090	0.010393	0.015243
MM-III-3	1320	0.012586	0.018459

Table 4-5. continue

Specimen code	$F_{cr}(N)$	$K_I(MPa\sqrt{m})$	$K_{II}(MPa\sqrt{m})$
MM-III-5	1140	0.010869	0.015942
PMII-1	2010	0	0.018252
PMII-2	1980	0	0.017979
PMII-3	1850	0	0.016799
PMII-4	1897	0	0.017226
PMII-5	1782	0	0.016182

4.4.4. Fracture criterion

Almost in all fracture tests, the interface crack propagated through the interface which means the bond behavior between AC and PCC can be characterized as a weak bond. The results for mixed mode interfacial fracture resistance of weak bonds are usually presented in a normalized form as $(K_{II})_C / K_{IIC}$ versus $(K_I)_C / K_{IC}$ as described in section 3 of this dissertation (see Eq. (3.29)). According to the results given Tables 4-4 and 4.5, the averages value of mode I interfacial fracture toughness K_{IC} obtained from the fracture tests (i.e. S1= 50 *mm*, S2 = 38 *mm*) were 0.0915 $MPa\sqrt{m}$ and 0.0307 $MPa\sqrt{m}$, at T = -20°C and T = 20°C, respectively. Also, the average value of the mode II interfacial fracture toughness K_{IIC} obtained from the fracture tests were 0.0511 $MPa\sqrt{m}$ and 0.0173 $MPa\sqrt{m}$, at T = -20°C and T = 20°C, respectively.

The mixed mode test results obtained in this research for various combinations of mode I and mode II are shown in Figures 4-7 and 4-8 in a $(K_{II})_C / K_{IIC} - (K_I)_C / K_{IC}$ diagram, for T= -20°C, and T= 20°C, respectively. Also shown in this figure, the power law criterion needs *2p* = 2.71, *2q* = 2.25 to meet the fracture test data at T = -20°C and

requires *2p* = 2.45, *2q* = 2.15 for T = 20°C. It is worth mentioning that a direct comparison between these two fitting lines (dashed lines in Figure 4-7 and 4-8) shows that the curve corresponding to T = -20°C is slightly higher than that of plotted for T = 20°C. That means one can roughly assume the power law criterion is independent of the test temperature for all values between -20°C and 20°C.

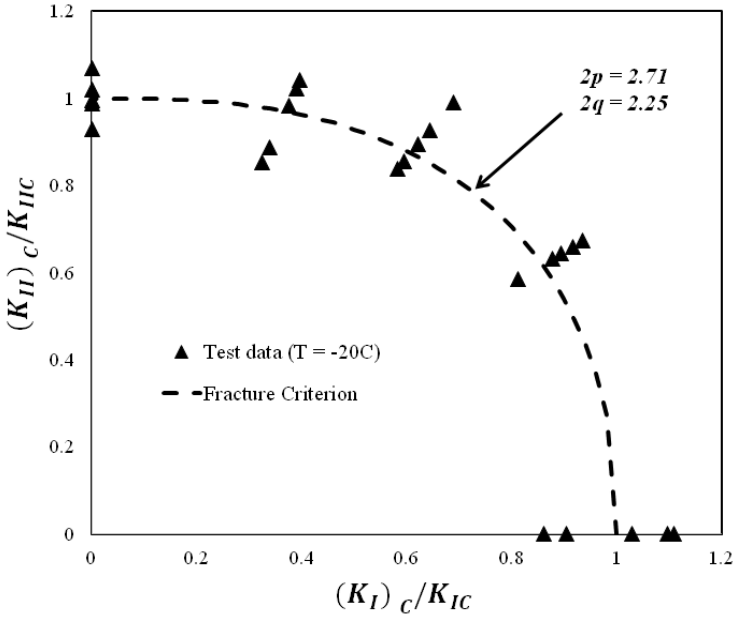

Figure 4-7. Mixed-mode fracture envelope and predictions for AC/ PCC interfacial delamination at T = -20°C.

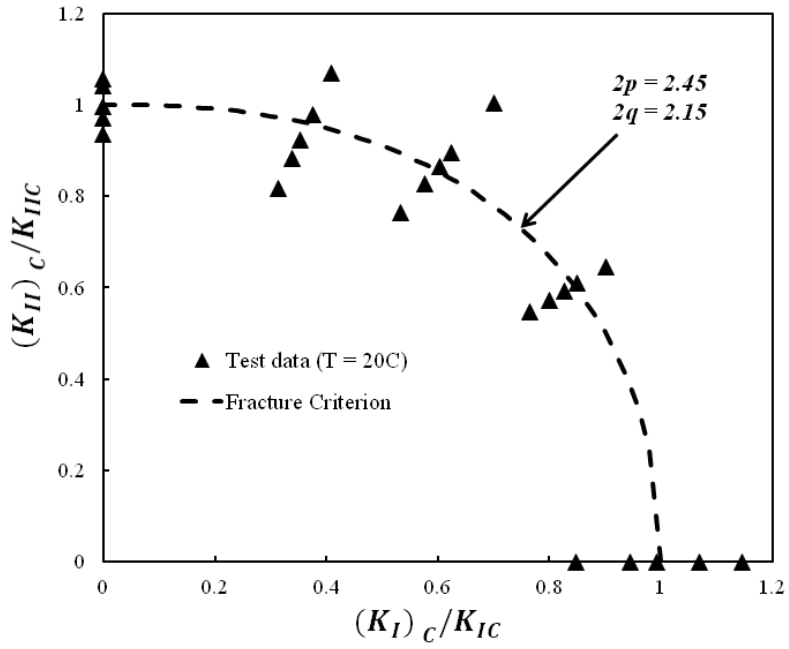

Figure 4-8. Mixed-mode fracture envelope and predictions for AC/ PCC interfacial delamination at T = 20°C.

4.5. Summary and conclusions

A review of the test specimens used in the past for conducting mixed mode fracture experiments revealed that some of them required a complicated test set up. For instance, a biaxial fixture not only made the experiments more expensive but also may be a source of error in the test results due to possible manufacturing inaccuracies. The described BSCB specimen, is simple since it can be tested by use of an ordinary three-point bend fixture which is normally available in standard fracture testing machines. Furthermore, the application of compressive loads in the BSCB experiments makes it more suitable for conducting fracture tests on weak bonded joints which are weak under tensile loads. Although almost all of the mixed mode test specimens can be used for pure

mode I and mixed mode fracture tests, some of them are not able to provide pure mode II. This issue becomes even more important for a bi-material system since not only the geometry, but also the elastic properties of each material control the mode mixity. Another advantage for the BSCB specimen is its ability for providing complete combinations of mode I and mode II including pure mode I, pure mode II and various intermediate mode mixities.

It is worth mentioning that cracked test specimens which contain only one crack tip (like the BSCB specimen), are often preferred to centrally cracked specimens that contain two crack tips (e.g. the centrally cracked square plate, or the centrally cracked Brazilian disk specimen). This is because the crack extension does not necessarily initiate from the two crack tips simultaneously. The delay between the fracture initiations at the two crack tips is not controllable and can sometimes be a likely source of error in the test results.

Because of the advantages elaborated above, the BSCB specimen can be recommended as a favorite bonded sample sample for conducting mixed mode interfacial fracture experiments. Finally, the conclusions can be summarized as follows:

- A new test configuration called the bi-material semi-circular bend (BSCB) specimen was suggested for interfacial mixed mode I/II fracture experiments.
- The simple geometry and loading set up, the ease of generating a crack in the specimen, and the ability of introducing full combinations of mode I and mode II are the main advantages of the BSCB specimen.

- The mixed mode interfacial bond strength between AC / PCC was successfully evaluated using the BSCB specimens at two temperatures.
- The mixed mode power law cohesive fracture model was employed to evaluate interfacial fracture tests on AC/ PCC bonded joints.
- In a concrete pavement, the slab horizontal and vertical (lift-off) end movements are directly affected by the bond strength between concrete slab and the subbase layer. The BSCB specimen can be used for evaluation of the bond strength of concrete slab / subbase interface.
- The results presented in this section for BSCB specimen are at their primary steps and a size effect study is needed in order to characterize that comprehensively.

5. MODELS FOR THE PREDICTION OF DISPLACEMENTS IN CRC PAVEMENTS

5.1. Introduction

The use of concrete as a paving material has a long history that dates back to the early 1900's in the United States. Since its introduction, considerable effort has been made to develop design methods and construction procedures. Due to the environmental loads, end movements occurs in a concrete slab. End movements in CRC pavements is an important distress leading to deterioration of in-service pavement structures. There are many factors affecting displacements and development of stresses in CRC pavements. The bond strength between the concrete slab and subbase layer is one of the most important factors that plays an important role in slab displacement. The separation mechanism at the interface of concrete slab and subbase layer can be addressed by interfacial fracture mechanics concepts, as explained in pervious sections (sections 3 and 4). This section is aimed to study different models for evaluation of the end movements in CRC pavements.

Figure 5-1 shows a scheme of the continuously reinforced concrete pavement (CRCP). CRCP was developed as an alternative to jointed concrete pavement that eliminates the need for contraction joints. In CRCP, longitudinal reinforcement is continuous, in that each individual length of reinforcing bar is lapped end-to-end to each of its adjoining reinforcing bars in the reinforcement grid. The presence of the steel in the pavement does not prevent the formation of cracks. Rather, it induces the concrete to

develop numerous transverse cracks. Theoretically, the steel keeps the cracks tightly closed, which maintains the integrity of the aggregate interlock across the cracks.

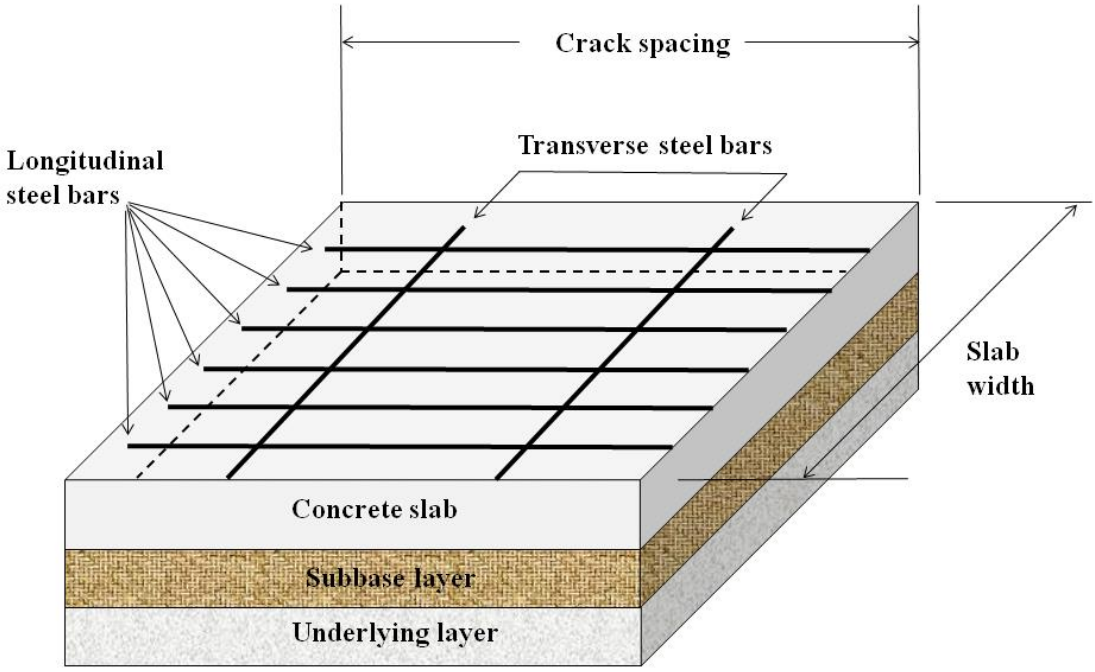

Figure 5-1. General configuration of CRC pavement.

There are many variables that are known to influence the crack spacing, and its developments, including the type and amount of longitudinal steel, the air temperature at the time of placement, the composition and uniformity of the concrete, the base friction, traffic loadings, and the air temperature range relative to the placing temperature. Therefore, the importance of developing a rational method of predicting CRCP behavior based on the mechanics of the pavement structure, the environmental conditions, and the material properties is important [4].

One can find a number of mechanistic models for CRC pavements in the literature. The first mechanistic model of the CRC pavement called CRCP-1, was developed in the mid-1970s under a study sponsored by the National Cooperative Highway Research Program (NCHRP) [143]. This computer program evaluated the effect of such design variables as layer thicknesses and properties, concrete strength, and steel reinforcement, together with environmental and traffic loads, such as temperature variation, drying shrinkage, wheel load, and tire pressure. In 1991, Won et al. [144] developed an improvement to the CRCP program, CRCP-5, that simulates material variance to concrete tensile strength and includes fatigue failure models. The normalized curing curves were determined for different coarse aggregates commonly used in Texas pavements [145], and these curves and the calibrated failure prediction model were included in CRCP-7 [28]. In 1995, previous versions of the CRCP programs were integrated into one program, CRCP-8, with simplification of the user input process [146]. Although CRCP-8 has permitted pavement engineers to develop design of the CRC pavements, there were some limitations owing to the simplified assumptions of the one dimensional analysis. In 1996, Texas Department of Transportation (TxDOT) was conducted to expand the ability of the mechanistic model by incorporating the variations in temperature and moisture changes through the depth of concrete slab. As a result of that work, a two-dimensional finite element model was developed [147, 148]. In 1998, the more comprehensive version of the work done by TxDOT led to develop CRCP-9. CRCP-9 used two-dimensional finite element theories to reduce the cost of the computation, but in order to increase the accuracy of the 2D model, three-dimensional

analyses were performed first using finite element method, and the differences between 2D and 3D analysis results were investigated [149, 150]. The CRCP models were then modified even more, CRCP-11, to design CRCP under different climatic conditions in a more sophisticated manner.

However, the CRCP models have some limitations as will be discussed in the following. Although they provide good approximations of true behavior for some conditions, the large number of simplifying assumptions (especially for early versions CRCP-1, CRCP-2, and CRCP-3) that were made to develop the models limit its accuracy to a great extent. Although many of the assumptions are necessary to reduce the mathematical complexity of the model to a manageable level, some are gross simplifications of the conditions that actually exist in the pavement system. Assuming that the bond stress between the steel and the concrete acts as an average value over a specified development length is one such assumption. Research has shown that the actual bond stress distribution has a range of values that vary from zero to a peak magnitude that far exceeds the average value [151]. Assuming an average bond stress distribution severely limits the validity of the CRCP model in many instances. In cases where there is high frictional resistance between the base material and the pavement slab, or there is a large temperature drop, the computed development length for the bond stress can actually exceed the length of the slab over which the bond forces have to act [142]. This is a physical impossibility in an actual pavement, since the concrete and the steel have to be fully bonded at the midpoint of the slab. In addition, the stress distributions in both the steel and the concrete are governed, in part, by the bond stress

distribution between them. If the bond stress distribution is invalid, then the stress distributions in the steel and the concrete will also be invalid. Other assumptions that limit the accuracy of the CRCP models include: 1) modeling the concrete as a linear, elastic material, 2) assuming that the temperature variations and shrinkage strains are uniform throughout the slab, and 3) neglecting the effect of creep and slab warping.

The displacement, stress, and strain fields in CRC pavement due to different loading configurations were also characterized by other researchers. One of the pioneering analytical works on the study of the mechanism of the slab deformation due to the environmental effects is the work done by Palmer [4]. He represented stress, strain and displacement field in CRCP and calculated relative displacements between concrete slab and subgrade, and between concrete slab and reinforcing steel bar. However, the effect of lift-off (slab's vertical displacement) on the slab end movement as well as the effect of interfacial delamination were not taken into account.

According to the literature survey presented above, one can realize that none of the above models takes into account the effect of cohesive bond strength on the slab displacements. In the all previous models, the bond behavior between concrete slab and base layer is modelled as friction models which do not represent the effect of interfacial crack propagation, at the interface of concrete slab and base layer, due to the environmental loads. This research aims to study effect of bond strength on the slab displacements using interfacial fracture mechanics approaches. First, some Palmer's model [4] is explained and then, a modified version of the Palmer's model is presented which takes into account the effect of slab lift-off together with the interfacial fracture

theories. The two analytical models are compared and their advantages, disadvantages, and limitations are discussed. The predictions provided by the modified Palmer's model are compared to the results obtained from two-dimensional simulation of a plain concrete pavement subjected to a typical environmental load. Then, a 3D finite element approach is employed to investigate slab displacements taking into account the bond strength between concrete slab and base layer using cohesive zone model. Finally, the developed 3D finite element simulation is then employed to predict experimental data available in the literature for displacements in a concrete slab due to the environmental loading.

5.2. Palmer's model for CRC pavement

Palmer [4] developed a mechanistic model for the prediction of stresses, strains and displacements in CRC pavements. Comparing with other CRCP models discussed above, he presented a more sophisticated method taking into account the effect of bond slip distribution (for both steel/ concrete and concrete/ subbase interfaces) on the slab displacements. Followings are the assumptions he used for the model:

a) The concrete and the reinforcing steel behave in a linearly elastic manner.
b) The base material underneath the concrete slab is rigid, and will not deflect under loading by the horizontal friction force.
c) All materials are homogenous.
d) All temperature and shrinkage induced strains are uniformly distributed throughout the depth and the width of the CRCP slab.

e) The effect of curling, warping, and creep will be ignored.

f) All behavior in the slab is symmetrical about the midpoint of the slab.

By assuming that the temperature and shrinkage are uniformly distributed throughout the width of the slab, the slab can be modeled as a prism with a length equal to the one-half the length of the slab as shown in Figure 5-2. The prism has a thickness t_0 (equal to the slab thickness), and a width b which corresponds to the spacing of the steel reinforcement. There is also a cylindrical reinforcing steel bar running through the length of the prism. The governing equations for horizontal displacement due to shrinkage strain, ε_s, can be obtained by taking a slice of the prism of width Δx. As shown in Figure 5-3, a change in the magnitude of both the concrete stress, σ_c, and the steel stress, σ_s, occurs across the width of the slice, which equals $\Delta\sigma_c$ and $\Delta\sigma_s$, respectively.

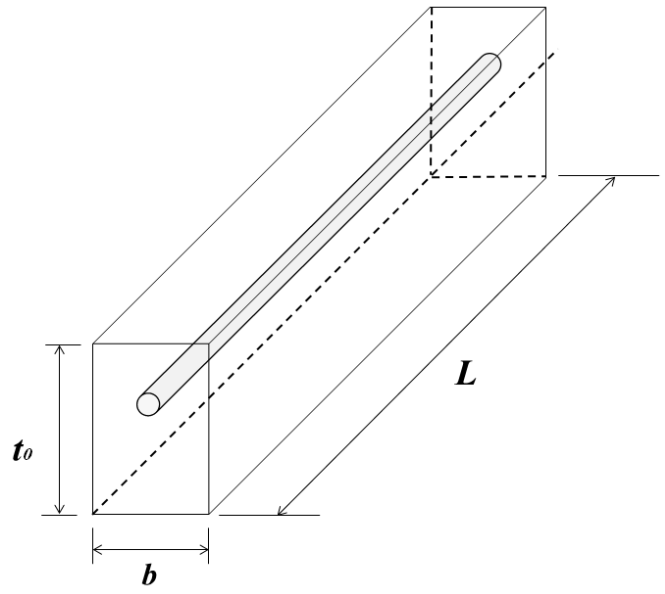

Figure 5-2. Prism used to model the CRC slab in Palmer's model [4].

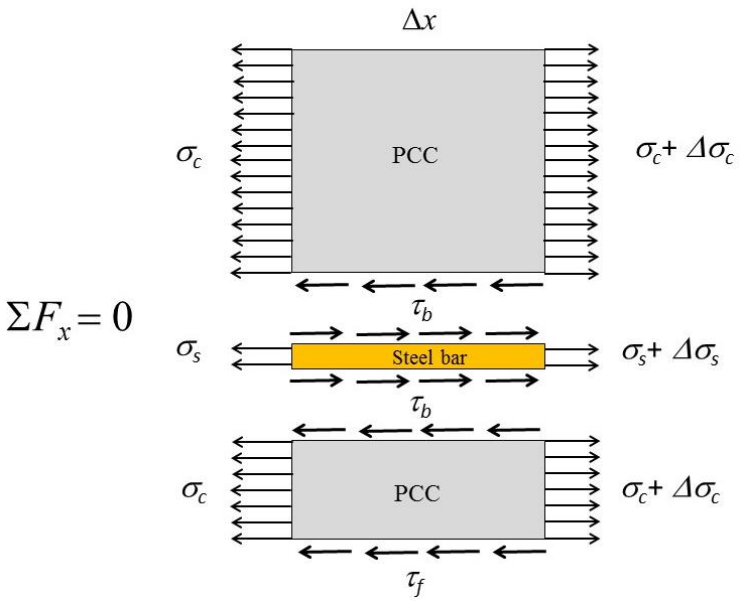

Figure 5-3. Stresses acting upon an elemental slice of the prism, in *x* direction.

The bond stress, τ_b, is present between the reinforcing steel and the concrete, and another bond stress, τ_f, is present between the concrete and base materials. Using the equilibrium equation in *x* direction, the following differential equations can be obtained for horizontal displacement of the concrete and steel as given in Eq. (5.1) and Eq. (5.2), respectively.

$$\frac{d^2\hat{u}_c}{dx^2} = \left(\frac{\pi d_s}{E_c A_c}\right)\tau_b + \left(\frac{b}{E_c A_c}\right)\tau_f \tag{5.1}$$

$$\frac{d^2\hat{u}_s}{dx^2} = -\left(\frac{\pi d_s}{E_s A_s}\right)\tau_b \tag{5.2}$$

where $\hat{u}_c$ and $\hat{u}_s$ are displacement of the concrete and steel due to the slab shrinkage. The expressions for shear stresses can be obtained by applying interfacial fracture mechanics concepts, which will be discussed later. Applying the boundary conditions and using the expression given by the interfacial fracture mechanics, one can find the horizontal contraction deformation. The boundary conditions are:

$$\hat{u}_c = \hat{u}_s = 0 @ x = L \tag{5.3}$$

$$\frac{d\hat{u}_c}{dx} = \frac{d\hat{u}_s}{dx} = 0 @ x = L \tag{5.4}$$

The bond stresses (τ_b and τ_f) must be characterized in order to solve Eq. (5.1) and Eq. (5.2). All that remains is to substitute the correct expressions for the bond stresses and solve the differential equations for the displacements $\hat{u}_c$ and $\hat{u}_s$. Palmer [4] suggested the three-part linear functions given in Eq. (5.5) and Eq. (5.6) to model both τ_b and τ_f as;

$$\tau_b = \begin{cases} K_1(\hat{u}_c - \hat{u}_s), & if \quad 0 \le (\hat{u}_c - \hat{u}_s) \le \delta_b \\ C_1 + K_2(\hat{u}_c - \hat{u}_s), & if \quad \delta_b \le (\hat{u}_c - \hat{u}_s) \le \delta_{bl} \\ 0, & if \quad (\hat{u}_c - \hat{u}_s) > \delta_{bl} \end{cases} \tag{5.5}$$

$$\tau_f = \begin{cases} K_3\hat{u}_c, & if \quad 0 \le \hat{u}_c \le \delta_b \\ C_2 + K_4\hat{u}_c, & if \quad \delta_b \le \hat{u}_c \le \delta_{bl} \\ 0, & if \quad \hat{u}_c > \delta_{bl} \end{cases} \tag{5.6}$$

The parameters K_1, K_2, K_3, K_4, C_1, C_2, δ_b, and δ_{bl} should be calibrated for reinforced steel deformation patterns and subbase types. Eq. (5.5) and Eq. (5.6) suggest a

formulation for shear stresses which relates the stresses to the relative displacements between concrete slab and streel bar, and between concrete slab and the base layer. However, interfacial crack propagation is not taken into account for the formulation given by Palmer [4].

5.3. Modified Palmer's model for CRC pavement

Palmer's model does not take into account effect of slab's lift-off on the horizontal displacement. In other words, Palmer's model is developed in a one dimensional framework. However, a concrete slab deforms upward as a result of temperature and moisture gradient throughout the slab thickness. Figure 5-4 illustrates the two-dimensional model of the slab deformation. The net strain gradient which causes as a result of temperature and moisture gradient (mainly temperature gradient) is considered as ε_c and the net strain caused by the shrinkage is shown as ε_s.

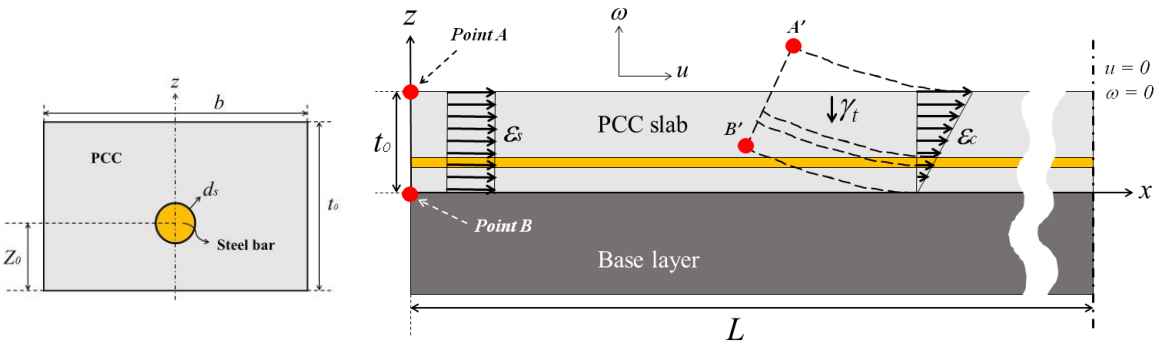

Figure 5-4. 2D scheme of the end movement in a reinforced concrete beam.

The net strain can be linear or nonlinear with respect to the z direction, however, an equal linear net strain profile can roughly be obtained for nonlinear cases using strain energy concept. The net lift-off displacement can be calculated by subtraction of the effect of slab weight from the effect of moisture and temperature gradient as:

$$w = w_c - w_w \tag{5.7}$$

where, w, w_c, and w_w are displacements in *z* direction for total, due to the temperature and moisture gradient, and due to the slab weight, respectively. The profiles for w_c and w_w can be obtained from Eq. (5.8) and Eq. (5.9), as follows:

$$\frac{d^2 w_c}{dx^2} = \frac{\varepsilon_c}{t_0} \tag{5.8}$$

$$E_c I_t(z_0) \frac{d^2 w_w}{dx^2} = M(x) = \gamma_t t_0 \frac{x^2}{2} \tag{5.9}$$

where, ε_c is the equivalent linear lift-off strain profile due to the temperature and moisture gradient (see Figure 5-4). This equivalent strain can be calculated by equalizing experimental strain profile with an asymptotic linear profile using strain energy density concept ($\int \sigma . d\varepsilon$). The actual strain profile is a function of moisture and temperature gradient and can be expressed in Eq. (5.10) as:

$$\varepsilon_c(z) = f(H(z), T(z)) = \frac{\Delta\sigma_c(z)}{E_t} = \frac{1}{E_t}\left(\frac{\partial \sigma_c(z)}{\partial T} . dT + \frac{\partial \sigma_c(z)}{\partial H} . dH \right) \tag{5.10}$$

where E_t is the equivalent combined Young's modulus, and *H(z)* and *T(z)* are moisture and temperature profiles, respectively. The net stress, or strain profiles given in Eq. (5.10) can be determined experimentally.

In Eq. (5.9), the parameter γ_t is the total unit weight of the reinforcing concrete, and I_t is the equivalent second moment of inertia (steel and concrete) with respect to the *y* axis. The parameter I_t is a function of location of the steel bar, z_0, and as a result, the slab lift-off is be obtained as function of z_0. The E_c parameter is the Young's modulus of the concrete. Using Eq. (5.8) and Eq. (5.9), the Eq. (5.7) can be rewritten as follows;

$$\frac{d^2w}{dx^2} = \frac{d^2w_c}{dx^2} - \frac{d^2w_w}{dx^2} = \frac{\varepsilon_c}{t_0} - \frac{\gamma_t t_0}{E_c I_t(z_0)} \frac{x^2}{2} \tag{5.11}$$

Applying the boundary conditions, one can find the slab lift-off easily. Here we assume that the primary reason for interface crack propagation is the slab shrinkage due to the horizontal deflection. This can be a proper assumption since the slab displacement in mostly influenced by the horizontal shrinkage rather than the slab lift-off and the interface crack has already propagated when the slab tends to curl upward. The boundary conditions for Eq. (5.11) are:

$$\frac{dw}{dx} = w = 0 @ x = L \tag{5.12}$$

Applying boundary conditions given in Eq. (5.12), the vertical displacement, *w(x, z)*, can be obtained as:

$$w(x,z) = \frac{\varepsilon_c(z)}{2t_0} x^2 - \frac{\gamma_t.t_0}{24D(z_0)} x^4 + \left[\frac{\gamma_t.t_0}{6D(z_0)} L^3 - \frac{\varepsilon_c(z)}{t_0} L \right].x + \left[\frac{\varepsilon_c(z)}{2t_0} L^2 - \frac{\gamma_t.t_0}{8D(z_0)} L^4 \right] \tag{5.13}$$

Where, $D(z_0) = E_c I_t(z_0)$. Assuming that the radius of the curvature shown in Figure 5-4 is larger than the slab's dimension, the total horizontal displacement of the concrete slab, with respect to the base layer, can be obtained as the following:

$$u_c(x,z) = \hat{u}_c(x) + \left|\frac{dw}{dx}\right|.z \tag{5.14}$$

$$u_s(x,z) = \hat{u}_s(x) + \left|\frac{dw}{dx}\right|.z \tag{5.15}$$

The Eq. (5.14) and Eq. (5.15) must be solved in order to obtain displacements in concrete slab and the reinforcing steel bar. The above explanation for the modified version of the Palmer's method, takes into account the effect of slab's lift-off. However, the effect of interfacial crack propagation is to be accounted for yet.

Figure 5-5 shows a two-dimensional scheme of area with stress concentration in a reinforcing concrete slab/base structure. As given in Eq. (5.1) and Eq. (5.2), the governing differential equation requires bond tress distribution between concrete slab and base, τ_f, and between concrete and the steel bar, τ_b. These ultimate bond stresses can be characterized using interfacial fracture mechanics. Before the crack initiation, we have a notch at the interface of two dissimilar materials, and once crack propagates (even a very short crack), we have a crack existing at the interface of two dissimilar materials which may propagate along the interface or may kink into one of the base materials. Crack will be created at the interface of two dissimilar materials when the stress field around the notch tip reaches a critical value. In a real pavement structure, the

interface crack always exists since the initial crack length can be assumed as the size of an air void.

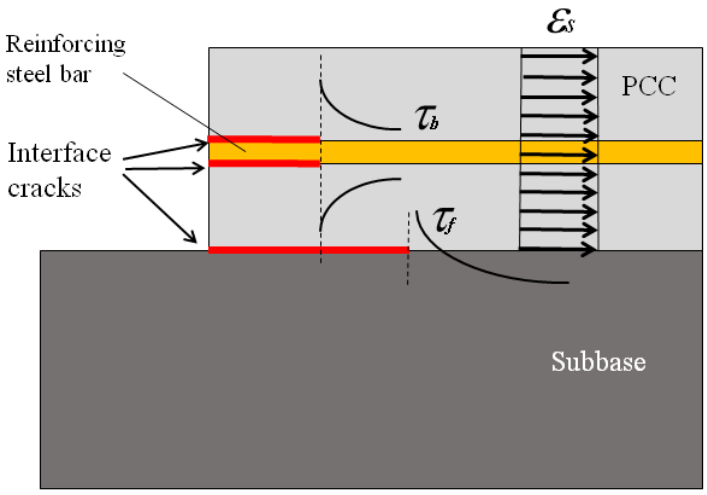

Figure 5-5. Areas with stress concentrations and interface cracks in a CRCP structure, together with the typical shear stress profiles.

The shear stresses given in Eq. (5.1) and Eq. (5.2) can be considered as a function of *x*, along the interface. As comprehensively discussed in section 3 of this dissertation, the stress field around an interface crack tip can be considered as a series of expansion with infinite numbers. Therefore, considering shear stresses as function of *x*, along the interface, and defining parameters *A*, *B*, and *C*, one can rewrite the Eq. (5.1) and Eq. (5.2) as following:

$$\frac{d^2\hat{u}_c}{dx^2} = A\tau_b(x) + B\tau_f(x) \tag{5.16}$$

$$\frac{d^2\hat{u}_s}{dx^2} = C\tau_b(x) \tag{5.17}$$

Where *A*, *B*, and *C* are $\frac{\pi d_s}{E_c A_c}$, $\frac{b}{E_c A_c}$, and $-\frac{\pi d_s}{E_s A_s}$, respectively.

According to the Eq. (3.1) in section 3 and considering only singular stress field, the shear stresses along the interface in vicinity of the crack tip can be expressed as follows;

$$\tau_b(x) = \frac{\hat{K}_I}{\sqrt{2\pi x}}\,\hat{f}_{xy-1} + \frac{\hat{K}_{II}}{\sqrt{2\pi x}}\,\hat{f}_{xy-2} \tag{5.18}$$

$$\tau_f(x) = \frac{K_I}{\sqrt{2\pi x}}\,f_{xy-1} + \frac{K_{II}}{\sqrt{2\pi x}}\,f_{xy-2} \tag{5.19}$$

where $\hat{f}_{xy-1}$, $\hat{f}_{xy-2}$, f_{xy-1}, and f_{xy-2} are known functions of materials properties and geometries, and $\hat{K}_I$, $\hat{K}_{II}$, K_I, and K_{II} are the stress intensity factors (see section 3). Indeed more terms must be added to cover for a larger distance from the crack tip. However, Eq. (5.16) and Eq. (5.17) are solved by taking into account only the singular terms of the shear stresses. Substituting Eq. (5.18) and Eq. (5.19) into Eq. (5.16) and Eq. (5.17), the governing differential equations can be rewritten as;

$$\frac{d^2\hat{u}_c}{dx^2} = A\left(\frac{\hat{K}_I}{\sqrt{2\pi x}}\,\hat{f}_{xy-1} + \frac{\hat{K}_{II}}{\sqrt{2\pi x}}\,\hat{f}_{xy-2}\right) + B\left(\frac{K_I}{\sqrt{2\pi x}}\,f_{xy-1} + \frac{K_{II}}{\sqrt{2\pi x}}\,f_{xy-2}\right) \tag{5.20}$$

$$\frac{d^2\hat{u}_s}{dx^2} = C\left(\frac{\hat{K}_I}{\sqrt{2\pi x}}\,\hat{f}_{xy-1} + \frac{\hat{K}_{II}}{\sqrt{2\pi x}}\,\hat{f}_{xy-2}\right) \tag{5.21}$$

Applying the boundary conditions given in Eq. (5.3) and Eq. (5.4), the above differential equations can be solved in the followings form;

$$\hat{u}_c = \frac{\hat{X}}{\sqrt{2\pi}}\left(\frac{4}{3}.x^{3/2} - 2\sqrt{L}.x + \frac{2}{3}.L^{3/2}\right) \tag{5.22}$$

$$\hat{u}_s = \frac{\hat{Y}}{\sqrt{2\pi}}\left(\frac{4}{3}.x^{3/2} - 2\sqrt{L}.x + \frac{2}{3}.L^{3/2}\right) \tag{5.23}$$

Where $\hat{X}$ and $\hat{Y}$ are defined as;

$$\hat{X} = A\left(\hat{K}_I\,\hat{f}_{xy-1} + \hat{K}_{II}\,\hat{f}_{xy-2}\right) + B\left(K_I\,f_{xy-1} + K_{II}\,f_{xy-2}\right) \tag{5.24}$$

$$\hat{Y} = C\left(\hat{K}_I\,\hat{f}_{xy-1} + \hat{K}_{II}\,\hat{f}_{xy-2}\right) \tag{5.25}$$

The stress intensity factors (and higher order terms) should be determined using numerical simulations of the structure, in order to calculate the shear stress. The variation of the stress intensity factor with different CRCP geometries (steel percentage, slab dimensions) and loading configuration is discussed in section 6 of this dissertation.

A classical method for describing bond behavior between the concrete slab and the base layer is the friction model. According to the friction models, the concrete slab resists against any movement on the subbase layer with a coefficient of friction of μ_s. Here we can relate this classical parameter to the formulations presented in modified Palmer's model. The uniform friction force on a piece of slab with the volume of ΔV, as a result of slab's weight can be expressed as following according to its classical definition;

$$F_s(x) = \mu_s.\Delta V.\gamma_t = \mu_s.(t_0.x.b).\gamma_t \tag{5.26}$$

The bond shear stress, shown in Figure 5-5, can be expressed as given in Eq. (5.27) where τ_u is the ultimate interface shear strength and $\tau_{xy}(x)$ is the same equation given in Eq. (3.1) (see section 3 for more details). The ultimate shear strength of the bond, τ_u, can be obtained using interfacial fracture tests (see section 4 for details).

$$\tau_f = \begin{cases} \tau_u & x < r_c \\ \tau_{xy}(x) & x \geq r_c \end{cases} \tag{5.27}$$

The parameter r_c in Eq. (5.27) is the radius of the damaged zone around the interface crack (see section 3 for more details). The equivalent friction force on an element with the width of *dx* as a result of the shear stress between the concrete slab and the subbase can be obtained as;

$$dF_s = \tau(x).dA = \tau(x).b.dx \tag{5.28}$$

Then, the friction force for $x \geq r_c$ can be calculated as;

$$F_s(x) = b(r_c.\tau_u + \int_{r_c}^{x} \tau_{xy}(x).dx) \tag{5.29}$$

Using Eq. (5.26) and Eq. (5.29), the relationship between the classical coefficient of friction and the interfacial shear stress can be calculated as the following form;

$$\mu_s = \frac{r_c.\tau_u + \int_{r_c}^{x} \tau_{xy}(x).dx}{t_0.\gamma_t} \tag{5.30}$$

In Eq. (5.30), the number of stress terms, given in Eq. (3.1), is an important parameter which needs to be considered. For distances very close to the interface crack tip, one can cover the shear stress by taking into account only singular stress terms. However, for distances far from the crack tip, the higher order terms should be considered for the shear stress field. Similar methodology can be used for the bond strength between the reinforcing steel bar and the concrete slab. However, since the current research focuses on the bond behavior between the concrete slab and base layer,

we use the data given in the literature for evaluation of the bond strength between concrete slab and the reinforcing steel bar.

As discussed above, the shear stress distribution suggested by Palmer [4] is now reformulated in terms of the stress field around an interface crack. Also, the modified model provides a two-dimensional framework taking into account the slab's lift-off. Such modification provides a more realistic description on the stresses, strains, and displacements in CRC pavement.

In order to examine accuracy of the modified Palmer's method, an example is presented in the following for comparison between the modified Palmer's method and the finite element simulation. Since there are some unknown parameters in traditional Palmer's method which cannot be characterized in a straightforward manner, only the modified version of it is examined here. As discussed above, the modified Palmer's model requires stress intensity factors which can easily be calculated using finite element simulation, however, the traditional Palmer's model requires calibration of some parameters related to the relative bond slip between concrete slab and the subbase layer which should be characterized by the experiments.

Because of the geometry of CRCP, one cannot simulate it in a two-dimensional finite element framework. Therefore, the following example is on the simulation of a plain concrete pavement instead of the CRCP ($d_s = 0$). The selected material properties for the plain concrete pavement are: E_c = 34000 MPa, $\nu_c = \nu_{sub}$ = 0.2, and E_{sub} = 3500 MPa, and concrete density of 2400 kg/m^3. The half slab length of L = 4.5m, slab thickness of t_0 = 0.3m, and subbase thickness of t_{sub} = 0.1m were selected for the

geometry of the structure. The fracture criterion parameters (for weak interfaces, according to Eq. (3.29)) were also selected as $K_{IC} = K_{IIC} = 0.05MP.m^{0.5}$, $p = q = 2$, and the $\sigma(z) = 0.5+2z$ MPa was selected as the net stress profile through the slab thickness. Figure 5-6 depicts mesh pattern used for the two-dimensional finite element simulation of the concrete pavement. In the finite element analysis, 6-node quadratic triangular singular elements were used for the first row of elements surrounding the interface crack tip and 8-node quadratic quadrilateral elements were utilized for the rest of the model.

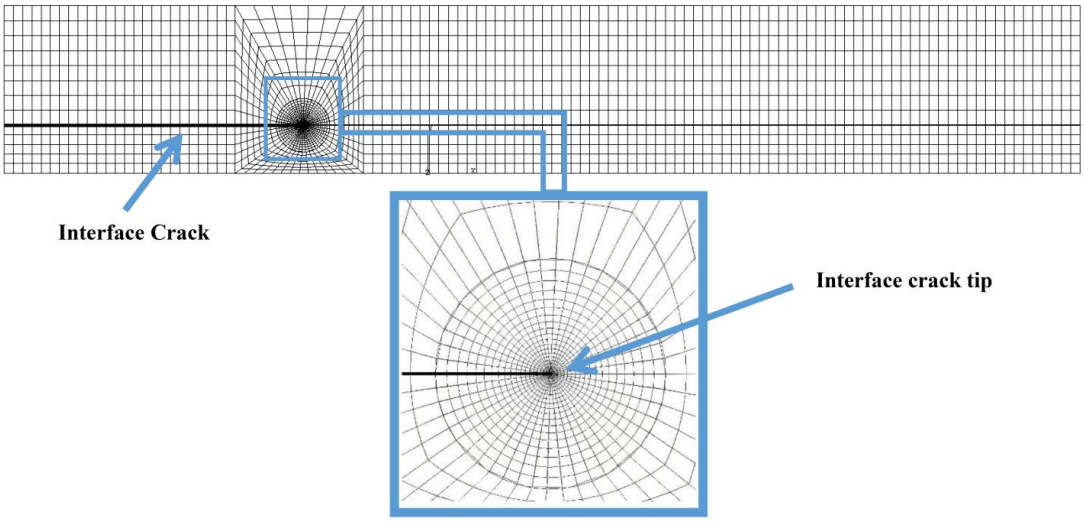

Figure 5-6. Mesh pattern used for the two dimensional finite element simulation of a concrete slab placed on the subbase layer, as well as an expanded view of the interface crack tip elements.

In the finite element model, the crack length is increased manually in different steps until the stress intensity factors developed around the interface crack tip become lower than their critical value (see Eq. (3.29)). At the final step, the interface crack length reaches its maximum value and displacements at points A and B, which are associated with top and bottom of the slab, (shown in Figure 5-4) are measured. Table 5-

1, lists displacements at point A and B obtained by modified Palmer's model and the two-dimensional finite element simulation. It is seen that the modified Palmer's model predicts the two-dimensional finite element results with acceptable accuracy.

Table 5-1. Comparison between predictions provided by modified Palmer's method and the two-dimensional finite element simulation.

Method	u_A(mm)	w_A(mm)	u_B(mm)	w_B(mm)
2D-FEM	3.27	1.66	0.45	0.33
Modified Palmer's	2.9	1.92	0.39	0.41

Although, the closed form formulation presents a more sensible description of the slab's movement, it uses some assumptions at the beginning which sometimes may lead to errors in prediction of the displacements. Using the finite element simulation, one can assume any temperature and moisture gradients throughout the concrete slab. In addition, it is very hard to obtain displacements induced by environmental loads at multiple load steps using the closed form solutions. Therefore, researchers recently have used the finite element method for simulation of the slab's movements. As mention previously in this section, many of the finite element simulations done in the past are two-dimensional. However, the geometry of the CRC pavement does not allow to simulate that as a two-dimensional model. The next section describes a three-dimensional finite element procedure for evaluation of the slab's movements subjected to environmental loads. The suggested method uses cohesive zone elements at the interface of concrete slab and subbase layer, and at the interface of concrete slab and the reinforcing steel bar.

5.4. Three-dimensional finite element modeling

The analytical models presented above always need some assumptions in their presented solutions. Such assumptions sometimes are source of errors in estimation of the displacements, strains, and stresses in concrete pavements. Here, we present a three-dimensional finite element simulation approach to evaluate slab's movement due to the environmental loading. Using the finite element approach, we can significantly reduce the number of assumptions considered by the theoretical solutions, especially the following ones;

a) No limitation on the material properties: for instance in Palmer's model the subbase was assumed to be a rigid material. However, this assumption was dismissed in the proposed modified Palmer's model.
b) One can apply any bond behavior between concrete slab and subbase layer using finite element approach: as will be discussed later, the cohesive elements are used for interface elements between concrete slab and the subbase and between the concrete slab and the reinforcing steel bar.
c) Any temperature and moisture gradients can be assumed throughout the concrete slab: for analytical solutions, it was very hard and sometimes impossible to solve for nonlinear gradients.
d) Any slab's displacement can be simulated and no assumption is needed for any warping effects or other types of out of plane deformations.

In the current research, the commercial software ABAQUS is used as a finite element tool to simulate CRCP structures. In this section, we first briefly introduce the

geometry of the model and then, the materials properties of each part of the model, boundary conditions, and loading profiles are discussed. Finally, the three-dimensional cohesive zone model is utilized to predict experimental data given in the literature for displacements in a concrete slab due to the o given moisture and temperature profile.

5.4.1. Geometry of the model

Figure 5-7 shows a prism taken out of the middle of the edge of a typical CRCP structure. Since we are interested in end movement in concrete slabs, the prism is taken out of end of the CRCP structure. In fact, the corner and the edge of a concrete slab lift-off upward in different manners.

The deformation at the corners can also be easily simulated by applying the corresponding boundary conditions. However, in the current research, we focus on the end movements in the middle of the concrete slab. The reinforcing bar in CRC pavement has the spacing of b, and dimeter of d_s placed at the distance z_0 from the subbase layer. The selected prism has the length of L, and the thickness of the concrete slab and the subbase are t_0 and t_{base}, respectively. Interface cohesive elements are used to connect concrete slab and subbase layer, as well as the concrete slab and the reinforcing steel bar. The constitutive model for the cohesive zone model used for the simulation is described in part 5.4.2 of the current section. The same geometry can be used for plain concrete slabs by assuming d_s as zero.

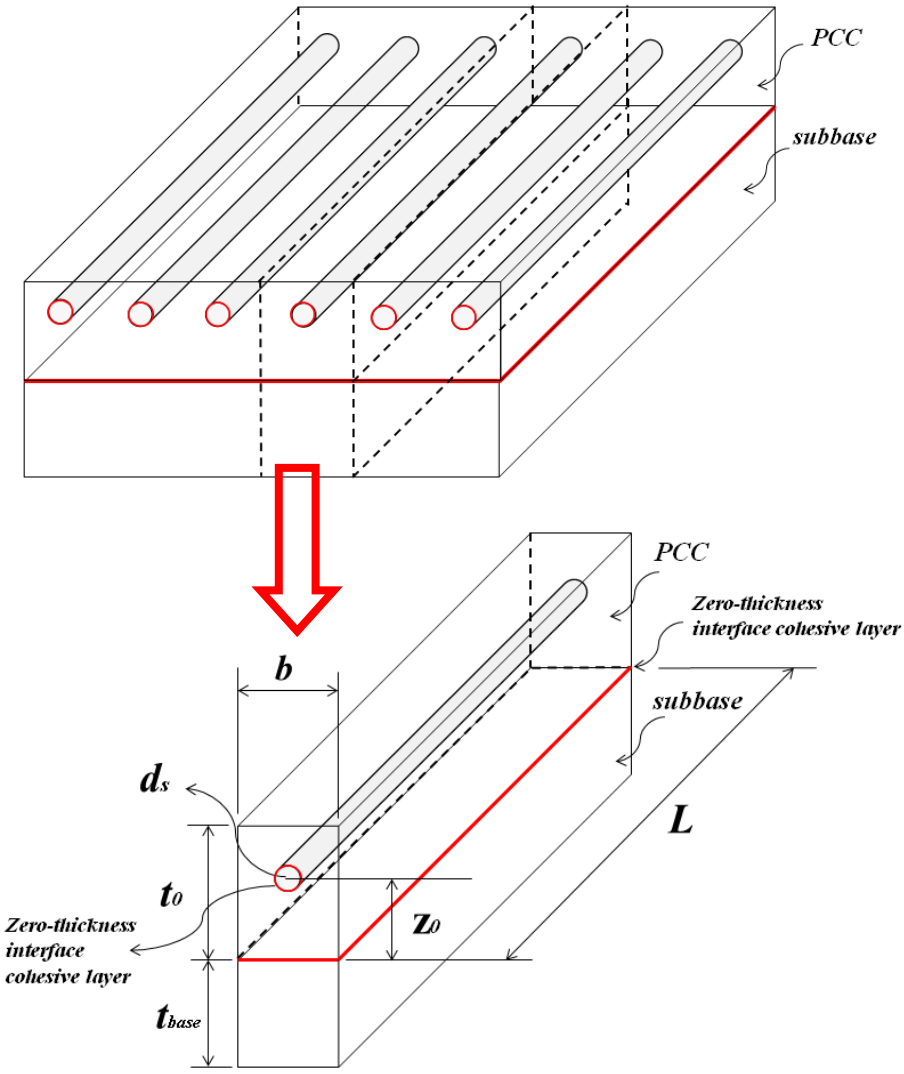

Figure 5-7. Geometry of the CRCP structure used for the three-dimensional finite element simulation.

5.4.2. Material properties

The materials used for the three-dimensional finite element modeling consist of: Portland cement concrete, subbase layer, reinforcing steel bar, and cohesive zones. A brief description of each materials is given as follows;

Portland cement concrete: in the current research, the Portland cement concrete is considered as a homogeneous material. Indeed, the Portland cement concrete should be modelled as a composite materials when it is studied in a multi-scale framework. However, assuming Portland cement concrete as a homogeneous material may be an acceptable assumption since we are interested in general deformation of the concrete and the interaction between the concrete ingredients (cement and aggregates) is not studied in this research. Also, a thermo-elastic material model is utilized to model the concrete behavior. In other words, the Portland cement concrete can be characterized by its density, modulus of elasticity, Poison's ratio, and the coefficient of thermal expansion. It is assumed that material properties are constant during temperature and moisture variations. It is assumed that the deformation in concrete slab does not cause significant cracking in concrete slab and whole fracture energy release as a result of de-bonding between the concrete slab and subbase layer, and reinforcing steel bar.

Subbase material: the subbase layer is also assumed as a homogeneous material and is modelled using the linear elastic material model. Therefore, the subbase material can be simply characterized by its density, modulus of elasticity, and the Poison's ratio. Simulating subbase material as linear elastic material model means that its material properties is assumed not to be sensitive with respect to the temperature and moisture variations. However, when a viscoelastic material is used as the subbase layer, we should be take into account the temperature effects as well and use a proper linear/ nonlinear viscoelastic material model.

Reinforcing steel bars: the reinforcing steel bar is assumed as a homogeneous material behaving like a thermo-elastic material model. That means the material properties required for modeling the steel bar are modulus of elasticity, Poison's ratio, density, and the coefficient of thermal expansion.

Cohesive zones: The cohesive elements are used at the interface of concrete slab and subbase layer as well as between the concrete slab and the reinforcing steel bar. A brief explanation on the cohesive elements is given in the following.

ABAQUS [152] offers a broad set of cohesive elements and features. For modeling surface-bonded structures, the traction-separation constitutive response option is recommended. It is intended for cases where the adhesive is very thin, often so thin as to be impractical to accurately define its physical thickness. Bulk material properties of the adhesive are often unknown or not applicable to the analysis. The user even has the option in this approach of modeling an adhesive with zero thickness. The traction-separation constitutive law relates stresses to separations in the though thickness, and transverse shear directions. Figure 5-8a shows the general form of the traction-separation material response for cohesive modeling in ABAQUS [152] – a triangle. It is important to note that the law uses the bond separation distance instead of physical strain as the independent axis. It is formulated this way to accommodate the common case of a "zero" thickness bond. The constitutive relationship depicted in Figure 5-8a is a one-dimensional relationship. In ABAQUS [152], the actual behavior is generalized to accommodate 2D and 3D analyses (see ABAQUS documentation [152] for additional details). The basic concept in the cohesive element approach is that the cohesive

elements carry loads to constrain the two parts together until loads and deformations on the cohesive elements cause damage and failure. When the element has fully failed, it will have accounted for an amount of energy equal to the critical fracture energy defined for the real material. To accommodate this within a finite element framework, the cohesive material must have finite definitions of stress and separation over which the fracture energy can be released. For the triangular law used by ABAQUS [152], the cohesive element exhibits recoverable linear elastic behavior until the tensile separation has exceeded δ_o, beyond which damage occurs, and ultimately element failure if the separation exceeds the material's failure separation, δ_f. A physical interpretation of this failure separation parameter, δ_f , is that it characterizes the cohesive material's ductility. As such, we will also refer to δ_f as the cohesive ductility.

Classical methods of analyzing fracture and peeling assume that the bond or cohesive material is infinitely stiff in its bonding directions until fracture, upon which a finite amount of fracture energy G_c is released. Figure 5-8b, provides an interpretation of this assumption within the context of a traction-separation constitutive construct. An impulsive-like behavior is defined as the limit of the cohesive ductility, δ_f, goes to zero (and the ultimate stress goes to infinity), but that the area under the curve remains finite. The cohesive element approach requires the bond to be compliant and have some amount of ductility. There is much debate in the literature about which approach is correct, the cohesive element method or the classical impulsive method. In general, neither is "perfectly correct", as both are engineering representations to complex physical phenomenon.

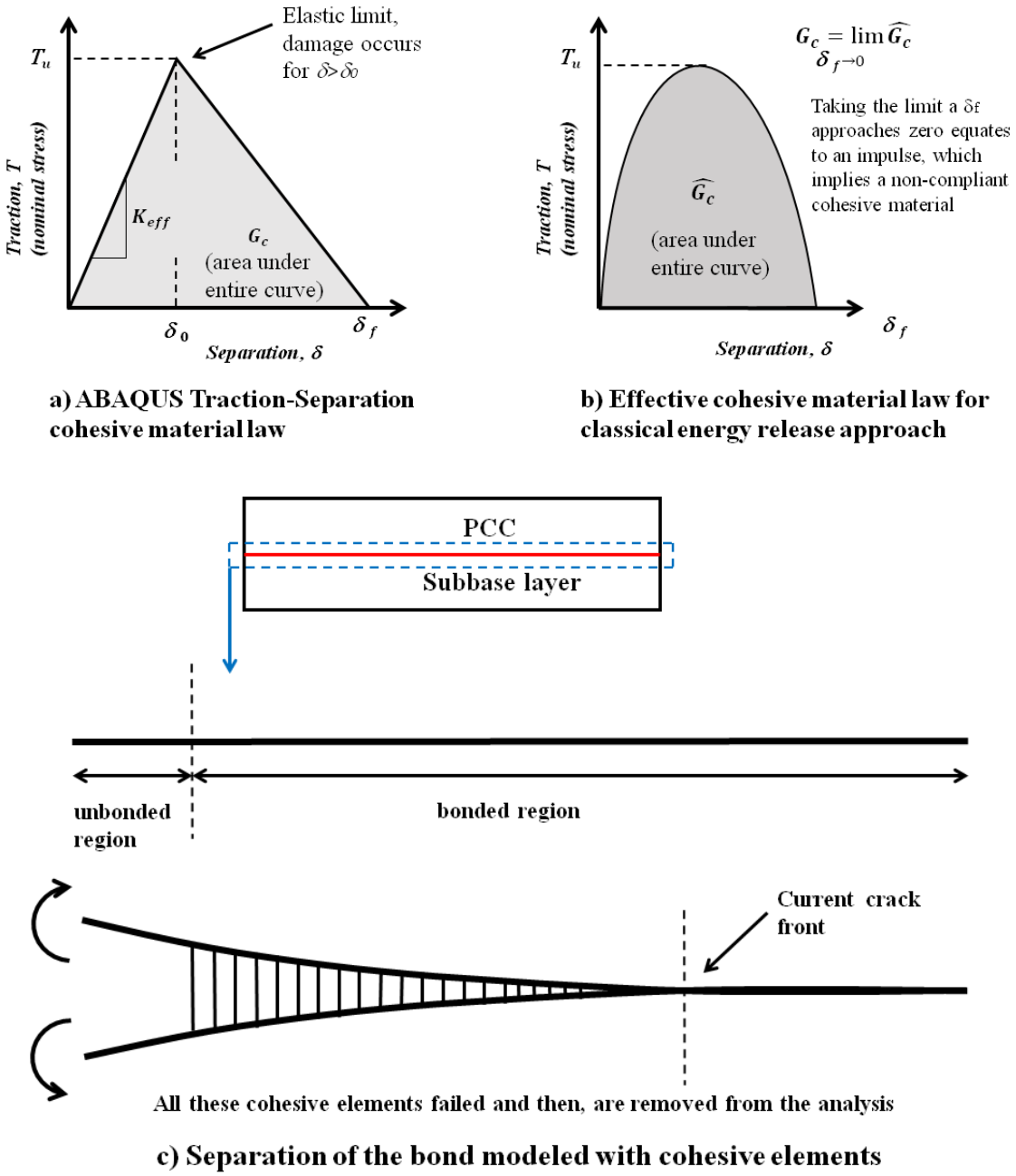

Figure 5-8. Two-dimensional scheme of modeling with cohesive elements under pure mode I loading.

In Figure 5-8, the area highlighted in red represents the area corresponding to the cohesive elements. As discussed above, one can obtain the mixed mode fracture energy

of the bonds using laboratory specimens (like BSCB specimen introduced in section 4) and then use those values as the input of the finite element simulation. The finite element software ABAQUS [152] has the option of changing fracture energy envelope given in Eq. (3.28) by changing the parameters *p* and *q* (see section 3 for more details). The effect of parameters *p* and *q* on the predictions of the slab's displacements, provided by the three-dimensional simulations, will be investigated in section 6 of this dissertation.

5.4.3. Boundary conditions

The boundary conditions used for the simulation of the CRCP structures is illustrated in Figure 5-9.

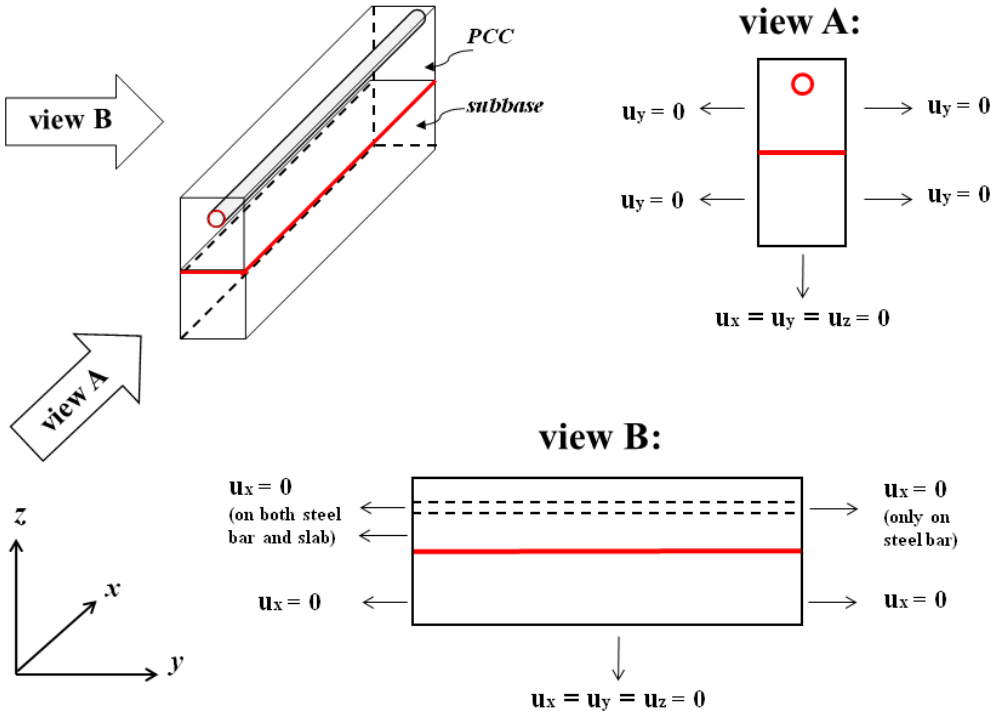

Figure 5-9. Boundary conditions used for 3D finite element simulation of the CRCP.

The length of the prism is half of the actual slab's length and then, the boundary conditions is symmetric with respect to the *x* and *y* axes. The restrictions on *x* and *y* directions are shown in view B and view A, respectively. It is also seen according to view B that the reinforcing steel bar is restricted in *x* direction at the slab's joint. However, the reinforcing steel bar has the freedom to slide in the concrete as a result of environmental loads. There is no restriction on the area covered by the cohesive zone elements. Finite element simulations shows any boundary conditions on the cohesive zone with result in a significant increase of run time, at therefore, it is highly recommended not to restrict the cohesive layer in any direction. It is worth mentioning that Figure 5-9 illustrates a general boundary conditions which can be employed for any rigid pavement structure.

5.4.4. Environmental loading

Time dependent deformation of concrete consists of (1) stress dependent strain and (2) stress-independent strain. Stress dependent strain, ε_i^{σ}, which is produced by stresses in the concrete, is the sum of the elastic strain, ε_i^{e}, and the creep strain, ε_i^{c}. On the other hand, the stress-independent strain, ε_i^{0}, which is not related to stresses , is the sum of the thermal strain, ε_i^{th},and the shrinkage strain, ε_i^{sh}. Therefore, total strain during time step $\Delta t_r (= t_r - t_{r-1})$ is as follows [3, 153].

$$\Delta\varepsilon_i^{Tot} = \Delta\varepsilon_i^{\sigma} + \Delta\varepsilon_i^{0} = \Delta\varepsilon_i^{e} + \Delta\varepsilon_i^{c} + \Delta\varepsilon_i^{th} + \Delta\varepsilon_i^{sh} \tag{5.31}$$

where $\Delta\varepsilon_i^{Tot}$ is the total strain increment; $\Delta\varepsilon_i^{e}$ is the elastic strain increment; $\Delta\varepsilon_i^{c}$ is the creep strain increment; $\Delta\varepsilon_i^{th}$ is the thermal strain increment; $\Delta\varepsilon_i^{sh}$ is the shrinkage strain increment.

If there is no external loading and the environmental loads such as changes in temperature and moisture are the only loads, the stress independent strain will be the only stain developed. However, the pavement structure is always subjected to restrains and as a result the stress dependent strains always develops. The stress independent strain is independent of the slab's boundary conditions and can be measured separately. In other words, if the stress independent strain at a given location of the concrete pavement is known and the total strain of the pavement at the same location is measured, the actual elastic stress of that location will be the strain difference between the stress independent strain and total strains multiplied by the elastic modulus of the concrete at the time of measurement.

Figure 5-10 shows a typical variation of the concrete strains versus time, measured by Nam [3]. The thermal strain and shrinkage strain are changed as the concrete slab cures as a result of change in temperature and moisture gradient throughout the concrete slab. The thermal strain changes in a cyclic manner during daytime with negligible residual strain. The shrinkage strain also changes during daytime, but, with a residual strain at the end of each day. Therefore, the total strain (which includes the stress dependent strains) changes in a cyclic manner with some residual strain per day.

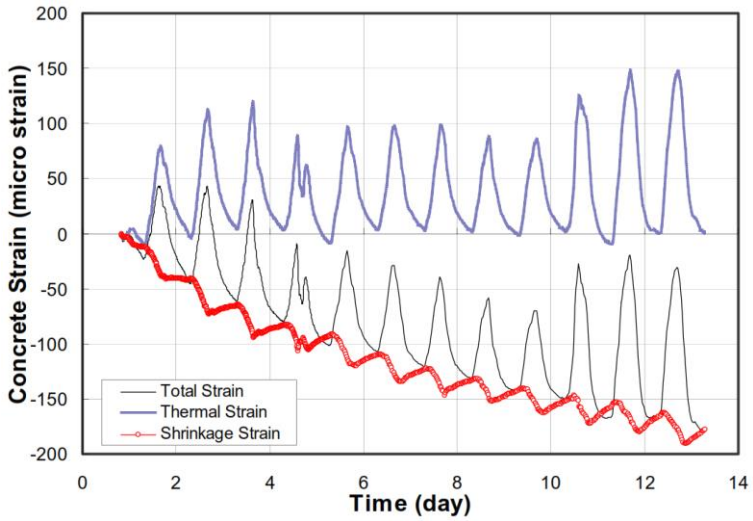

Figure 5-10. Variation of the strains in a concrete slab versus time.

Thermal and shrinkage strains cause in concrete pavement as a result of temperature and moisture gradients, respectively. The temperature profile through the thickness of the slab is nonlinear and causes curling of the slab edges. Although, an equal linear temperature profile is suggested in the literature reducing efforts of dealing with nonlinear temperature profile [14], neglecting the nonlinearity effects sometimes may cause significant errors in prediction of the displacements induced by the temperature. In the current research, however, the three-dimensional finite element approach is capable of simulating of the concrete displacements subjected to any nonlinear temperature gradient.

The 3D finite element equation solver allows the initialization of the model to any state of deformation and stresses that may simulate a built-in lift-off as found in a freshly cured slab. This is done by specifying an equivalent initial thermal and moisture gradient profiles through the slab thickness and running the model in a dynamic

relaxation mode that builds up the static stresses and displacements at the specified parts of the model. After full dynamic relaxation, the model becomes deformed and loaded with stresses that simulate the state of residual stresses in a freshly cured concrete pavement. A data file containing the distorted model becomes the starting file to which any magnitudes and configurations of the environmental loading are applied prior to its reprocessing in a static or dynamic mode as illustrated by the flow chart in Figure 5-11. In other words, the three-dimensional finite element simulation is performed at different time steps to represent time dependent displacements in the concrete slab during a specific period of time.

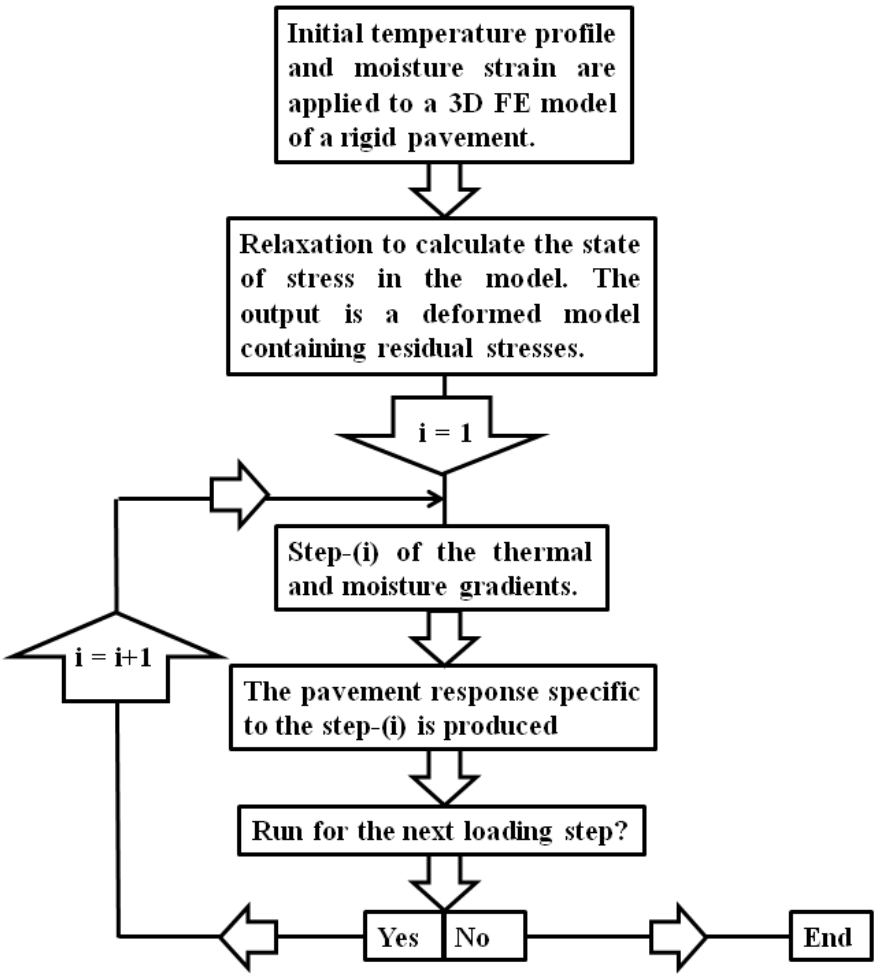

Figure 5-11. Suggested 3D finite element simulation procedures.

5.5. Prediction of the test data

A literature survey shows that the available experimental data reported for the end movements of concrete slabs due to the environmental loading profile is very limited. This part, deals with the prediction of the experimental test data on the slab's lift-off presented by Jeong and Zollinger [154] using the three-dimensional finite element procedure explained above.

5.5.1. Experiments

Jeong and Zollinger [154] constructed a concrete slab at Texas A&M University to investigate environmental effects in terms of temperature and moisture effects on the behavior of jointed plain concrete pavements (JPCP). They measured the temperature and moisture profile throughout the concrete slab and measured the associated strain fields. They used the equivalent temperature profile proposed by Mohamed and Hansen [14] to simplify calculating of the thermal stresses. Figure 5-12 illustrates the layout of the slab instrumentation as well as the geometry of the JPCP made by them. The mixture properties of the concrete and the detailed construction procedure is explained in [154]. Dowel bars with 45.7 cm (18 inch) length and 3.1 cm (1.25 inch) diameter were installed mid-slab of the pavement where a sawcut joint was placed. The dowel bars were placed at a spacing of 30.5 cm (12 inch).

They collected temperature and moisture data over two years after construction of the slab to analyze the effect of climatic factors on the temperature and moisture movement within the slab. Figure 5-13 shows variations in temperature and relative humidity over first seven days at three locations: bottom of the slab, top of the slab, and the ambient.

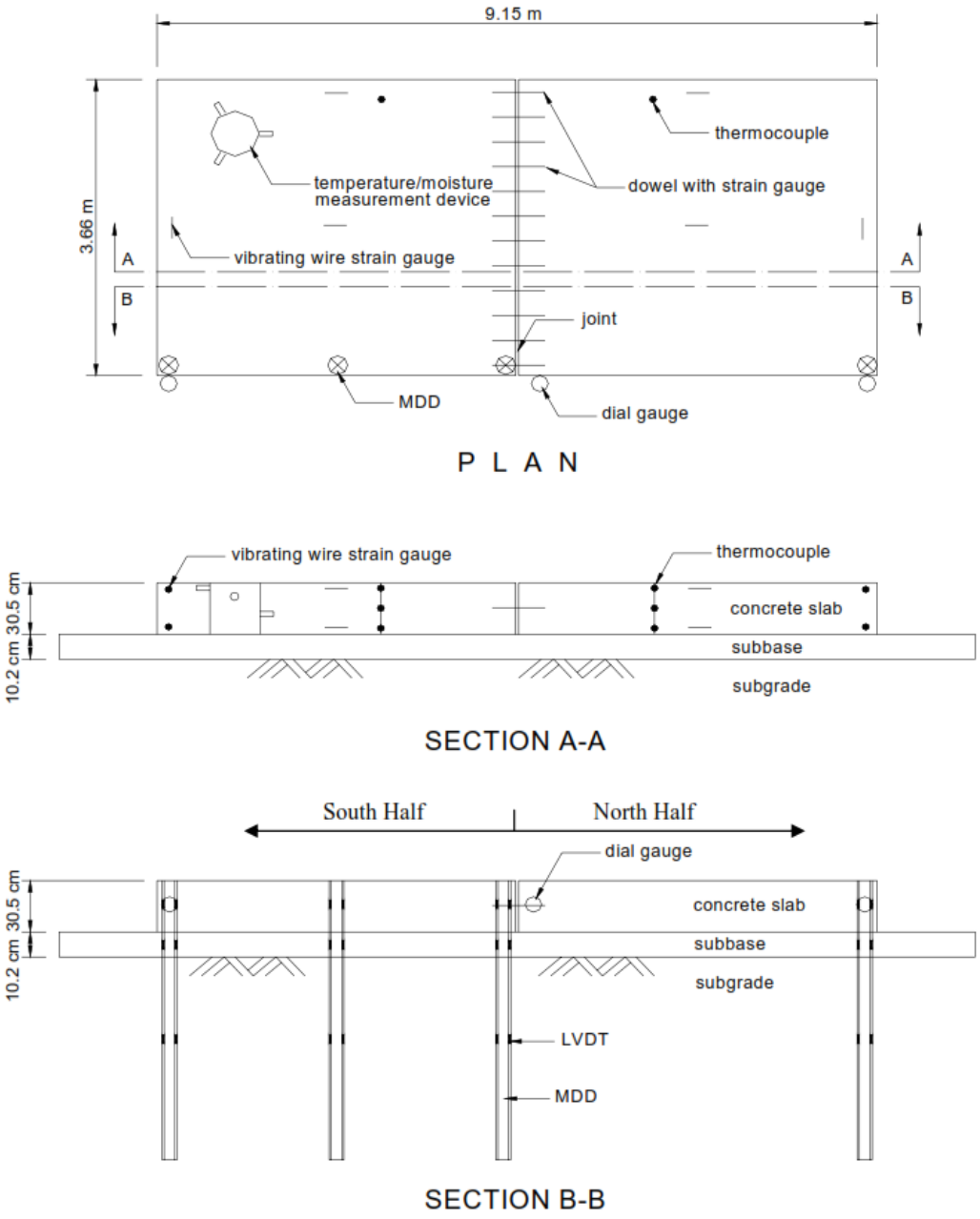

Figure 5-12. Layout of the instrumentation and the geometry of the JPCP made by Jeong and Zollinger [154].

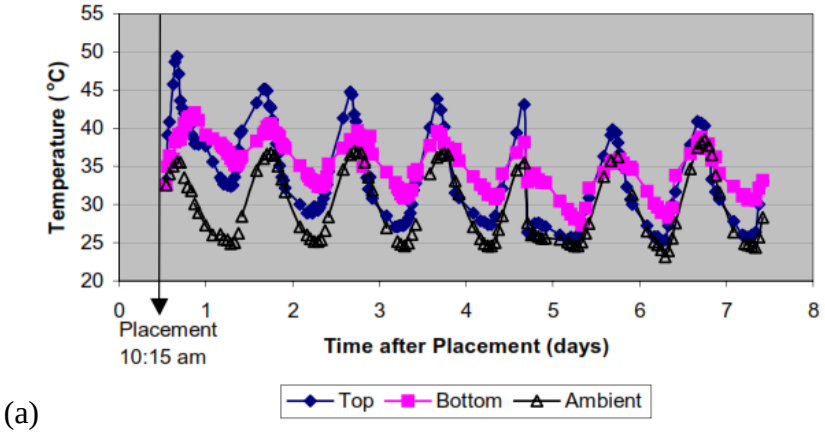

(a)

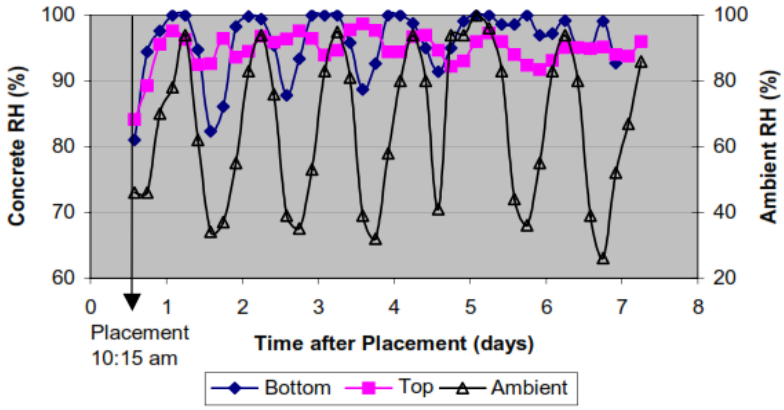

(b)

Figure 5-13. Temperature and relative humidity at top and bottom of slab over initial 7 days: (a) temperature; (b) relative humidity [154].

The stress-independent strains were calculated using Eq. (5.32), and Eq. (5.33) for thermal and shrinkage strains, respectively.

$$\varepsilon^{th} = \alpha.\Delta T(z) \tag{5.32}$$

$$\varepsilon^{sh} = -\varepsilon_{\infty}.\left(1-\left[\frac{RH(z)}{100}\right]\right)^{3} \tag{5.33}$$

where ε_{∞} was measured as 524μ.

Figure 5-14 shows the lift-off at the top of the slab reported by Jeong and Zollinger [154] at three different locations. However, the vertical displacement in the prism taken out for the finite element simulation, shown in Figure 5-7, should be compared to the vertical displacement reported for the joint. The vertical displacement at the corner can also be simulated by slightly change in the boundary conditions shown in Figure 5-9.

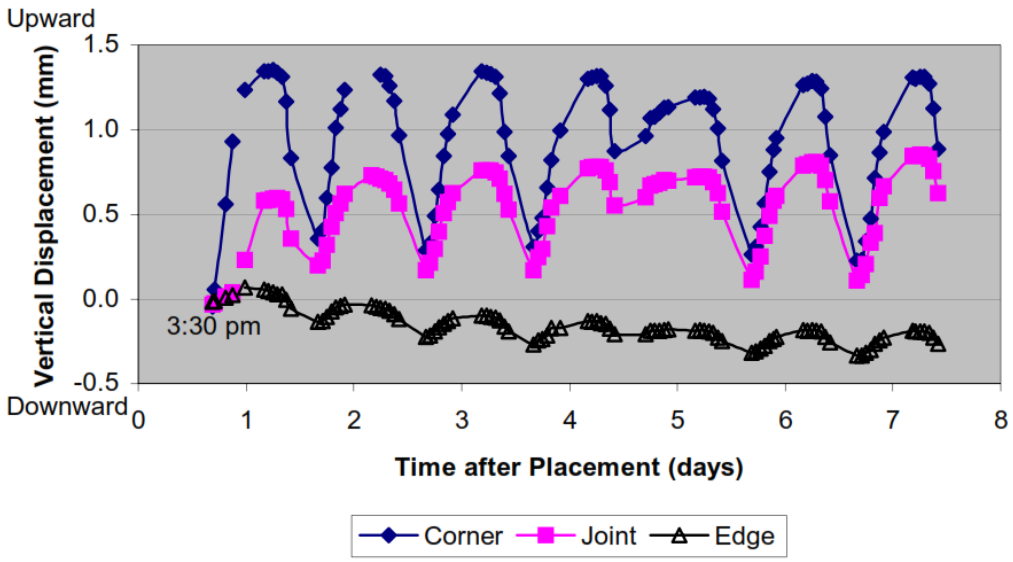

Figure 5-14. Vertical displacements of slab over Initial 7 days at each position [154].

5.5.2. Material properties and geometry

The elastic and thermal properties of the concrete slab, dowel bar, and subbase layer are listed in Table 5-2. Experimental observation shows that some amount of cement transfers from the fresh concrete slab into the subbase material. Therefore, the bond between the concrete slab and the subbase layer breaks somewhere in the subbase

material. Such observation leads to this conclusion that one can assume that the bond strength between the concrete slab and the subbase layer can be considered same as the ultimate tensile strength of the subbase layer.

Table 5-2. Material properties used for the JPCP constructed by Jeong and Zollinger [154].

Material	Property	Value
Concrete		
	Density (Kg/m3)	2400
	Compressive strength (MPa)	19.1
	Tensile strength (MPa)	2.89
	Modulus of elasticity (MPa)	34000
	Poisson's ratio	0.2
	Coefficient of thermal expansion (/^{o}C)	11.3×10^{-6}
Subbase		
	Density (Kg/m3)	2100
	Modulus of elasticity (MPa)	3500
	Poisson's ratio	0.2
	Compressive strength (MPa)	1.2
	Tensile strength (MPa)	0.11
Steel		
	Density (Kg/m3)	7830
	Modulus of elasticity (MPa)	210000
	Poisson's ratio	0.3
	Coefficient of thermal expansion (/^{o}C)	10.8×10^{-6}

It is assumed the elastic properties and the bond strength of the cohesive layer between the concrete slab and the subbase equates the elastic properties and the tensile strength of the subbase material. In order to use damage evolution method of the traction separation law, the failure parameters were assumed $p = q = 2.1$ (see Eq. (3.28)). In fact, this value for p and q was obtained after several simulations with different values and obtaining the best value to fit with the test data. The fracture toughness G_{Ic}, and G_{IIc},

were also measured as: $G_{Ic} = G_{IIc} = \frac{\pi.\sigma_{T,C}.C_0}{2E_{sub}}$, where $\sigma_{T,C}$ and E_{sub} are the tensile strength and modulus of elasticity of subbase material, respectively, and C_0 equates the size of the voids (≈ 0.4mm). The effect of each parameter on the slab's displacements is comprehensively studied in section 6 of this dissertation. Since dowel bars in JPCP are not fully bonded to the concrete material (even they are lubricated in some cases), the contact behavior between the dowel bar and the concrete slab was assumed as a frictional contact with the coefficient of friction of μ = 0.05, as recommended in the literature [155].The slab weight was activated to include the body force that may influence the magnitude of deflection and stress due to curling, especially under slab/subbase separation conditions.

Figure 5-15, illustrates the geometry of the model used for the three-dimensional finite element simulation. In JPC pavements, concrete slabs are connected together using dowel bars and the geometry of all concrete slab segments are same. That means one can simulate only one segment in order to study displacements in JPCP. On the other hand, one can take out a prism form middle of the concrete slab and run the simulation on the prism instead of simulation the whole slab. This geometrical simplification significantly reduces the run time. The width of the prism is equal to the spacing distance of the dowel bars. Figure 5-15 also shows the connection between two concrete slabs using dowel bars. The space between the two concrete slabs shown in this figure is the size of a crack, which can be assumed zero in comparison to the order of dimensions used for the current simulation.

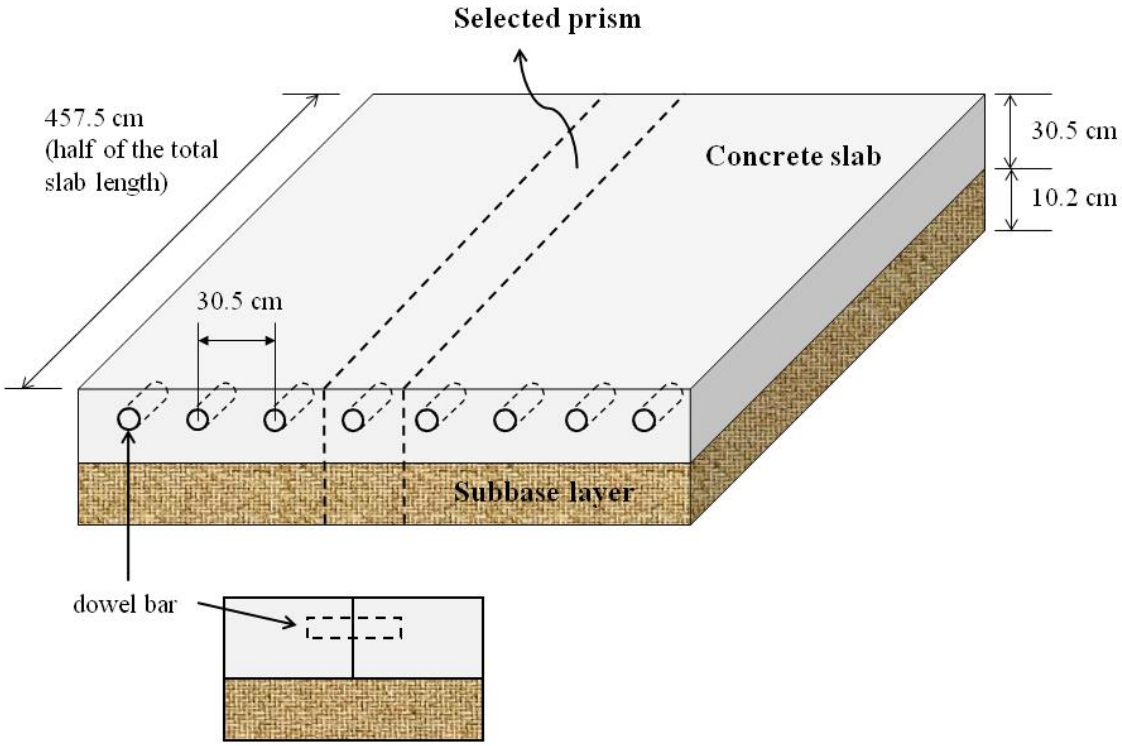

Figure 5-15. Geometry of the model and the selected prism used for the three-dimensional finite element simulation of JPCP constructed by Jeong and Zollinger [154].

5.5.3. Loading profiles

As shown in Figure 5-14, the concrete slab moves vertically during daytime as a result of change in temperature and the moisture gradients. For the current study, the slab end movements during sixth day of the placement is simulated. Figure 5-16 a, and b, illustrate variation of the temperature and moisture during sixth day through the slab thickness at two points: top and the bottom. Because of the lack of enough test data through the slab thickness, a linear profile is assumed for both temperature and moisture gradients from top to the bottom of the concrete slab.

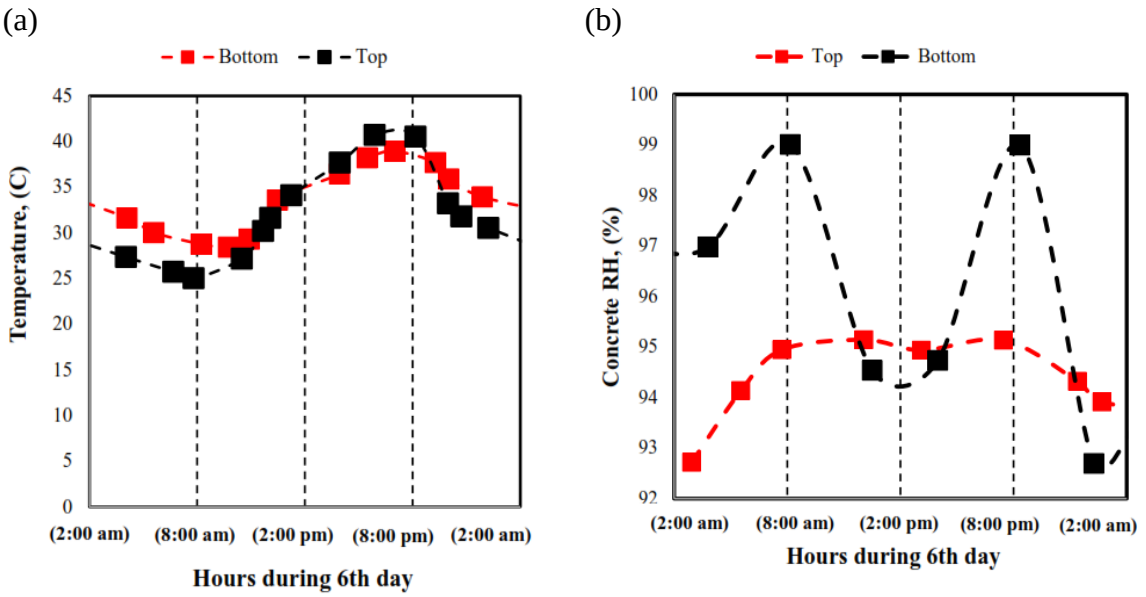

Figure 5-16. Temperature and relative humidity at top and bottom of slab over 6th day: (a) temperature; (b) relative humidity.

Since both concrete and the dowel bar are modeled as thermo-elastic materials, the temperature profile is directly given to the finite element simulation as an input to allow the whole structure relax during each time step. The moisture strain corresponding to each time step was also calculated using the Eq. (5.33) and then given to the finite element simulation as the input. Four steps plus an initial step were considered for the finite element simulations as: initial step (the initial temperature and moisture strain are applied to create the initial displacements before starting the sixth day), step-1 (to simulate displacements associated from 2:00 am to 8:00 am), step-2 (from 8:00 am to 2:00 pm), step-3 (from 2:00 pm to 8:00 pm) and step-4 (from 8:00 pm to 2:00 am). In addition to the temperature and moisture induced strains, the slab weight was also modelled as a body force throughout the concrete slab.

5.5.4. Meshing and element types

The prism, which consists of cement concrete, subbase, dowel bar, and the cohesive layer, were modeled using very fine mesh, as shown in Figure 5-17. The fine meshing allows realistic modeling of circular dowel bars using eight-node solid brick elements, permits the application of any form of thermal gradient and shrinkage strain through the slab thickness, and facilitates the numerical solution.

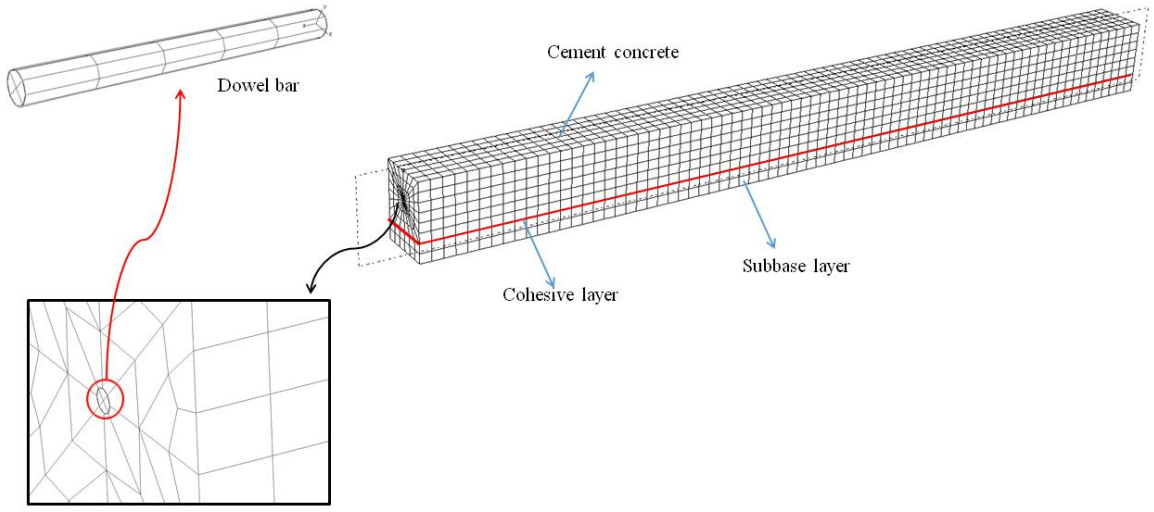

Figure 5-17. Mesh pattern used for the three-dimensional finite element simulation of the CRC prism.

The 3D modeling of the dowel bars using fine mesh is essential in order to account for the mechanism of dowel contact and the associated states of stress that develop around the dowels for different temperature profiles and moisture strains. Sliding interfaces with frictional contact were assumed between the dowel bar and the surrounding concrete, with the coefficient of friction of $\mu = 0.05$ (as suggested in [155]).

If the dowel bar does not suffer bending deformation due to external loading or temperature gradient, the concrete prism can contract freely without interference with the dowels. However, if the slab curls, the dowel-concrete interface would allow non-uniform and partial contact along the interface of the dowel at any angular position that depends on the dowel position along the transverse joint. A 3D stress element (C3D8R), was used to simulate cement concrete, subbase, and the dowel bar and a 3D cohesive element (COH3D8), which is an eight node three dimensional cohesive element, is employed to simulate the cohesive layer between the concrete and the subbase layer. Since five steps were simulated together, it was hard to achieve complete solution for all steps together. In order to achieve full solution including all steps, the number of elements used for each part were changed many times.

5.5.5. Simulation results

Figure 5-18 shows mesh pattern of the 3D deformed prism as well as close up views for sliding of dowel bars and the crack propagation through the interface of concrete and the subbase layers during the first step. Dowel bar slides through the concrete and moves out as the concrete curls upward. The cohesive elements break once they meet critical mixed mode fracture energy and as a result, the cohesive crack propagates through the interface of the concrete and the subbase layer. Finally, the interface crack stops propagating when the environmental loads (which lead to lift concrete slab upwards) reaches to an equilibrium with the slab weight. A more informative view of the displacements is depicted in Figure 5-19. In this figure, the mid

plane of the model is taken out in order to show displacements at the middle of the model in a better manner. The relative displacement between the concrete slab and the dowel bar is better illustrated in this figure. In order to diminish effects of boundary conditions on the simulation results, two points A, and B, at the mid plane are selected to track displacements at the top and bottom of the concrete slab.

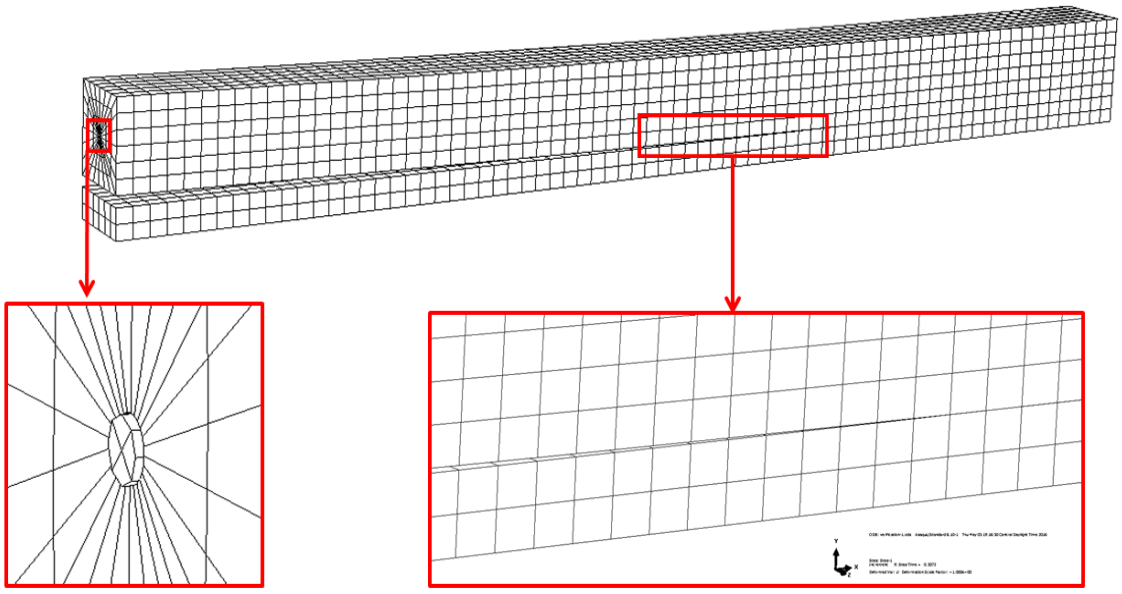

Figure 5-18. Mesh pattern for the deformed JPCP prism with close up for sliding of dowel bar as well as cohesive crack propagation through concrete/ subbase interface.

Figure 5-20 shows the vertical displacement of the concrete slab at point A, at different time steps. Three curves exist: test data form Jeong and Zollinger [154], simulation results for p=q=1, and the simulation results for p=q=2.1. The simulation results corresponding to p=q=1 assumes a linear relationship in traction separation law, and can be seen, it does not represent the concrete/ subbase bond behavior in a proper

manner. After several simulations with different values of p and q, it was found $p=q=2.1$ (which presents a nonlinear failure envelope) provides best fit for the tests results. This finding is in agreement with the literature which suggest $2.0 < p, q < 2.5$ for most interfacial bonded joints in engineering applications [60 – 62]. The effect of parameters p and q on the displacements in CRCP structures is studied in section 6 of this dissertation. It can also be seen from Figure 5-20 that there is a good agreement between the test data and the simulation predictions at the first steps, however, the prediction error increases for next steps. This may happen because of this fact that the error at higher steps is accumulated since each step starts with the initial conditions calculated at the end of the previous step. Other factors causing error are: assuming linear profile for temperature and moisture gradient through the slab thickness (because of lack of available test data), and large increments (every six hours).

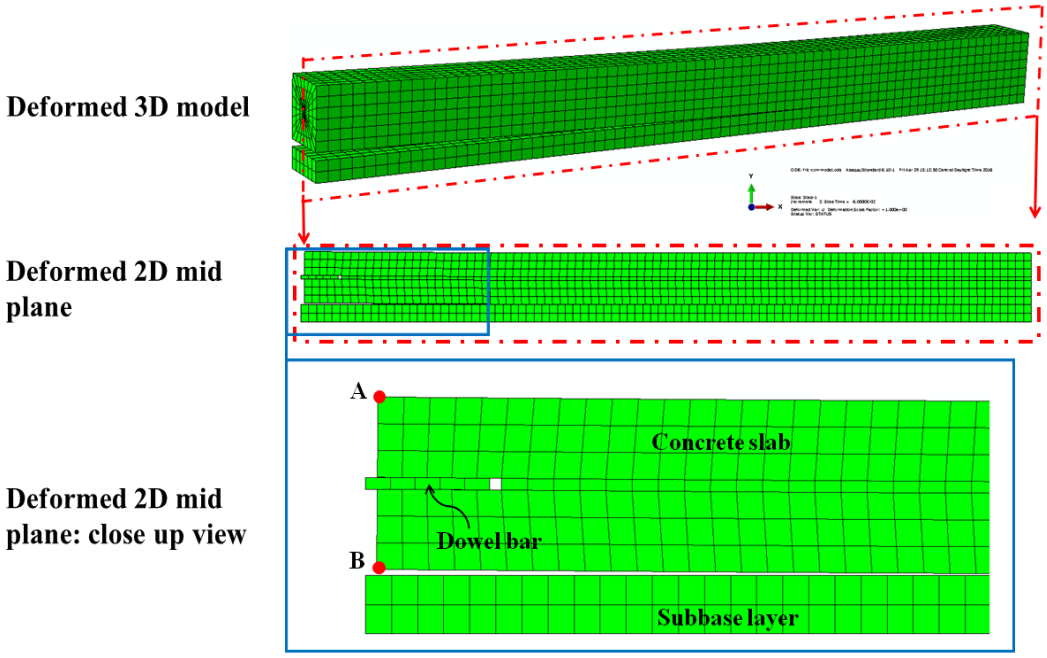

Figure 5-19. Mesh pattern for the deformed JPCP prism: deformed 3D model, deformed mid plane, close up view of deformed mid plane.

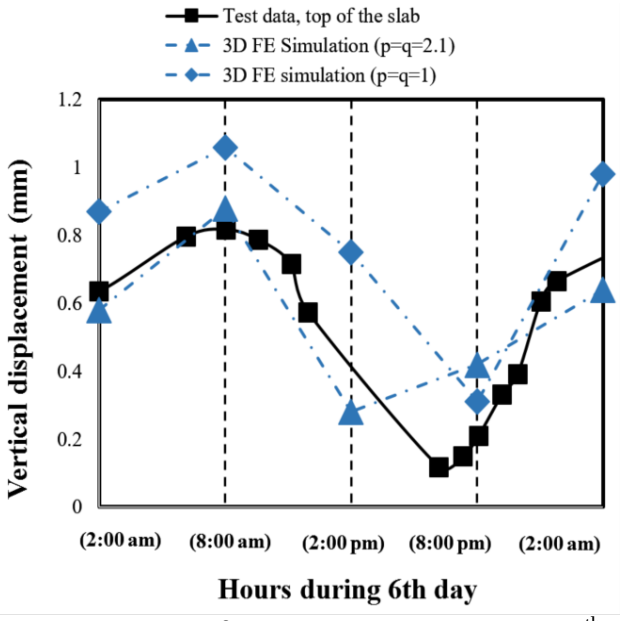

Figure 5-20. Vertical displacement of the concrete slab during 6th day: test data, finite element simulation with linear cohesive failure criterion, and finite element simulation with nonlinear cohesive failure criterion.

As mentioned before, the available test data for validation of the numerical procedure explained in this section is very limited. Jeong and Zollinger [154] reported the displacements for the vertical direction but, not for the horizontal direction. However, it was interesting to see the simulation results for the prediction of the horizontal end movements. The horizontal displacements at points A and B of the concrete slab (see Figure 5-19) is illustrated in Figure 5-21. It is seen that the end movement at the top of the slab is larger than the bottom of the slab. This is reasonable since the bottom of the slab is restricted by the cohesive layer while the top surface is free to move and therefore, the slab edge (segment AB) tends to rotate clockwise as a result of environmental loads.

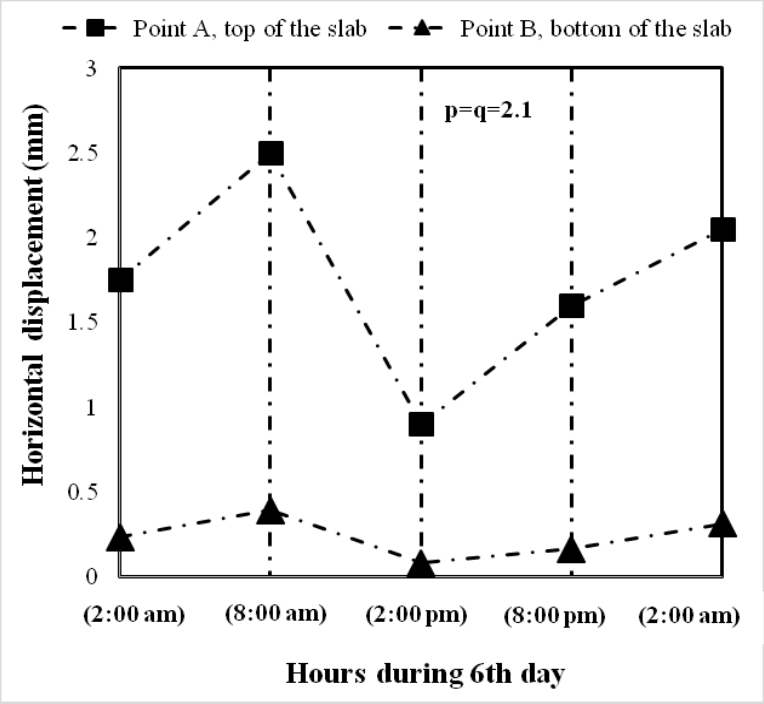

Figure 5-21. Horizontal displacement of the concrete slab during 6th day: at the point A (top), and at the point B (bottom).

5.6. Summary and conclusions

Both analytical and numerical models for evaluation of the end movements in concrete slabs were studied. First, Palmer's model was introduced as a pioneering work which presents a one dimensional solution for displacement field in CRC pavements. A modified version of the Palmer's model was then presented in a two dimensional framework considering effects of slab lift-off on the horizontal displacement of the CRC pavements. The bond strength modeling between concrete slab and the subbase layer was also improved in modified Palmer's model by considering the effect of crack propagation mechanism at the interface of the concrete slab and the subbase layer. The modified Palmer model was then compared to the results obtained from two-dimensional finite element simulation of a concrete slab subjected to a typical environmental loading configuration. It was found that there is an agreement between the predictions provided by the modified Palmer's model and those of obtained from two-dimensional finite element simulation results.

Like other closed form solutions, both Palmer and the modified palmer are developed based on some assumptions which sometimes may lead significant errors. In order to present a more realistic model, a three dimensional finite element approach was suggested which was able to simulate CRCP at different load steps. The model uses a zero thickness cohesive layers at concrete/ subbase and concrete/ steel bar interfaces. The failure properties of the cohesive layer are directly related to the bond strength which can be characterized by the fracture test of the laboratory specimens (like BSCB, see section 4 of this dissertation). The suggested three dimensional finite element

approach was then utilized to predict displacements in a JPCP structure tested by the previous researchers. It was found that the three dimensional finite element model is capable of predicting the experimental data in an acceptable range of error.

6. EFFECT OF DIFFERENT FACTORS ON THE END MOVEMENTS IN CRC PAVEMENTS

6.1. Introduction

There are many factors affecting on the end movements in CRC pavements. Among them, slab dimensions, environmental loads (temperature and moisture gradients), and slab modulus are well investigated by researchers in the past decades using either analytical models or special-purpose programs. This section studies effect of these parameters on the end movement in CRC pavements using 3D finite element approach introduced in section 5. In addition, the effect of bond strength between the concrete slab and subbase layer, as well as the effect of subbase modulus are included which have not been considered in the previous published works. The results of the current research provide researchers with insight as to the effect of different design parameters in CRC pavements and answer some of the primary questions on the mechanism of end displacements in concrete slab/ subgrade structures due to the environmental loads.

6.2. Finite element modeling

The 3D finite element model, developed in section 5, is used herein for study of the different factors on the end movements in CRC pavements. The geometry and the boundary conditions used for the simulation are shown in Figure 5-7, and Figure 5-9, respectively (see section 5). Figure 6-1, illustrates deformation of the prism shown in

Figure 5-7, subjected to a typical environmental load. The deformed shape of the mid plane is also depicted to show bond slip between the reinforcing steel bar and the concrete.

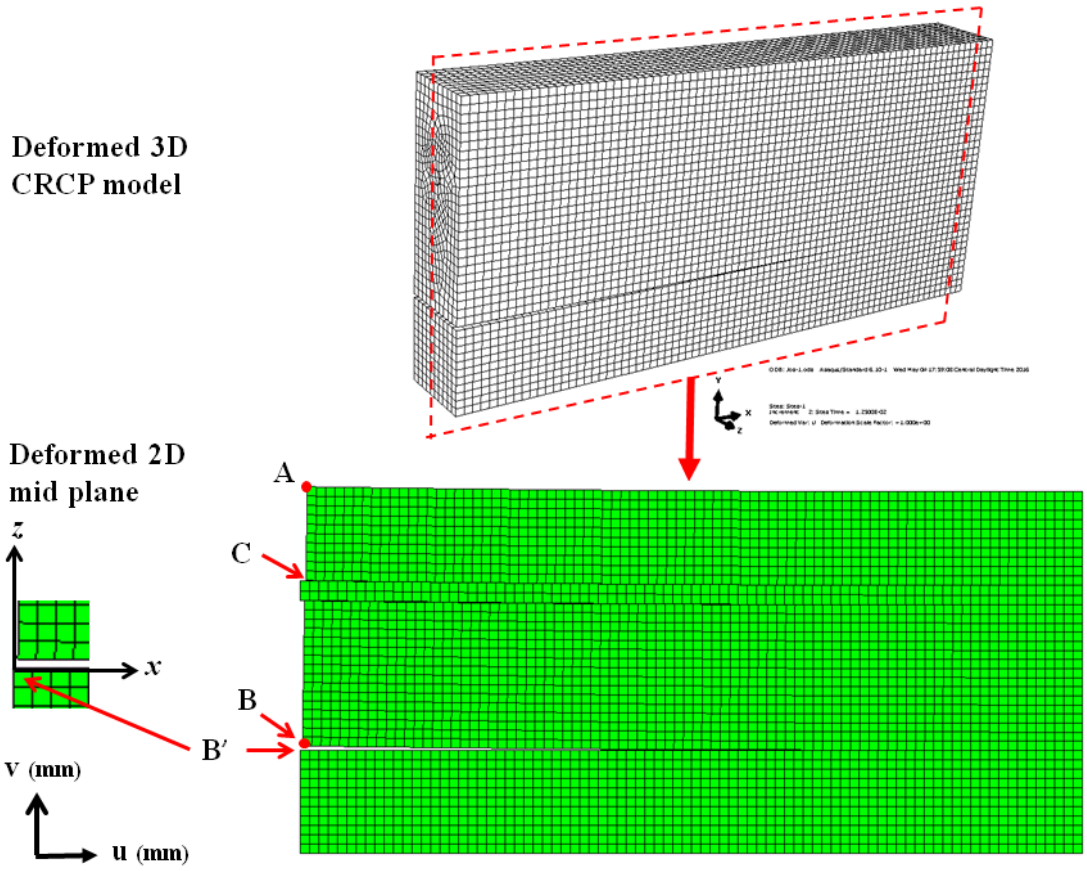

Figure 6-1. Mesh pattern for deformed CRCP, as well as the deformed mid plane.

Vertical and horizontal displacements are tracked at three points: A) top of the slab, B) bottom of the slab, and C) on the concrete part, at the interface of reinforcing steel bar and concrete slab. Since the reinforcing steel bar is restricted at its end, the horizontal displacement at point C roughly represent bond slip between the concrete and

the reinforcing steel bar. The bond strength between the concrete slab and the reinforcing bar is assumed to be a constant value of τ_b = 5MPa [156, 157], and steel bar #6 (d_s = 0.75in = 1.905cm) was used for all simulations. The zero thickness cohesive zone models are utilized for simulation of the reinforcing steel bar/ concrete, and concrete slab/ subbase interfaces.

6.3. Effects of geometry

The geometry of the CRCP used for the finite element modeling is illustrated in Figure 5-7 (see section 5). It is expected that all dimensions shown in Figure 5-7 influence on the slab displacements. In the following, the effects of slab length (L), relative slab thickness (t_0 / t_{base}), and the location of the reinforcing steel bar (Z_0), on the displacements at points A, B and C shown in Figure 6-1, are explored. Table 6-1 lists dimensions used for the finite element simulation. The slab thickness and width are considered as fixed values of t_0 = 25cm, and b = 10.8cm, respectively. It should be mentioned that L equals to the half of the actual slab length.

Table 6-1. Dimensions used for modeling of CRCP.

t_{base} (cm)	L (cm)	Z_0 (cm)
2.5, 5, 7.5, 10	45.7, 76, 137	13.75, 15, 16.25

The materials properties of concrete slab, subbase layer, and the reinforcing steel bar were assumed to be same as listed in Table 5-2 (see section 5). The interface between concrete slab and subbase layer were modelled using cohesive elements following traction separation law with failure parameters of $p = q = 2$ (see section 5 and

Eq. (3.28) in section 3 for more details). A one-step constant linear loading configuration through slab thickness is assumed for the environmental loads as $\Delta T = T_{bottom} - T_{top} = +10^oC$, and $\Delta RH = 10\%$. In addition to the temperature difference, a constant temperature profile of $T = +10^oC$ is also given as an input to the model. The linear strain profile induced by moisture gradient was then obtained using Eq. (5.33). The slab weight was modelled as a body force throughout the slab in which the density of concrete slab and the reinforcing steel bar were assumed 2400Kg/m^3, and 2100 Kg/m^3, respectively. This loading profiles are also used to study effect of modulus of elasticity, and the bond strength on the end movement in CRCP (sections 6.4 and 6.5).

Figure 6-2 (a) and (b) show variation of displacements at points A, B, and C versus normalized slab length (L/b), in horizontal and vertical directions. In Figure 6-2, other dimensions are fixed as Z_0 = 15cm, and t_{base} = 5cm. As seen from Figure 6-2 (a), the horizontal end movement increases as the slab length increases. This observation can be explained easily because the more slab length the more shrinkage in a same shrinkage strain profile. For vertical displacement, except for the point B which is affected by the interface, it can be seen that the slab lift-off increases as the slab length increases until a critical slab length is achieved. After the critical slab length, the slab tends to move downward due to the slab weight. However, the variation of the vertical displacement versus slab length is negligible. In the present model, the concrete slab is bonded to the subbase layer. Indeed, the effect of slab length on the vertical displacement must be more significant for lower bond strength or ultimately if the concrete slab be placed on a frictionless surface.

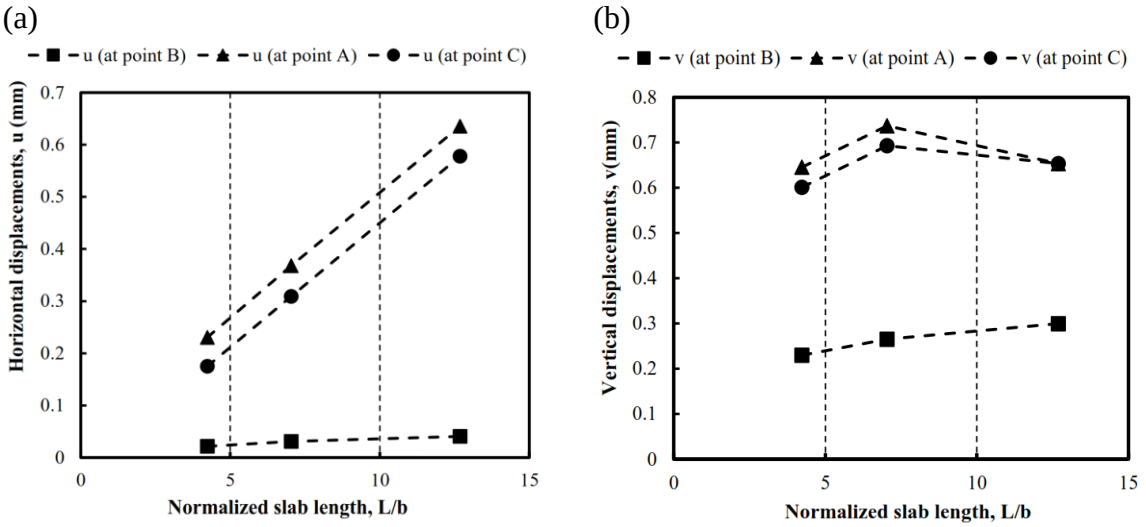

Figure 6-2.Variation of displacements at the slab edge versus normalized slab length: (a) horizontal displacement, (b) vertical displacement. Z_0 = 15cm, and t_{base} = 5cm.

The effect of location of the reinforcing steel bar on the end movements is shown if Figure 6-3. Other dimensions are fixed as L = 76cm, and t_{base} = 5cm. In the current model, since the temperature of the concrete slab is assumed to be lower on its top than its bottom (which happens during nighttime), the concrete slab tends to move upward and thus, the upper and lower parts of the slab are under tension and compression, respectively (due to the dead weight of concrete slab). The lower part of the concrete slab is also constrained by the interface bond and therefore, one can decrease slab lift-off by moving the reinforcing steel bar to the upper part of the slab (increasing Z_0), in order to help concrete slab to resist moment induced by environmental loading. Figure 6-3(b) proves this hypothesis as can be seen that the vertical displacement dramatically decreases by increasing Z_0. The effect of location of the reinforcing steel bar on

horizontal end movements is expected to be negligible since changing Z_0 does not make a significant change on the amount of shear stress between the reinforcing streel bar and the concrete slab, as can be seen in Figure 6-3(a). In other words, the location of the reinforcing steel bar controls the vertical displacement by carrying some part of the lift-off moment, but does not influence horizontal end movement significantly.

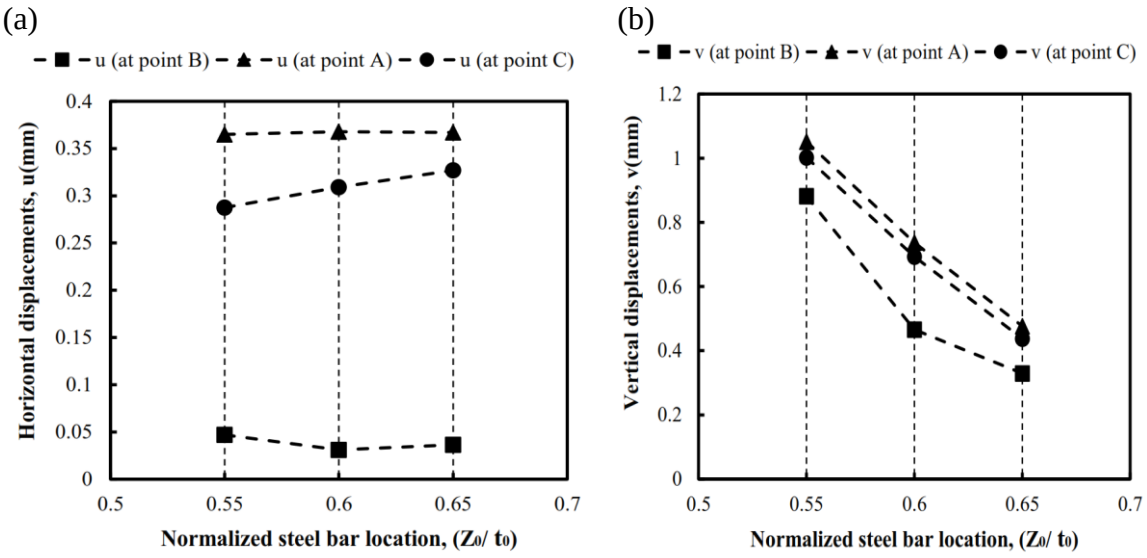

Figure 6-3.Variation of displacements at the slab edge versus normalized reinforcing steel bar location: (a) horizontal displacement, (b) vertical displacement. L = 76cm, and t_b = 5cm.

The simulation results for effect of subbase thickness on the end movement in CRC pavements are illustrated in Figure 6-4. In order to investigate only the effect of subbase thickness, other dimensions are fixed as Z_0 = 15cm, L = 76cm. It can be observed that the displacements at the slab edge do not change considerably when the subbase thickness increases. This observation can easily be explained by the boundary

conditions assumed for the subbase layer, as shown in Figure 5-9 (see section 5). According to Figure 5-9, a considerable role of the subbase thickness on the end movements can be expected when the cohesive bond between the concrete slab and the subbase layer is very strong. However, in many CRCP structures, the bond strength between the concrete slab and the subbase layer is not so strong to deform subbase layer significantly, but rather the interface bond between the concrete slab and the subbase layer fails before deformation occurs in the subbase layer.

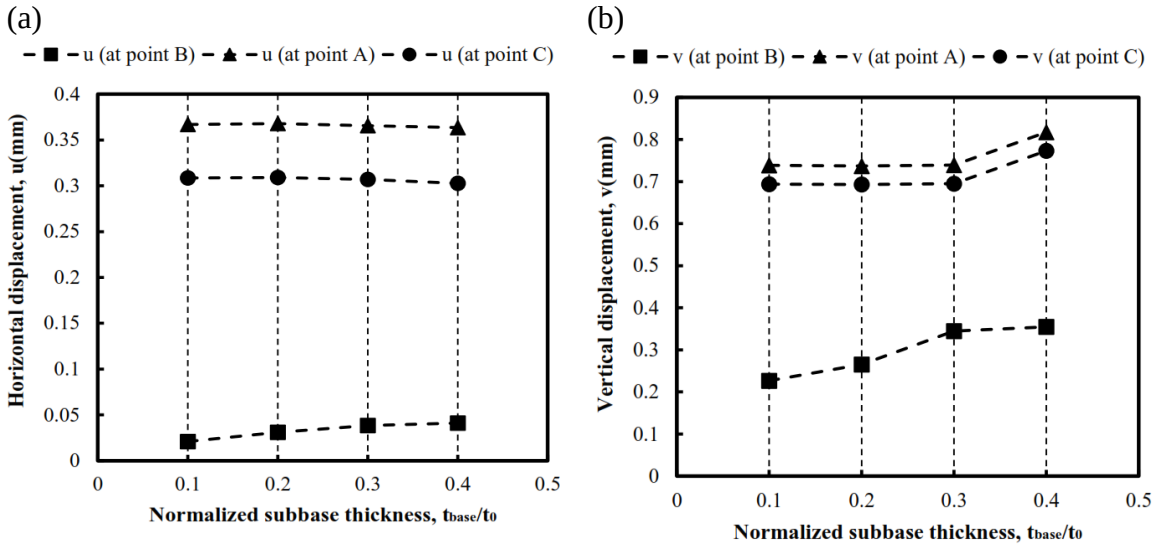

Figure 6-4.Variation of displacements at the slab edge versus normalized subbase thickness: (a) horizontal displacement, (b) vertical displacement. Z_0 = 15cm, L = 76cm.

6.4. Effect of modulus of elasticity

Figure 6-5 shows the effect of subbase modulus on the end movement in a CRCP structure. A fixed dimension is used for the finite element simulation as Z_0 = 15cm, L =

76cm, and t_{base} = 5cm. The simulation results show that modulus of the subbase layer does not have a significant impact on the concrete slab displacement. This behavior can be explained by this fact that the bond strength between the concrete slab and the subbase layer is not strong enough to transfer effects of slab modulus to the concrete slab. In other words, the end movement in concrete slab should be more affected by the bond strength rather than the modulus of the subbase layer. For example, for a very strong bond between the concrete slab and the subbase, the subbase layer has to deform as a result of slab lift-off and therefore, it is expected that the modulus of subbase layer influence on the slab displacements.

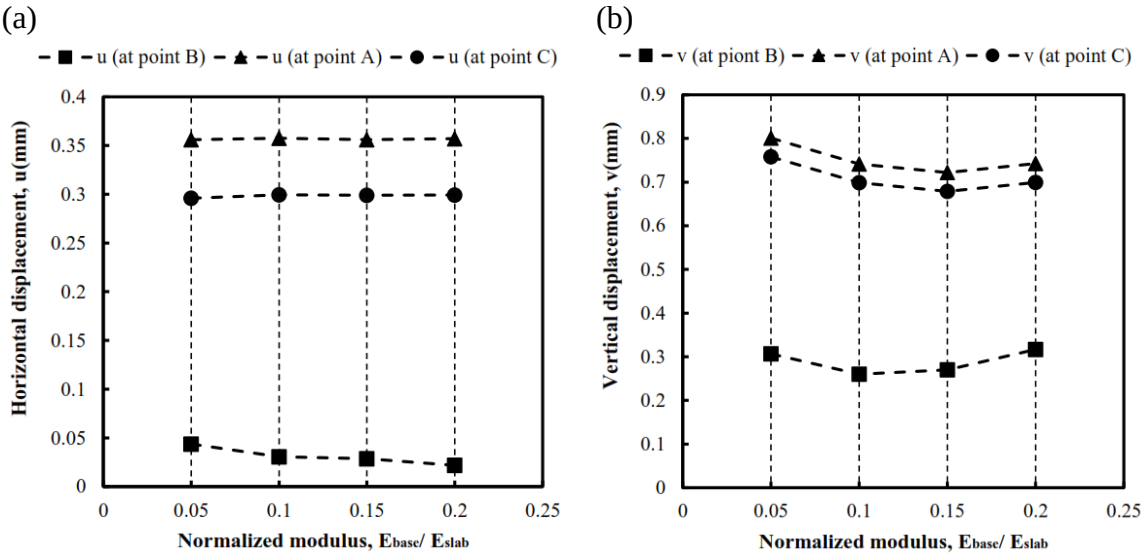

Figure 6-5. Variation of displacements at the slab edge versus normalized subbase modulus: (a) horizontal displacement, (b) vertical displacement. Z_0 = 15cm, L = 76cm, and t_{base} = 5cm.

It is worth mentioning that for exploring effect of modulus of elasticity, it was assumed that the modulus of concrete slab is constant and the modulus of the subbase

layer is changed. This is reasonable since the modulus of elasticity does not vary significantly for concrete in different CRC pavements, however, it alters for the subbase layer depending on the type of the material served as the subbase. Indeed, a significant variation in end movement is anticipated when the modulus of the concrete is changed. This happens because the net environmental strains are applied to the concrete slab and thus, the displacements should increase as the modulus of the concrete decreases.

6.5. Effect of Bond strength between concrete slab and subbase layer

The bond strength between concrete slab and the subbase layer controls separation of the slab from the subbase. It is expected that the higher bond strength, the lower slab lift-off. However, in pavement design, a strong bond strength is not always desirable. In other words, de-bonding of the concrete slab/ subbase layer interface helps to release some energy induced by the environmental loads and prevents concrete slab from early age cracking. Low bond strength, on the other hand, enhances separation in CRC pavements leading to deterioration of slab/ subbase due to interface erosion. That means the bond strength should be considered as an important parameter in designing CRC pavements.

The fracture criterion for weak interfaces can be expressed as a power-law equation explained in section 3, as $\left[\frac{(G_I)_C}{G_{IC}}\right]^p + \left[\frac{(G_{II})_C}{G_{IIC}}\right]^q = 1$, where $(G_I)_C$ and $(G_{II})_C$ are the mode I and mode II components of the strain energy release rate at fracture, G_{IC} and G_{IIC} are the critical fracture energies for pure modes, and p and q are exponents (see

section 3, subsection 3.4. for more details). Figure 6-6 depicts variation of the fracture loci versus parameters p and q ($p = q = 1$). The area surrounded by each curve and the coordinate axes represents the safe zone, and above this area, the interface crack propagates through the interface. It is seen that as the values of p and q decrease the safe zone gets more constricted and the fracture criterion presents more conservative predictions. However, according to the literature, for many of the interface bonds available in different engineering applications, p and q parameters fall within the range of $1.5 < p, q < 2.5$. These parameters are determined for asphalt concrete/ concrete bonds in section 4 of this dissertation. Same method can be applied for any other bonded structures with different material properties.

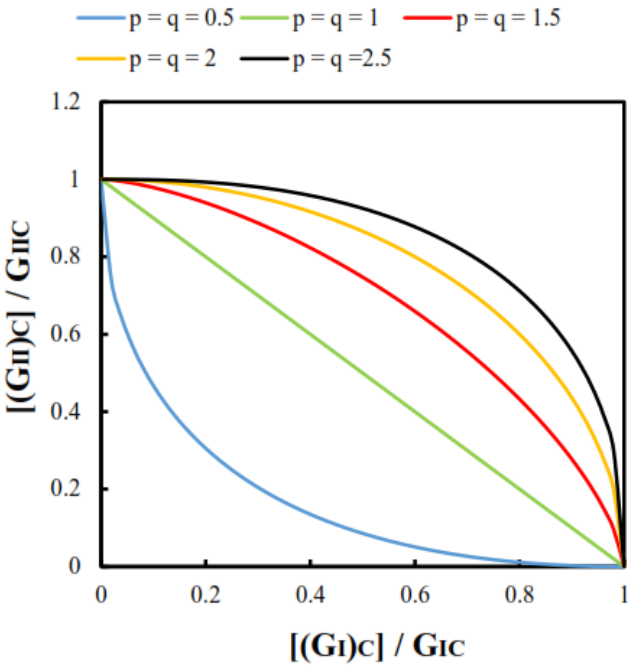

Figure 6-6. Variation of the power law fracture envelope with different values of p and q (it is assumed $p = q$).

The finite element software ABAQUS has the ability of simulating cohesive zone model using traction separation law which uses failure parameters *p* and *q*. Figure 6-7 illustrates variation of the horizontal and vertical displacements at the edge of the concrete slab versus parameters *p* and *q*. The critical fracture energies for pure modes were assumed to be the same as that of considered in section 5 (subsection 5.5.2). It can be seen that both horizontal and vertical displacements dramatically decrease by increasing parameters *p* and *q*. In fact, the lower values of *p* and *q* means lower de-bonding threshold as shown in Figure 6-6 and thus, the concrete slab can be separated easier.

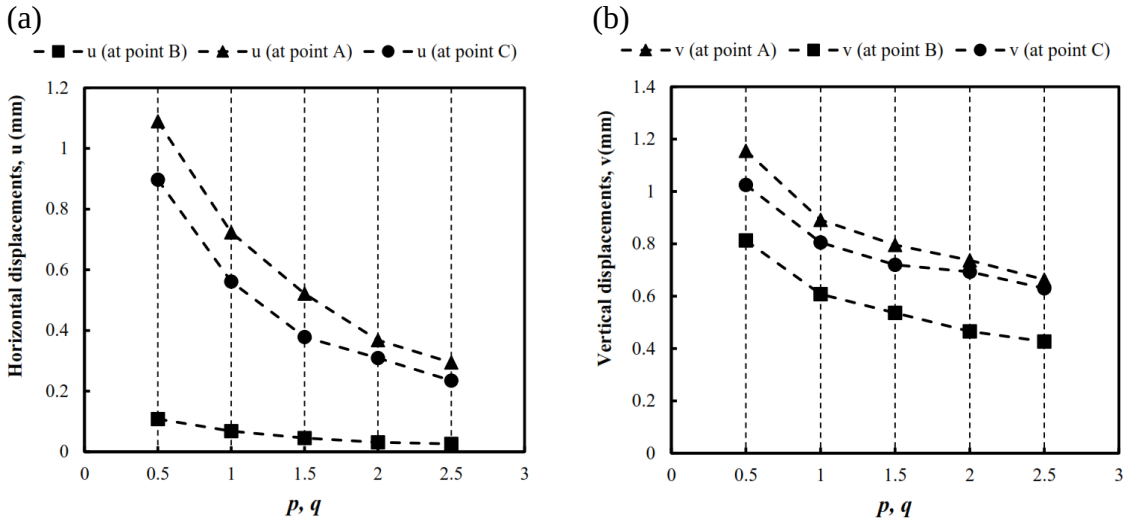

Figure 6-7. Variation of displacements at the slab edge versus different values of *p* and *q*. (a) horizontal displacement, (b) vertical displacement. Z_0 = 15cm, L = 76cm, and t_{base} = 5cm.

6.6. Effect of temperature gradient

The concrete slab response to temperature differences through the slab thickness has been recognized as curling. A positive temperature difference between the top and the bottom surfaces of the concrete slab ($\Delta T = T_{top} - T_{bottom} > 0$) during daytime causes the slab edges to curl downwards while a negative temperature difference during night time results in the upward curling of the concrete slab. Since concrete can recover its original shape after the effects of temperature variation are removed, the curling due to temperature variation from daily or seasonal weather condition can be considered as a transient component of slab curvature behavior due to environmental loading (Yu et al. [158]). Curling can create not only slab deformation but also internal stresses in the absence of traffic loading. Westergaard [8] proposed the first well known closed– form solution for prediction of concrete slab curling deflections and stress on the basis of assumption of an infinite or semi-infinite plain concrete slab over dense liquid foundation. Bradbury [159] later extended Westergaard's bending stress solutions for a two dimensional concrete slab with finite dimensions.

Although the temperature profile through the depth of the concrete slab is nonlinear [160, 161] the concept of equal linear temperature profile, which simplifies calculation of the temperature induced stresses, is widely accepted by the pavement engineers. According to this concept, the total nonlinear temperature profile in a slab can be thought of as having three components, as shown in Figure 6-8: (a) uniform component causing axial expansion or contraction, (b) a linear component causing bending of pavement slab, and (c) a zero – moment nonlinear component that remains

after subtraction of the uniform and linear component from total nonlinear components. It is worth noting that the lack of knowledge of the zero–moment nonlinear component can lead to higher maximum computed tensile stress during day time and lower maximum computed tensile stress during night time [161]. However, it is shown by Yu et al. [158] that the zero– moment nonlinear temperature component does not have a significant influence on the calculation of curling displacements. That means, any nonlinear temperature profile can be converted to its equivalent linear profile to be used by pavement engineers for designing CRC pavements.

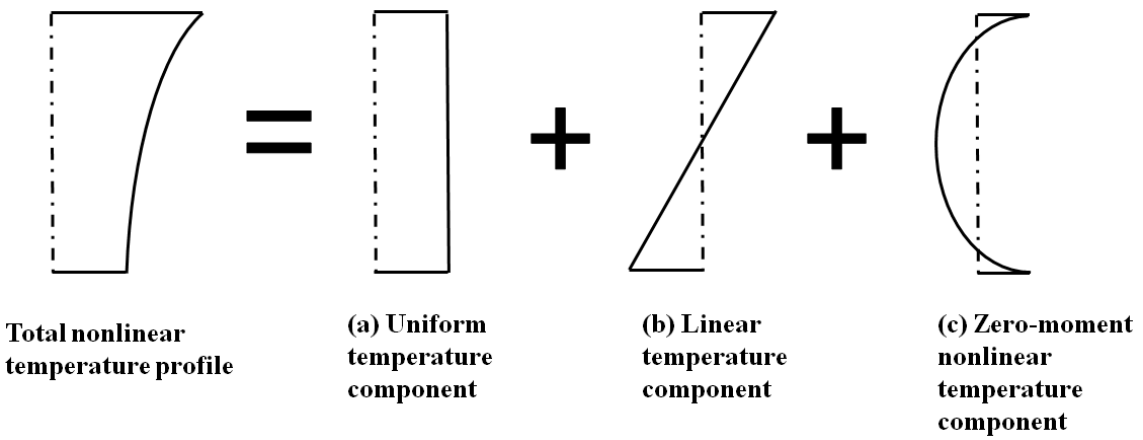

Figure 6-8. Typical temperature profile through the slab thickness, proposed by Choubane and Tia [161].

Figure 6-9 shows effect of linear temperature difference on the displacements in concrete slab edge. The boundary conditions (like bond strength), other loading profiles (like moisture gradient), and material properties (like modulus) are considered the same as those of used for section 6.3. It is seen that both horizontal and vertical displacements are dramatically influenced by the temperature gradient throughout the concrete

thickness. The end movement in CRC pavement increases as the temperature difference increases. It should be noted that Figure 6-9 is plotted for the nighttime temperature conditions in which the top surface of the slab is cooler than its bottom surface. However, the curling occurs under such conditions and therefore, the nighttime temperature profile is chosen for the current analysis.

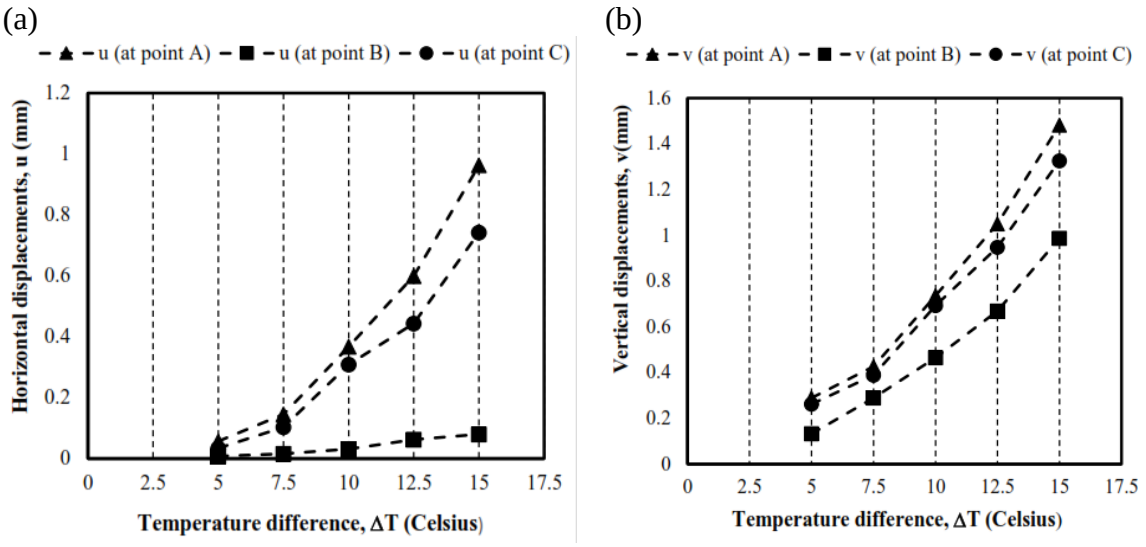

Figure 6-9. Variation of displacements at the slab edge versus different temperature differences, ΔT: (a) horizontal displacement, (b) vertical displacement. Z_0 = 15cm, L = 76cm, and t_{base} = 5cm.

6.7. Effect of moisture gradient

The moisture gradient is influenced by the daily and seasonal weather conditions and the pavement material such as permeable base and poor drainage soils [15]. Especially, it has been recognized that seasonal variations influences more than other factors due to the low hydraulic conductivity of concrete [158, 162]. The variation of

moisture gradient through the thickness of the concrete slab can be expressed as Eq. (6.1);

$$RH(z) = RH_{top} + (RH_{bottom} - RH_{top}) \times \left[1 - (\frac{z}{t_0})^{n'} \right] \tag{6.1}$$

where, parameter n′ controls the moisture profile throughout the slab thickness. Figure 6-10 depicts variation of the moisture profile in concrete thickness for different values of n′. Other parameters in Figure 6-10 are assumed as: $\Delta RH = RH_{bottom} - RH_{top} = 10\%$, and, $RH_{top} = 90\%$. It is well-known that the RH profile is nonlinear through a concrete slab pavement exposed to the environment on its top. In the current analysis, in order to explore the effect of RH difference (ΔRH) throughout the slab, it was assumed n′=3, and the bottom surface is considered as fully saturated ($RH_{bottom} = 100\%$).

Figure 6-11 illustrates displacements at the edge of the concrete slab versus different values of RH difference (ΔRH). It is seen that horizontal end movement is more influenced by the moisture gradient than the vertical end movement. This happens since the moisture profile is one of the primary sources of concrete shrinkage which leads to significant change in slab length in horizontal direction. However, because the concrete slab is restricted at the bottom, the moisture gradient slightly influences on vertical displacements, as shown in Figure 6-11(b).

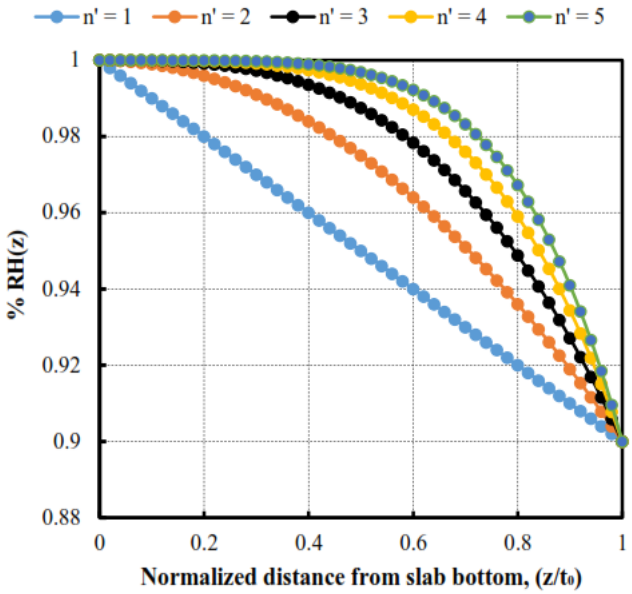

Figure 6-10. Variation of RH through slab thickness with different values of n′ for $\Delta RH = RH_{bottom} - RH_{top} = 10\%$, and, $RH_{top} = 90\%$.

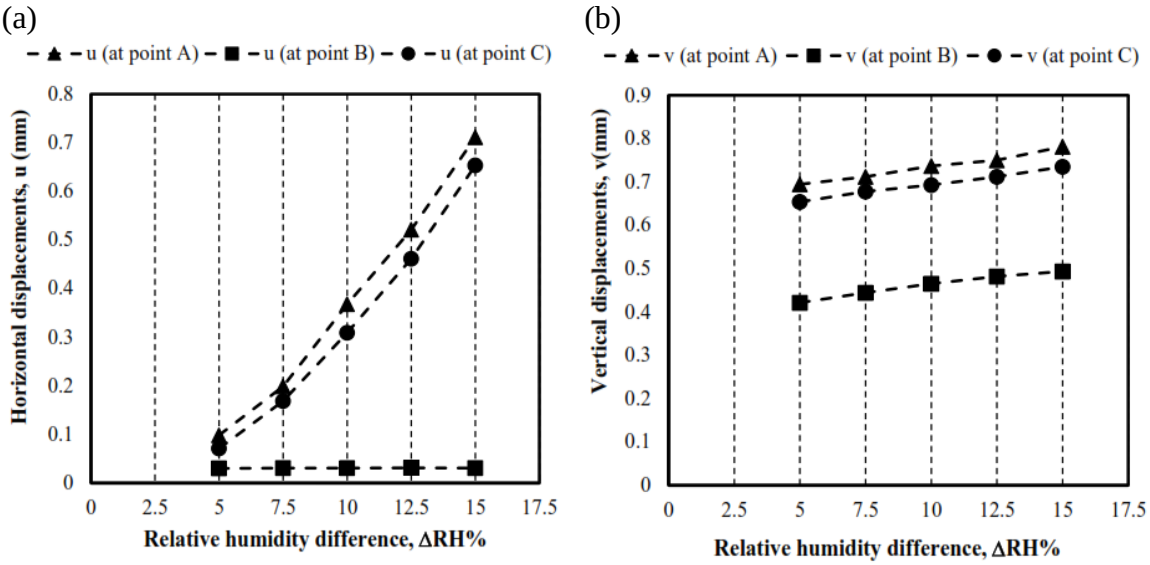

Figure 6-11. Variation of displacements at the slab edge versus different moisture differences, ΔRH: (a) horizontal displacement, (b) vertical displacement. n′=3, Z_0 = 15cm, L = 76cm, and t_{base} = 5cm.

6.8. Summary and conclusions

The effect of different parameters on the end movements in CRC pavements was studied. The findings obtained in this section of the dissertation can be summarized as the following:

The geometry of the CRC pavement remarkably influence its end movements. As the length of the concrete slab increases, the horizontal end movement increases, however, the vertical displacement component does not change significantly. The location of the reinforcing steel bar has a considerable effect on the vertical end movement, but has almost no effect on the horizontal displacement of the slab edge. It was also found that the thickness of the subbase layer does not have a significant influence on the end movements in concrete slab. However, it has to be mentioned that for very thin subbase layers, the behavior may be changed due to the bond strength effects. However, exploring such effects needs a multiscale simulation which was out of scope of the current research.

The effects of modulus of the subbase layer on the slab displacements was also investigated. It was also found that the modulus of the subbase layer does not have a significant influence on the end movements in concrete slab. This results bring this fact to mind that the end movement in concrete slab is more influenced by the bond strength between the concrete slab and the subbase layer, rather than the subbase modulus.

The role of bond strength on the end movements in concrete slab was also studied. Using the power-law fracture criterion, developed for weak interfaces, it was shown that the bond strength significantly influences on the end movement in concrete

slab. The role of power-law fracture criterion exponent, n′, on the prediction of the horizontal and vertical displacements in CRCP was also explored. The results of this part emphasizes the necessity of conducting fracture tests for evaluation of the bond strength between the concrete slab and the subbase layer, as was done in section 4 of this dissertation.

The effects of temperature and moisture gradients on the horizontal and vertical end displacements in concrete slab were also explored. It was shown that the temperature gradient influences end movements in both horizontal and vertical directions, but the moisture gradient has a more effect on the horizontal displacements than the vertical component.

7. SUMMARY, CONCLUSIONS, AND FUTURE RESEARCH

7.1. Summary and conclusions

Continuously Reinforced Concrete Pavement (CRCP) is the most widely used rigid pavement type in Texas as well as other states due to its durable nature and minimum maintenance cost. In order to design CRC pavements, many factors must controlled in order to decrease maintenance costs and prevent CRCP from deterioration. Although the use of in-situ measurements provides a very good understanding of the CRCP behavior, they represent a set of data collected for an especial case of traffic and environmental loads. Therefore, the mechanism behind CRCP behavior must be explored in order to present a more general design framework. In addition, the in-situ investigations always cost more than laboratory and computational simulations. Thus, one of the best options would be exploring mechanism of CRCP behavior using laboratory tests and computational simulations, and then, trying to correlate these findings with the real field applications.

There are many factors influencing CRCP displacements over time like, temperature and moisture gradients, modulus, CRCP dimensions, and the bond behavior between the concrete slab and the subbase layer. Over past fifty years, researchers have tried to model CRCP behavior using either closed form solutions or computational frameworks. However, none of them considered bond strength between the concrete slab and the subbase layer in a realistic manner, as discussed in section 2.

The current dissertation tried to take into account effect of bond strength between the concrete slab and the subbase layer in a more realistic manner than previous studies, by taking into consideration the crack propagation at the concrete slab/ subbase interface. The investigation started from one step behind the area of the study to fundamentally understand mechanism of interfacial crack propagation in a general bi-material system. Section three of the dissertation was focused on studying different fracture criteria for crack propagation at the interface of two dissimilar materials. A new stress-based fracture criteria was proposed for prediction of the mixed mode interfacial fracture toughness as well as the crack kinking angles. The proposed criterion, which was developed for strong interfaces, was then employed to predict mixed mode fracture toughness and the kinking angles in different bi-material components made of different engineering materials. It was found that the proposed criterion provides more accurate estimation of the experimental data than other traditional criteria. The crack propagation at the interface of weak bonds (where the interface crack propagates through the interface instead of kinking into one of the materials) was also explored using power-law fracture criterion. It was pointed out that for weak interfaces, the crack propagation mechanism is mainly affected by the chemical bond strength rather than material property of each bonded material.

In the next section (section four), a new fracture test specimen was developed for evaluation of the interfacial mixed mode fracture toughness of bonded materials. The features and advantages of the suggested specimen was discussed in this section. One of the most important advantages of the proposed test specimen was covering all spectrum

of the mode mixities from pure mode I to pure mode II conditions. The proposed specimen was then employed to explore interfacial mixed mode fracture toughness of AC/PCC at different temperatures.

The next two sections of the dissertation, sections 5 and 6, were focused on different models for prediction of the end movements in CRC pavements due to the environmental loads. Starting from theoretical closed form models, the one dimensional Palmer's model was introduced and its capabilities and its limitations was discussed. Then, the Palmer's model was modified by the replacement of the traditional bond-slip model with the interfacial fracture mechanics concepts. The suggested model was presented in a two-dimensional framework and was able to consider effect of slab lift-off on the horizontal end movements. The modified Palmer's model was then compared to the results obtained from two dimensional finite element simulation of a plain concrete and a very good correlation was observed between them.

Because of existence of the reinforcing steel bar, it is not possible to model CRCP using two dimensional finite element simulation. Therefore, a three dimensional finite element simulation program was suggested in which the concrete slab/ subbase and reinforcing steel bar/ concrete slab interfaces were simulated using zero thickness cohesive zone elements. The program was able to implement interfacial fracture criterion parameters into the simulation directly using traction-separation constitutive law. Then, the experimental data obtained by the previous researchers for the end movement of a JPCP were predicted using the suggested three dimensional finite element program, in order to examine validity of the approach, and an acceptable

agreement was found between them. Finally, the effect of slab dimensions, location of the reinforcing steel bar, subbase modulus, concrete slab/ subbase bond strength, and temperature and moisture gradients on the horizontal and vertical end movements, as well as the relative steel bar/ concrete displacements were investigated in section six using the suggested three dimensional finite element simulations. It was found that some of these factors significantly influence on the end movements, while some others have no influence or only influence on one of displacement components. The results obtained in section six can be useful for pavement engineers for designing CRC pavements under environmental loads.

7.2. Future research

The research topic explored in this dissertation can be extended in many ways. In fact, although the CRCP has been investigated using different models and simulation approaches so far, the research topic is still on its beginning because of its complexity. There are a vast amount of factors affecting CRCP behavior which have not been investigated yet. Some of them are summarized in the following;

The CRC pavement consist of different composite layers made of different size of aggregates, cementitious materials, water, and other chemicals. Although the material properties of the layers are considered to be constant when studying general behavior of CRC pavements, the story is completely different at smaller size scales. The first step toward this fact is to consider CRCP layers as composite materials instead of considering them as homogeneous materials. The next step would be study of the effect of such

internal ingredients on the material properties of each layer. For instance, the study of the effects of size and percentage of the aggregates, hydration, and water transport on the coefficient of thermal expansion, and modulus of the each layer falls inside this research circle.

It is also worth mentioning that in some CRC pavements, the subbase layer is made of asphalt concrete which is a viscoelastic material. The effect of different constitutive models for the CRCP layers on the concrete slab displacements can also be considered as another extension of the current research topic. A more complex simulation can be performed by considering different constitutive models to each ingredients (cementitious materials, aggregates, C-S-H, and water) separately at different CRCP layers.

As pointed out in section 3 and investigated in section 4, the bond strength for weak interfaces is more affected by the chemical bonds between two materials than their individual mechanical properties. The story is completely different for strong interfaces in which the interface crack kinks into one of the materials and therefore, the material property of the weaker material controls the interfacial fracture toughness. That means, a multiscale investigation is necessary to understand mechanism of bond failure for weak interfaces, which may not be necessary for strong interfaces. On the other hand, as shown in section 4, the concrete slab/ subbase interfaces behaves like a weak bond rather than a strong bond and therefore, a multiscale investigation is needed to achieve a better description of the concrete slab/ subbase delamination due to the environmental loads. The output of the multiscale investigation of the concrete slab/ subbase, and concrete

slab/ reinforcing steel bar interfaces can be used for modification of the traction-separation constitutive law used in this research. Also, the effect of bond strength between reinforcing steel bar and the concrete slab on the CRCP end movements can be investigated which was assumed to be constant in the current study.

Finally, it is worth noting again that the current research was mainly focused on the effects of environmental loads (temperature and moisture gradients) on the end movements in CRCP. The effect of traffic loads on the displacements in concrete slab was not investigated in this dissertation. This can also be considered as a future research topic. In fact, an in-service CRC pavement is subjected to both traffic and environmental loads simultaneously, which must be considered for design purposes. However, the primary source of slab lift-off and other distresses in CRC pavements is because of the environmental loads.

REFERENCES

[1] Highway Research Board. Continuously Reinforced Concrete Pavement. National Cooperative Highway Research Program Synthesis of Highway Practice 16, Washington D.C., 1973.

[2] AASTHO. AASHTO Guide for the Design of Pavement Structures. American Association of State Highway and Transportation Officials, Washington D.C., 1986.

[3] Nam JH. Early-age behavior of CRCP and its implications for long-term performance [Dissertation]. Austin, Texas: University of Texas at Austin; 2005.

[4] Palmer RP. A mechanistic model for the prediction of stresses, strains, and displacements in continuously reinforced concrete pavements [Dissertation]. College Station, Texas: Texas A&M University; 1988.

[5] McCullough BF, Elkins GE. CRC pavement design manual. Austin Research Engineers, Inc. Prepared for the Associated Reinforced Bar Producers−CRSI. Austin, Texas. 1979.

[6] Mendoza-Diaz A, McCullough BF. Design charts for the design of HMAC overlays on PCC pavements to prevent reflection cracking. Center for Transportation Research, The University of Texas at Austin, Research Report # 249-6. 1983.

[7] Zhang X. Effects of base characteristics on curling stresses of continuously reinforced concrete pavements. CICTP 2012: Multimodal Transportation Systems—Convenient, Safe, Cost-Effective, Efficient. 2012:3169-74.

[8] Westergaard HM. Analysis of stresses in concrete pavements due to variations of temperature. Proceedings of the Sixth Annual Meeting of the Highway Research Board. 1927; 6:201-15.

[9] Tang T, Zollinger D, Senadheera S. Analysis of concave curling in concrete slabs. Journal of Transportation Engineering. 1993; 119(4):618–33.

[10] Bari ME, Zollinger DG. New concepts for the assessment of concrete slab interfacial effects in pavement design and analysis. International Journal of Pavement Engineering. 2016; 17(3): 233-44.

[11] Jeong JH, Zollinger DG. Early-age curling and warping behavior: insights from a fully instrumented test-slab system. Transportation Research Record: Journal of the Transportation Research Board. 2004; 1896:66-74.

[12] Jeong JH, Lee JH, Suh YC, Zollinger DG. Effect of slab curling on movement and load transfer capacity of saw-cut joints. Transportation Research Record: Journal of the Transportation Research Board. 2006; 1947: 69-78.

[13] Bissonnette B, Attiogbe EK, Miltenberger MA, Fortin C. Drying shrinkage, curling, and joint opening of slabs-on-ground. ACI Materials Journal. 2007; 104(3):259-67.

[14] Mohamed A, Hansen W. Effect of nonlinear temperature gradient on curling stress in concrete pavements. Transportation Research Record: Journal of the Transportation Research Board. 1997; 1568:65-71.

[15] Rao S, Roesler JR. Characterizing effective built-in curling from concrete pavement field measurements. Journal of Transportation Engineering. 2005; 131(4):320-27.

[16] Yu H, Khazanovich L, Darter M, Ardani A. Analysis of concrete pavement responses to temperature and wheel loads measured from instrumented slabs. Transportation Research Record: Journal of the Transportation Research Board. 1998; 1639:94-101.

[17] Rao C., Barenberg EJ, Snyder MB, Schmidt S. Effects of temperature and moisture on the response of jointed concrete pavements. Seventh International Conference on Concrete Pavements. The Use of Concrete in Developing Long-Lasting Pavement Solutions for the 21st Century. 2001; 23-38.

[18] Cha SW. Modeling of hydration process and analysis of thermal and hygral stresses in hardening concrete [Dissertation]. Seoul, Korea: Seoul National University; 1999.

[19] Mehta PK, Monteiro PJM. Concrete: Microstructure, properties, and materials. Second Edition, New York City, USA: the McGraw-Hill Companies, Inc.; 1993.

[20] Mindess S, Young JF. Concrete. New Jersey, USA: Prentice-Hall Inc.; 1981.

[21] McCullough BF, Zolinger D, Dossey T. Evaluation of the performance of Texas pavements made with different coarse aggregates. Center for Transportation Research, The University of Texas at Austin, Report # 3925-1. 1999.

[22] Nam J-H, Kim S-M, Moon W. Measurement and analysis of early-age concrete strains and stresses: Continuously reinforced concrete pavement under environmental loading. Transportation Research Record: Journal of the Transportation Research Board. 2006; 1947: 79-90.

[23] Byfors J. Plain concrete at early-ages. Sweden: Swedish Cement and Concrete Research Institute. Report # FO 3:8. 1980.

[24] ACI Committee. 517. Accelerated curing of concrete at atmospheric pressure – State of the art. ACI Materials Journal. 1980; 6:429-48.

[25] Emborg M. Thermal stresses in concrete structures at early ages [Dissertation]. Lulea, Sweden: Lulea University of Technology; 1989.

[26] Kosmatka SH, Panarese WC. Design and control of concrete mixtures. Illinois, USA: Portland Cement Association; 1988.

[27] Samarai M, Popovics S, Malhotra, VM. Effect of high temperatures on the properties of hardened concrete. Transportation Research Record. 1983; 924.

[28] Suh YC, Hankins K, McCullough BF. Early-age behavior of continuously reinforced concrete pavement and calibration of the failure prediction model in the CRCP-7 Program. Center for Transportation Research, The University of Texas at Austin, Report # 1244-3. 1992.

[29] Schaels CA, Hover KC. Influence of mix proportions and construction operations on plastic shrinkage cracking in thin slab. ACI Materials Journal. 1988; 85: Title No. 85-M48.

[30] Bazant ZP, Najjar LJ. Drying of concrete as a nonlinear diffusion problem. Cement and Concrete Research. 1971; 1(5): 461-73.

[31] Neville AM. Properties of concrete. Essex, UK: Addison Wesley Longman; 1996.

[32] Lura P, Van Breugel K, Maruyama I. Autogenous and drying shrinkage of high strength lightweight aggregate concrete at early ages-The effect of specimen size. Proceedings of the International RILEM Conference. 2002:335-42.

[33] Zhutovsky S, Kovler K, Bentur A. Efficiency of lightweight aggregates for internal curing of high strength concrete to eliminate autogenous shrinkage. Materials and Structures. 2002; 35(2): 97-101.

[34] Polak MA. Effective stiffness model for reinforced concrete slabs. Journal of Structural Engineering. 1996; 122(9):1025-30.

[35] Polak MA, Vecchio FJ. Nonlinear analysis of reinforced-concrete shells. Journal of Structural engineering. 1993; 119(12):3439-62.

[36] Zhang J, Li VC. Influence of supporting base characteristics on shrinkage-induced stresses in concrete pavements. Journal of transportation engineering. 2001;127(6):455-62.

[37] Delcourt C, Jasenski A. First application of a concrete overlay on a bitumen paved motorway in Belgium. Proceedings of the 7th international symposium on concrete roads. 1994:15–20.

[38] Petersson O, Silfwerbrand J. Thin concrete overlays on old asphalt roads. Proceedings of the 5th International conference on concrete pavement design and rehabilitation, USA: Purdue University. 1993:241–6.

[39] Mack JW, Wu CL, Tarr SM, Refai T. Model development and interim design procedure guidelines for ultra-thin whitetopping pavements. Proceedings of the 6th international conference on concrete pavement design and rehabilitation, Indianapolis, USA. 1997: 231–54.

[40] Rasmussen RO, Rozycki DK. Thin and ultrathin whitetopping–A synthesis of highway practice. NCHRP Synthesis 338. Transportation Research Board. 2004.

[41] Sadd M, Shukla A, Subramaniam VK, Lee KW. Determination of interfacial bond behavior of composite concrete-asphalt pavement systems. US Department of Transportation. Report # FHWA-RIDOT-RTD-08-1. 2008.

[42] Chabot A, Hun M, Hammoum F. Mechanical analysis of a mixed mode debonding test for composite pavements. Construction and Building Materials. 2013; 40:1076-87.

[43] Tschegg EK, Macht J, Jamek M, Steigenberger J. Mechanical and fracture-mechanical properties of asphalt-concrete interfaces. ACI Materials Journal. 2007; 104(5): 474–80.

[44] Jung YS, Zollinger D, Wimsatt A. Test method and model development of subbase erosion for concrete pavement design. Transportation Research Record: Journal of the Transportation Research Board. 2010; 2154: 22-31.

[45] Pouteau B, Balay JM, Chabot A, Larrard FD. Fatigue test and mechanical study of adhesion between concrete and asphalt. 9th International Symposium on Concrete Roads, Istanbul, Turkey. 2004.

[46] Mirsayar MM, Huang K, Zollinger DG. New approach to determining concrete slab lift-off by use of interfacial fracture mechanics concepts. Transportation Research Record: Journal of the Transportation Research Board. 2016; 2590:10-17.

[47] Tozzo C, Antonio D, Al-Qadi I. Prediction of fatigue failure at asphalt concrete layer interface from monotonic testing. Transportation Research Record: Journal of the Transportation Research Board. 2015; 2507:50-56.

[48] Kim SM, Kim Nelson P, Ruiz M, Otto Rasmussen R, Turner D. Early-age behavior of concrete overlays on continuously reinforced concrete pavements. Transportation Research Record: Journal of the Transportation Research Board. 2003; 1823: 80-92.

[49] Totsky ON. Behavior of multi-layered plates on Winkler foundation (in Russian). Moscow: Stroitel'naya Mekhanika I Raschet Sooruzhenii. 1981; 6:54-8.

[50] He MY, Hutchinson JW. Kinking of a crack out of an interface. Journal of Applied Mechanics. 1989; 56(2):270-78.

[51] Hurd DS, Caretta R, Gerberich WW. An experimental fracture mechanics study of a strong interface: The silicon/glass anodic bond. Journal of materials research. 1995; 10(02):387-400.

[52] Martin E, Leguillon D, Lacroix C. A revisited criterion for crack deflection at an interface in a brittle bimaterial. Composites science and technology. 2001; 61(12):1671-9.

[53] Evans AG, Ruhle M, Dalgleish BJ, Charalambides PG. The fracture energy of bimaterial interfaces. Metallurgical Transactions A. 1990; 21(9): 2419-29.

[54] Ayatollahi MR, Mirsayar MM, Nejati M. Evaluation of first non-singular stress term in bi-material notches. Computational Materials Science. 2010; 50(2):752-60.

[55] Mirsayar MM. On fracture of kinked interface cracks–The role of T-stress. Materials and Design. 2014; 61:117-23.

[56] Fernlund G, Spelt JK. Mixed-mode fracture characterization of adhesive joints. Composites Science and Technology. 1994; 50(4):441-9.

[57] Campilho RD, Banea MD, Chaves FJ, Da Silva LF. Extended finite element method for fracture characterization of adhesive joints in pure mode I. Computational Materials Science. 2011; 50(4):1543-9.

[58] Alvarez D, Blackman BR, Guild FJ, Kinloch AJ. Mode I fracture in adhesively-bonded joints: A mesh-size independent modelling approach using cohesive elements. Engineering Fracture Mechanics. 2014; 115:73-95.

[59] Fernlund G, Papini M, McCammond D, Spelt JK. Fracture load predictions for adhesive joints. Composites Science and Technology. 1994; 51(4):587-600.

[60] Choupani N. mixed-mode cohesive fracture of adhesive joints: Experimental and numerical studies. Engineering fracture mechanics. 2008; 75(15):4363-82.

[61] Nikbakht M, Choupani N, Hosseini SR. 2D and 3D interlaminar fracture assessment under mixed-mode loading conditions. Materials Science and Engineering: A. 2009; 516(1):162-168.

[62] Sharifi S, Choupani N. Stress analysis of adhesively bonded double-lap joints subjected to combined loading. World Academy of Science, Engineering and Technology. 2008; 41(17):758-63.

[63] Yang YQ, Dudek HJ, Kumpfert J. Interfacial reaction and stability of SCS-6 SiC/Ti–25Al–10NB–3V–1MO composites. Materials Science and Engineering: A. 1998; 246(1-2): 213–20.

[64] Labossierea PEW, Dunn ML, Cunninghamc SJ. Application of bimaterial interface corner failure mechanics to silicon/glass anodic bonds. Journal of the Mechanics and Physics of Solids 2002; 50(3):405–33.

[65] Greco F, Leonetti L, Lonetti P. A two-scale failure analysis of composite materials in presence of fiber/matrix crack initiation and propagation. Composite Structures. 2013; 95:582–97.

[66] Chen X, Beyerlein IJ, Brinson LC. Bridged crack models for the toughness of composites reinforced with curved nanotubes. Journal of the Mechanics and Physics of Solids. 2011; 59(9):1938 – 52.

[67] Chaudhuri RA, Chiu SHJ. Three-dimensional asymptotic stress field at the front of an unsymmetric bimaterial wedge associated with matrix cracking or fiber break. Composite Structures 2007; 78(2):254–63.

[68] Chandra Kishen JM, Singh KD. Stress intensity factors based fracture criteria for kinking and branching of interface crack: application to dams. Engineering Fracture Mechanics. 2001; 68(2):201-19.

[69] Williams ML. The stresses around a fault or crack in dissimilar media. Bulletin of the seismological society of America. 1959; 49:199–204.

[70] Dempsey JP, Sinclair GB. On the stress singularities in the plane elasticity of the composite wedge. Journal of Elasticity. 1979; 9:373-91.

[71] Berto F, Lazzarin P. Recent developments in brittle and quasi-brittle failure assessment of engineering materials by means of local approaches. Materials Science and Engineering R Reports. 2014; 75:1–48.

[72] Berto F, Lazzarin P, Marangon C. Brittle fracture of U-notched graphite plates under mixed mode loading. Materials and Design. 2012; 41: 421-32.

[73] Velu M, Sunil B. Experimental investigations of fracture and fatigue crack growth of copper–steel joints arc welded using nickel-base filler. Materials and Design. 2015; 67: 244-60.

[74] Berto F, Croccolo D, Cuppini R. Fatigue strength of a fork-pin equivalent coupling in terms of the local strain energy density. Materials and Design. 2008; 29:1780-92.

[75] Berto F, Gallo P, Lazzarin P. High temperature fatigue tests of un-notched and notched specimens made of 40CrMoV13.9 steel. Materials and Design. 2014; 63: 609-19.

[76] Yang J, Wang G., Xuan FZ, Tu ST, Liu CJ. Out-of-plane constraint effect on local fracture resistance of a dissimilar metal welded joint. Materials and Design. 2014; 55: 542-50.

[77] Berto F, Lazzarin P, Marangon C. Fatigue strength of notched specimens made of 40CrMoV13.9 under multiaxial loading. Materials and Design. 2014; 54: 57-66.

[78] Berto F, Campagnolo A, Elices M, Lazzarin P. A synthesis of Polymethylmethacrylate data from U-notched specimens and V-notches with end holes by means of local energy. Materials and Design. 2013; 49: 826-33.

[79] Malyshev BM, Salganik RL. The strength of adhesive joints using the theory of cracks. International Journal of Fracture. 1965;1(2):114-19.

[80] He MY, Hutchinson JW. Kinking of a crack out of an interface. Journal of Applied Mechanics. 1989; 111:270–78.

[81] Rice JR. Elastic fracture mechanics concepts for interfacial cracks. Journal of Applied Mechanics. 1988; 55(1):98-104.

[82] Yuuki R, Xu JQ. Stress based criterion for an interface crack kinking out of the interface in dissimilar materials. Engineering Fracture Mechanics. 1992; 41(5):635-44.

[83] Erdogan F, Sih GC. On the crack extension in plates under plane loading and transverse shear. Journal of Basic Engineering. 1963; 85:525–27.

[84] Ayatollahi MR, Dehghany M, Mirsayar MM. A comprehensive photoelastic study for mode I sharp V-notches. European Journal of Mechanics-A/Solids; 2013; 37: 216-230.

[85] Qian ZQ. On the evaluation of wedge corner stress intensity factors of bi-material joints with surface tractions. Computers and Structures. 2001; 79(1):53-64.

[86] Ayatollahi MR, Mirsayar MM, Dehghany M. Experimental determination of stress field parameters in bi-material notches using photoelasticity. Materials and Design. 2011; 32 (10):4901-8

[87] Mirsayar MM, Aliha MRM, Samaei AT. On fracture initiation angle near bi-material notches – Effect of first non-singular stress term. Engineering Fracture Mechanics. 2014; 119: 124 – 31.

[88] Shlyannikov VN. T-stress for crack paths in test specimens subject to mixed mode loading. Engineering Fracture Mechanics. 2013; 108:3–18

[89] Smith DJ, Ayatollahi MR, Pavier MJ. The role of T-stress in brittle fracture for linear elastic materials under mixed mode loading. Fatigue and Fracture of Engineering Materials and Structures. 2001; 24(2):137–50.

[90] Dreier G, Schmauder S.T-stress related to thermal residual stresses in bi-materials. Scripta metallurgica et Materialia. 1993; 28:103-8.

[91] Li XF, Xu LR.T-stresses across static crack kinking. Journal of Applied Mechanics. 2007; 74(2):181-90.

[92] Mirsayar MM. Mixed mode fracture analysis using extended maximum tangential strain criterion. Materials and Design. 2015; 86:941-947.

[93] Mirsayar MM, Park P. The role of T-stress on kinking angle of interface cracks. Materials and Design. 2015; 80:12-19.

[94] Ravichandran M, Ramesh K. Evaluation of stress field parameters for an interface crack in a bimaterial by digital photoelasticity. The Journal of Strain Analysis for Engineering Design. 2005; 40(4): 327-43.

[95] Taylor D, Merlo M, Pegley R, Cavatorta MP. The effect of stress concentrations on the fracture strength of polymethylmethacrylate. Materials Science and Engineering: A. 2004; 382(1):288–94.

[96] Taylor D. The theory of critical distances. Engineering Fracture Mechanics. 2008; 75(7):1696–705.

[97] Hussain MA, Pu SL, Underwood J. Strain energy release rate for a crack under combined mode I and Mode II. Fracture Analysis ASTM STP 560, American Society for Testing and Materials. Philadelphia: USA. 1974: 2–28.

[98] Chang KJ. On the maximum strain criterion – a new approach to the angled crack problem. Engineering Fracture Mechanics. 1981; 14:107-24.

[99] Bowen JM, Knauss WG. An experimental study of interfacial crack kinking. Experimental Mechanics. 1993; 33(1): 37-43.

[100] Xie D, Waas AM, Shahwan KW, Schroeder JA, Boeman RG. Fracture criterion for kinking cracks in a tri-material adhesively bonded joint under mixed mode loading, Engineering Fracture Mechanics. 2005; 72(16):2487–504.

[101] Kawaguchi T, Pearson RA. The effect of particle–matrix adhesion on the mechanical behavior of glass filled epoxies. Part 2. A study on fracture toughness. Polymer. 2003; 44(15):4239–47.

[102] Johnson WS, Mall S. A fracture mechanics approach for designing adhesively bonded joints. Delamination and debonding of materials. ASTM International. 1985.

[103] Dillard DA, Singh HK, Pohlit DJ, Starbuck JM. Observations of decreased fracture toughness for mixed mode fracture testing of adhesively bonded joints. Journal of Adhesion Science and Technology. 2009; 23(10-11):1515-30.

[104] Kinloch A. Adhesion and adhesives: science and technology. Berlin, Germany: Springer Science and Business Media; 2012.

[105] Charalambides M, Kinloch AJ, Wang Y, Williams JG. On the analysis of mixed-mode failure. International Journal of Fracture. 1992; 54(3):269-91.

[106] Hashemi S, Kinloch AJ, Williams JG. Corrections needed in double-cantilever beam tests for assessing the interlaminar failure of fibre-composites. Journal of Materials Science Letters. 1989; 8(2):125-29.

[107] Chen B, Dillard DA. Numerical analysis of directionally unstable crack propagation in adhesively bonded joints. International journal of solids and structures. 2001; 38(38):6907-24.

[108] Chen CS, Krause R, Pettit RG, Banks-Sills L, Ingraffea AR. Numerical assessment of T-stress computation using a p-version finite element method. International Journal of Fracture. 2001; 107(2):177-199.

[109] Chai H. A note on crack trajectory in an elastic strip bounded by rigid substrates. International journal of fracture. 1986; 32(3):211-213.

[110] Wang HT, Wang GZ, Xuan FZ, Tu ST. An experimental investigation of local fracture resistance and crack growth paths in a dissimilar metal welded joint. Materials and Design. 2013; 44:179-89.

[111] Dunn ML, Cunningham SJ, Labossiere PE. Initiation toughness of silicon/glass anodic bonds. Acta materialia. 2000; 48(3):735-44.

[112] Williams JG, Ewing PD. Fracture under complex stress – the angled crack problem. International Journal of Fracture.1972; 8:441–6.

[113] Theocaris PS. A higher-order approximation for the T criterion of fracture in biaxial fields. Engineering Fracture Mechanics. 1984; 19:975–91.

[114] Fett T, Gerteisen G, Hahnenberger S, Martin G, Munz D. Fracture tests for ceramics under mode-I, mode-II and mixed-mode loading. Journal of the European Ceramic Society. 1995; 15:307–12.

[115] Xeidakis GS, Samaras IS, Zacharopoulos DA, Papakalitakis GE. Crack growth in a mixed-mode loading on marble beams under three point bending. International Journal of Fracture. 1996; 79:197–208.

[116] Suresh S, Shih CF, Morrone A, O-Dowd NP. Mixed-mode fracture toughness of ceramic materials. Journal of the American Ceramic Society. 1990; 73(5):1257–67.

[117] Tikare V, Choi SR. Combined mode I and mode II fracture of monolithic ceramics. Journal of the American Ceramic Society. 1993; 76(9):2265–72.

[118] Choi SR, Zhu D, Miller RA. Fracture behavior under mixed-mode loading of ceramic plasma-sprayed thermal barrier coatings at ambient and elevated temperatures. Engineering Fracture Mechanics. 2005; 72(13):2144–58.

[119] Bhattacharjee D, Knott JF. Effect of mixed mode I and II loading on the fracture surface of polymethyl methacrylate (PMMA). International Journal of Fracture. 1995; 72:359–81.

[120] Aliha MRM, Ayatollahi MR, Kharrazi B. Crack growth behavior of a brittle polymer under combined tensile-shear deformation. 14th international conference on deformation, yield and fracture of polymers. Netherlands; 2009.

[121] Aliha MRM, Ayatollahi MR, Kharrazi B. Numerical and experimental investigation of mixed mode fracture in granite using four point bend damage and fracture mechanics. Damage Fracture Mechanics. Netherlands: Springer; 2009: 275–83.

[122] Awaji H, Sato S. Combined mode fracture toughness measurement by the disc test. Journal of Engineering Materials and Technology. 1978; 100:175–82.

[123] Shetty DK, Rosenfield AR, Duckworth WH. Mixed-mode fracture in biaxial stress state: application of the diametral-compression (Brazilian disk) test. Engineering Fracture Mechanics. 1987; 26(6):825–40.

[124] Chang SH, Lee CI, Jeon S. Measurement of rock fracture toughness under modes I and II and mixed–mode conditions by using disc-type specimen. Engineering geology. 2002; 66(1):79–97.

[125] Khan K, Al-Shayea NA. Effect of specimen geometry and testing method on mixed I-II fracture toughness of a limestone rock from Saudi Arabia. Rock mechanics and rock engineering. 2000; 33(3):179–206.

[126] Lim IL, Johnston IW, Choi SK, Boland JN. Fracture testing of a soft rock with semi-circular specimens under three-point bending, part 2 – mixed mode. International journal of rock mechanics and mining sciences and geomechanics abstracts. 1994; 31(3):199–212.

[127] Aliha MRM, Ayatollahi MR. Brittle fracture evaluation of a fine grain cement mortar in combined tensile-shear deformation. Fatigue and Fracture of Engineering Materials and Structures. 2009; 32:987–94.

[128] Ayatollahi MR, Aliha MRM, Hasani MM. Mixed mode brittle fracture in PMMA – an experimental study using SCB specimens. Materials Science and Engineering: A. 2006; 417(12):348–56.

[129] Krishnan GR, Zhao Xl, Zaman M, Roegiers JC. Fracture toughness of a soft sandstone. International Journal of Rock Mechanics and Mining Sciences.1998; 35(6):695–710.

[130] Aliha MRM, Ayatollahi MR, Smith DJ, Pavier MJ. Mixed mode crack path investigation in a limestone rock using two circular shape samples – An experimental and theoretical study. International conference on crack paths. Vicenza: Italy; 2009.

[131] Mahajan RV, Ravi-Chandar K. An experimental investigation of mixed-mode fracture. International Journal of Fracture. 1989; 41:235–52.

[132] Richard HA, Benitz K. A loading device for the creation of mixed mode in fracture mechanics. International Journal of Fracture.1983; 22:55–8.

[133] Arcan M, Hashin Z, Volosnin A. A method to produce uniform plane-stress states with application to fibre-reinforced materials. Experimental Mechanics. 1978; 18:141–6.

[134] Ewing PD, Swedlow JL, Williams G. Further results on the angled crack problem. International Journal of Fracture. 1976; 12:85–93.

[135] Ayatollahi MR, Aliha MRM. Analysis of a new specimen for mixed mode fracture tests on brittle materials. Engineering Fracture Mechanics. 2009; 76:1563–73.

[136] Charalambides PG, Lund J, Evans AG, McMeeking RM. A test specimen for determining the fracture resistance of bimaterial interfaces. Journal of Applied Mechanics. 1989; 56(1):77-82.

[137] Evans AG, Dalgleish BJ. He M, Hutchinson JW. On crack path selection and the interface fracture energy in bimaterial systems. Acta Metallurgica. 1989; 37(12): 3249-54.

[138] Lim IL, Johnston IW, Choi SK. Stress intensity factors for semi-circular specimens under three-point bending. Engineering Fracture Mechanics. 1993; 3:363–82.

[139] Chong KP, Kuruppu MD, Kuszmual JS. Fracture toughness determination of layered materials. Engineering Fracture Mechanics.1987; 28(1):43–54.

[140] Li X, Marasteanu MO. Cohesive modeling of fracture in asphalt mixtures at low temperatures. International Journal of Fracture. 2005; 136: 285–308.

[141] Roberts FL, Kandhal PS, Brown ER, Lee DY, Kennedy TW. Hot mix asphalt materials, mixture design and construction. 1996.

[142] McCullough BF, William BL. LTS Design of Continuously Reinforced Concrete Pavements. Journal of the Highway Division, Proceedings of the ASCE. 1960; 86.

[143] McCullough BF, Ayyash AA, Hudson WR, Randall JP. Design of continuously reinforced pavements for highways. Center for Transportation Research, The University of Texas at Austin, NCHRP 1-15; 1975.

[144] Won MC, Hankis K, McCullough BF. Mechanistic analysis of continuously reinforced concrete pavements considering material characteristics, variability, and fatigue. Center for Transportation Research, The University of Texas at Austin, Report # 1169-2. 1991.

[145] Dossey T, McCullough BF. Characterization of concrete properties with age. Center for Transportation Research, The University of Texas at Austin. 1992.

[146] Won MC, Dossey T, Easley S, Speer J. CRCP-8 program user's guide. Center for Transportation Research, The University of Texas at Austin. 1995.

[147] Kim SM, Won M, McCullough BF. Development of a finite element program for continuously reinforced concrete pavements. Federal Highway Administration, Report # FHWA/TX-98/1758-S. 1997.

[148] Kim SM, Won M, McCullough BF. Numerical modeling of continuously reinforced concrete pavement subjected to environmental loads. Transportation Research Record: Journal of the Transportation Research Board. 1998; 1629:76 – 89.

[149] Kim SM, Won M, McCullough BF. Three dimensional analysis of continuously reinforced concrete pavements. Transportation Research Record: Journal of the Transportation Research Board. 2000; 1730:43 – 52.

[150] Kim SM, Won M, McCullough BF. Three dimensional nonlinear finite element analysis of continuously reinforced concrete pavements. Center for Transportation Research, The University of Texas at Austin, Report#1831-1. 2000.

[151] ACI committee 408. Bond stress – the state of the art. ACI journal proceeding. 1966; 63(11):1161 – 89.

[152] Abaqus. User's Manual Version 6.8. Providence, RI.: Habbit, Karlsson and Sorensen, Inc.; 2008.

[153] Bazant, ZP. Mathematical modeling of creep and shrinkage of concrete. Chichester: Wiley. 1988.

[154] Jeong J-H, Zollinger DG. Environmental effects on the behavior of jointed plain concrete pavements. Journal of Transportation Engineering. 2005; 131(2):140-48.

[155] William GW, Shoukry SN. 3D finite element analysis of temperature-induced stresses in dowel jointed concrete pavements. International Journal of Geomechanics. 2001; 1(3):291-307.

[156] Ihekwaba NM, Hope BB, Hansson CM. Pull-out and bond degradation of steel rebars in ECE concrete. Cement and Concrete Research. 1996; 26(2):267-82.

[157] Harajli MH. Comparison of bond strength of steel bars in normal-and high-strength concrete. Journal of Materials in Civil Engineering. 2004; 16(4):365-74.

[158] Yu HT, Khazanovich L, Darter MI. Consideration of JPCP curling and warping in the 2002 design guide. Transportation Research Board 83rd Annual Meeting. Washington, D.C.: Transportation Research Board; 2004.

[159] Bradbury RD. Reinforced Concrete Pavements. Wire Reinforcement Institute, Washington, D.C. 1938.

[160] Thomlinson J. Temperature variations and consequent stresses produced by daily and seasonal temperature cycles in concrete slabs. Concrete Constructional Engineering. 1940; 36(6): 298-307.

[161] Choubane B, Tia MA. Nonlinear temperature gradient effect on maximum warping stresses in rigid pavements. Transportation Research Record: Journal of the Transportation Research Board. 1992; 1370(1):11.

[162] Vandenbossche JM. Interpreting falling weight deflectometer results for curled and warped Portland cement concrete pavements. 2003.

APPENDIX A

STRESS FIELD AROUND AN INTERFACE CRACK

The multi-parameter Cartesian stress field equations in polar coordinates corresponding to material-1 are [55, 94];

$$\begin{Bmatrix}\sigma_{xx}^{(1)}\\ \sigma_{yy}^{(1)}\\ \sigma_{xy}^{(1)}\end{Bmatrix}=\sum_{n=0,2,4,\ldots}^{N}\frac{K_{In}}{Q}r^{\frac{(n-1)}{2}}\begin{Bmatrix} S^{(1)}\Big\{3\cos[\frac{n-1}{2}\theta-\varepsilon\ln(\frac{r}{L})]-(n-1)\sin\theta\sin[\frac{n-3}{2}\theta-\varepsilon\ln(\frac{r}{L})]\\ S^{(1)}\Big\{\cos[\frac{n-1}{2}\theta-\varepsilon\ln(\frac{r}{L})]+(n-1)\sin\theta\sin[\frac{n-3}{2}\theta-\varepsilon\ln(\frac{r}{L})]\\ S^{(1)}\Big\{-\sin[\frac{n-1}{2}\theta-\varepsilon\ln(\frac{r}{L})]-(n-1)\sin\theta\cos[\frac{n-3}{2}\theta-\varepsilon\ln(\frac{r}{L})]\end{Bmatrix}$$

$$\begin{Bmatrix}+2\varepsilon\sin\theta\cos[\frac{n-3}{2}\theta-\varepsilon\ln(\frac{r}{L})]\Big\}-\frac{1}{S^{(1)}}\cos[\frac{n-1}{2}\theta+\varepsilon\ln(\frac{r}{L})]\\ -2\varepsilon\sin\theta\cos[\frac{n-3}{2}\theta-\varepsilon\ln(\frac{r}{L})]\Big\}+\frac{1}{S^{(1)}}\cos[\frac{n-1}{2}\theta+\varepsilon\ln(\frac{r}{L})]\\ -2\varepsilon\sin\theta\sin[\frac{n-3}{2}\theta-\varepsilon\ln(\frac{r}{L})]\Big\}+\frac{1}{S^{(1)}}\sin[\frac{n-1}{2}\theta+\varepsilon\ln(\frac{r}{L})]\end{Bmatrix}$$

$$+\sum_{n=1,3,5,\ldots}^{N}\frac{K_{In}}{R^{(1)}}r^{\frac{(n-1)}{2}}\begin{Bmatrix}4\cos[\frac{n-1}{2}\theta]-(n-1)\sin\theta\sin[\frac{n-3}{2}\theta]\\ (n-1)\sin\theta\sin[\frac{n-3}{2}\theta]\\ -2\sin[\frac{n-1}{2}\theta]-(n-1)\sin\theta\cos[\frac{n-3}{2}\theta]\end{Bmatrix}$$

$$+\sum_{n=0,2,4,\ldots}^{N}\frac{K_{IIn}}{Q}r^{\frac{(n-1)}{2}}\begin{Bmatrix} S^{(1)}\Big\{3\sin[\frac{n-1}{2}\theta-\varepsilon\ln(\frac{r}{L})]+(n-1)\sin\theta\cos[\frac{n-3}{2}\theta-\varepsilon\ln(\frac{r}{L})]\\ S^{(1)}\Big\{\sin[\frac{n-1}{2}\theta-\varepsilon\ln(\frac{r}{L})]-(n-1)\sin\theta\cos[\frac{n-3}{2}\theta-\varepsilon\ln(\frac{r}{L})]\\ S^{(1)}\Big\{\cos[\frac{n-1}{2}\theta-\varepsilon\ln(\frac{r}{L})]-(n-1)\sin\theta\sin[\frac{n-3}{2}\theta-\varepsilon\ln(\frac{r}{L})]\end{Bmatrix}$$

$$
\left.\begin{array}{l}
+2\varepsilon\sin\theta\sin[\dfrac{n-3}{2}\theta-\varepsilon\ln(\dfrac{r}{L})]\Big\}+\dfrac{1}{S^{(1)}}\sin[\dfrac{n-1}{2}\theta+\varepsilon\ln(\dfrac{r}{L})] \\
-2\varepsilon\sin\theta\sin[\dfrac{n-3}{2}\theta-\varepsilon\ln(\dfrac{r}{L})]\Big\}-\dfrac{1}{S^{(1)}}\sin[\dfrac{n-1}{2}\theta+\varepsilon\ln(\dfrac{r}{L})] \\
+2\varepsilon\sin\theta\cos[\dfrac{n-3}{2}\theta-\varepsilon\ln(\dfrac{r}{L})]\Big\}+\dfrac{1}{S^{(1)}}\cos[\dfrac{n-1}{2}\theta+\varepsilon\ln(\dfrac{r}{L})]
\end{array}\right\}
$$

$$
+\sum_{n=1,3,5,\ldots}^{N}\frac{K_{IIn}}{R^{(1)}}r^{\frac{(n-1)}{2}}\left\{\begin{array}{c}
2\sin[\dfrac{n-1}{2}\theta]+(n-1)\sin\theta\cos[\dfrac{n-3}{2}\theta] \\
2\sin[\dfrac{n-1}{2}\theta]-(n-1)\sin\theta\cos[\dfrac{n-3}{2}\theta] \\
-(n-1)\sin\theta\sin[\dfrac{n-3}{2}\theta]
\end{array}\right\}
$$

where

$$Q = 2\sqrt{2\pi}\cosh(\pi\varepsilon) \tag{A.2}$$

$$S^{(1)} = e^{-\varepsilon(\pi-\theta)} \tag{A.3}$$

$$R^{(1)} = \sqrt{2\pi}(1+\omega)\ ,\omega = \frac{1+\kappa_1}{1+\kappa_2}\frac{G_2}{G_1} \tag{A.4}$$

The stress field expressions for material-2 can be obtained by replacing $e^{-\varepsilon\pi}$ by $e^{+\varepsilon\pi}$, $e^{+\varepsilon\pi}$ by $e^{-\varepsilon\pi}$, ω by $1/\omega$ and replacing the corresponding $R^{(2)}$ and $S^{(2)}$ into the Eq. (A.1). The Cartesian stress components could be easily transformed into the polar coordinate system, mentioned in Eq. (3.1), as:

$$\sigma_{rr}^{(m)} = \sigma_{xx}^{(m)} \cos^2\theta + \sigma_{yy}^{(m)} \sin^2\theta + \sigma_{xy}^{(m)} \sin[2\theta]$$
$$\sigma_{\theta\theta}^{(m)} = \sigma_{xx}^{(m)} \sin^2\theta + \sigma_{yy}^{(m)} \cos^2\theta - \sigma_{xy}^{(m)} \sin[2\theta] \qquad \text{(A.5)}$$
$$\sigma_{r\theta}^{(m)} = -\sigma_{xx}^{(m)} \sin\theta\cos\theta + \sigma_{yy}^{(m)} \sin\theta\cos\theta + \sigma_{xy}^{(m)} (\cos^2\theta - \sin^2\theta)$$

The parameters f_{rr}, $f_{\theta\theta}$ and $f_{r\theta}$ in Eq. (3.1) could easily be obtained. For example for $\sigma_{rr}^{(m)}$ we have:

$$f_{rr\_1}^{(m)} = f_{xx\_1}^{(m)} \cos^2\theta + f_{yy\_1}^{(m)} \sin^2\theta + f_{xy\_1}^{(m)} \sin[2\theta] \qquad \text{(A.6)}$$
$$f_{rr\_2}^{(m)} = f_{xx\_2}^{(m)} \cos^2\theta + f_{yy\_2}^{(m)} \sin^2\theta + f_{xy\_2}^{(m)} \sin[2\theta]$$

where $f_{xx\_1}^{(m)}$, $f_{yy\_1}^{(m)}$, $f_{xx\_2}^{(m)}$, $f_{yy\_2}^{(m)}$ are the terms of the series expansion of Eq. (A.1) corresponding to n = 0. It also should be mentioned that K_I, K_{II} and T in Eq. (3.1) are K_{I0}, K_{II0} and K_{I1} in Eq. (A.1) respectively.